

X-Atlas: An Online Archive of Chandra's Stellar High Energy Transmission Gratings Observations

Owen W. Westbrook¹, Nancy Ramage Evans, Scott J. Wolk, Vinay L. Kashyap, Joy S. Nichols, Peter J. Mendygral², Jonathan D. Slavin, Bradley Spitzbart

Harvard-Smithsonian Center for Astrophysics, 60 Garden Street, Cambridge, MA 02138

nevans@cfa.harvard.edu

and

Wayne L. Waldron

Eureka Scientific, Inc., 2452 Delmer Street Suite 100, Oakland, CA 94602-3017

ABSTRACT

October 25, 2018

The high-resolution X-ray spectroscopy made possible by the 1999 deployment of the *Chandra X-ray Observatory* has revolutionized our understanding of stellar X-ray emission. Many puzzles remain, though, particularly regarding the mechanisms of X-ray emission from OB stars. Although numerous individual stars have been observed in high-resolution, realizing the full scientific potential of these observations will necessitate studying the high-resolution *Chandra* dataset as a whole. To facilitate the rapid comparison and characterization of stellar spectra, we have compiled a uniformly processed database of all stars observed with the *Chandra* High Energy Transmission Grating (HETG). This database, known as X-Atlas, is accessible through a web interface with searching, data retrieval, and interactive plotting capabilities. For each target, X-Atlas also features predictions of the low-resolution ACIS spectra convolved from the HETG data for comparison with stellar sources in archival ACIS images. Preliminary analyses of the hardness ratios, quantiles, and spectral fits derived from the predicted ACIS spectra reveal systematic differences between the high-mass and low-mass stars in the atlas and offer evidence for at least two distinct classes of high-mass stars. A high degree of X-ray variability is also seen in both high and

¹present address: Massachusetts Institute of Technology, Cambridge, MA

²present address: University of Minnesota, Twin Cities, MN

low-mass stars, including Capella, long thought to exhibit minimal variability. X-Atlas contains over 130 observations of approximately 25 high-mass stars and 40 low-mass stars and will be updated as additional stellar HETG observations become public. The atlas has recently expanded to non-stellar point sources, and Low Energy Transmission Grating (LETG) observations are currently being added as well.

Subject headings: stars: galactic — stars: early-type — stars: late-type — X-rays: stars — *Chandra X-ray Observatory* — transmission gratings — databases

1. INTRODUCTION

Chandra has made high-resolution X-ray spectra of bright objects readily available. Over 130 observations of stars have been made in high resolution and analyzed, resulting in both insight and further questions about X-ray production, magnetic fields, stellar winds, and line shapes. However, the extracted gratings spectra are not currently expected to be part of the level 3 data products slated to be released by the *Chandra X-ray Center* in 2008. We have therefore compiled a database, known as X-Atlas,¹ of all stars observed with the *Chandra* high and medium energy gratings (HETG) and extracted the spectra in a uniform manner.

Additionally, although over 60 stars have been observed in high spectral resolution, thousands of stellar sources have been imaged with the *Chandra* ACIS CCDs, which have sufficient energy resolution to produce an extractable low-resolution spectrum for each source. To enable comparisons of the analyses made at low-resolution with results from the high-resolution spectra, we have used the HETG grating observations in X-Atlas to predict the low-resolution ACIS spectra by convolving the HETG spectra with the response functions of the ACIS detectors. These predicted low-resolution spectra, as well as hardness ratios and quantiles calculated from them, are a valuable tool for interpreting the physical properties of the large sample of stars observed only at low spectral resolution. For further comparison, we have also extracted the low-resolution zeroth-order spectrum from the HETG observations.

As a demonstration of the capabilities of the database, we present some early science results from X-Atlas. We use the high-resolution spectra to develop line ratio metrics for quick characterization of the target. Analyses of the predicted hardness ratios and quantiles of the stars in the atlas indicate that high-mass and low-mass stars exhibit distinct coronal

¹<http://cxc.harvard.edu/XATLAS/>

temperature regimes and suggest that at least two classes of high-mass OB stars exist. Variability analyses performed on each star reveal that a high proportion of the stars in X-Atlas exhibit variability during their *Chandra* observation period. Even stars generally considered minimally-variable, such as Capella, may undergo count rate fluctuations between observations while remaining stable over the time scale of a typical observation.

Both the high-resolution and predicted low-resolution spectra are made available in FITS and ASCII text formats through a dedicated web interface. This web interface allows users to search the database and create customized spectral plots of up to three sources, selecting either individual lines or spectral regions for intercomparison. We note that a similar spectral browsing utility has been created by González-Riestra & Rodríguez-Pascual (2007) for the plotting of Reflection Grating Spectrometer (RGS) observations from *XMM-Newton*, though without the data retrieval and low-resolution predictions offered by X-Atlas. In addition to offering interactive plotting capabilities, we also present on the X-Atlas web page the spectra in montages as functions of spectral type and object class for high-mass OB stars, Wolf-Rayet stars, and low-mass stars. Hardness ratios and quantiles also available for plotting and retrieval on the web page.

The X-Atlas spectral database will be updated as additional stellar HETG observations are carried out and archived. Further, we have applied the reduction and analysis methods used for normal stars to HETG observations of other point sources, including neutron stars, galactic novae, active galactic nuclei, and other exotic objects. All LETG observations of both stellar and non-stellar point sources will also eventually be included in the database.

We describe the high-resolution spectral atlas in §2, and the low-resolution predictions in §3. We discuss the characteristics of the sources in X-Atlas in §4, and summarize in §5.

2. HIGH-RESOLUTION ATLAS

The initial motivation for creating X-Atlas was to make available for comparison all of the *Chandra* high-resolution gratings observations of OB stars. X-Atlas has since been expanded to include low-mass stars as well. The database currently features over 130 observations² of roughly 25 high-mass and 40 low-mass stars (Section 2.5), with additional observations being added as they are made public.

²as of July 2007

2.1. HETG Observations and Data Reduction

The HETG consists of two grating arms: the High Energy Grating (HEG), optimized for a spectral range of approximately 1.5 to 15 Å, and the Medium Energy Grating (MEG), sensitive up to 30 Å (Weisskopf et al. 2002). The dispersed spectra produced by these grating arms cross at their respective zeroth orders, creating the elongated ‘x’ for which X-Atlas is named.

We have reprocessed each observation in the X-Atlas database uniformly, eliminating the need for weighing different analysis techniques and assumptions from observation to observation and enabling quick comparisons of X-ray sources in the atlas. The *Chandra* team has maintained a robust software package, *CIAO*, for the reduction and analysis of *Chandra* data (Fruscione et al. 2006). Using the most recent version (3.4) of *CIAO*, we have created a Perl pipeline script of the appropriate *CIAO* tools and ‘threads’³ needed to reduce and analyze each observation and have added our own IDL routines and S-Lang scripts for further analysis. The calibration files used for this processing are those available with the *Chandra* Calibration Database (CALDB) 3.3.0. After retrieving the necessary files from the *Chandra* Data Archive (CDA), this pipeline carries out a number of standard X-ray reduction steps, removing various instrumental distortions, locating the 0th-order centroid and the dispersed spectra of each gratings arm, classifying the dispersed photons by spectral order, and coadding the positive and negative grating spectral orders of the HEG and MEG spectra before proceeding to processing and analyses developed specifically for X-Atlas.

Data preparation for a given observation begins with the level 1 event file, a list of the arrival times and energies of incoming photons that is available from the Chandra data archive. Most *Chandra* archival data has undergone Standard Data Processing (SDP) during the most recent reprocessing run, which began in February 2006, but for those observations that have not yet been reprocessed, additional corrections are necessary.

Some portion of the X-ray events detected by *Chandra* are caused by cosmic ray interactions in the CCD, and if not removed, these ‘afterglow’ events can be interpreted as faint sources. Possible cosmic ray events are flagged during SDP, and are filtered out in the level 2 event file. Note that the particular method used in SDP versions prior to 7.4.0 has been shown to reject 3-5% of valid source photons⁴. This issue has been corrected in more recent processing versions, but for archival data that has not yet been reprocessed appropriately, we reset the afterglow flags on the level 1 event file and re-identify afterglows and bad pixels

³<http://asc.harvard.edu/ciao/threads/>

⁴<http://cxc.harvard.edu/ciao/threads/acisdetectafterglow/>

with the updated reduction methods.

In addition to afterglow detection, SDP also randomizes the coordinates of events within the pixel where they are detected to avoid aliasing effects and remove the 'gridded' appearance of the data.⁵ For X-Atlas reductions, we removed this randomization. Observations were also corrected for the contamination of the optical/UV filter on ACIS, a time-dependent drift in the detector gain values, and the charge transfer inefficiency (CTI) of the detectors as charge is moved from pixel to pixel during readout.

The dispersed photons are extracted after the data are prepped as described above. The *CIAO* wrapper script *tgdetect* was used to locate the centroid of the 0th-order image. While *tgdetect* is very accurate for the majority of HETG observations, if the intended target is bright enough to cause the 0th-order image to pile up, *tgdetect* may fail to properly detect the centroid.⁶ However, some of the most severe pileup effects, such as pulse saturation, where the energy of a piled event is greater than the instrumental threshold, are generally absent from stellar HETG observations in the atlas. In cases where *tgdetect* does not accurately identify the position of the zeroth order, the contributed *CIAO* tool *findzero* will usually obtain a correct value. In addition, *CXC's* current reprocessing effort of the entire archive correctly determines the zeroth-order position for piled-up sources. In the interest of applying uniform processing to each observation, we did not implement more sophisticated centroid detection schemes. It is expected that any in-depth scientific analysis of the stars in the atlas will require separate reprocessing of the appropriate observations.

After centroid detection, various *CIAO* tools determine the locations of the grating arms and assign events from each arm to the appropriate spectral orders. At this point, a level 2 event file is created by filtering out bad grades previously marked as afterglows and hot pixels, applying corrections for the effects of excess streaking on chip 8, and selecting only those events falling within the good time intervals determined by SDP.

The grating spectra are then extracted from the destreaked level 2 event file. In addition, we create grating Redistribution Matrix Files (gRMFs) to map between detector pulse height and energy space and Ancillary Response Files (gARFs) to measure the instrumental area and quantum efficiency of the HETG/ACIS-S configuration. The positive and negative spectral orders of each arm are then coadded and stored in six pulse height amplitude (PHA type I) spectral files, each of which corresponds to either the HEG or MEG arm of HETG and to one of the coadded $\pm 1^{st}$, $\pm 2^{nd}$, or $\pm 3^{rd}$ orders. With the high-resolution spectrum

⁵<http://cxc.harvard.edu/ciao/threads/acispixrand/>

⁶http://space.mit.edu/ASC/docs/memo_fzero_1.3.ps

extracted, data reduction continues with processing routines developed specifically for X-Atlas, starting with the creation of the predicted low-resolution ACIS spectra, described in section §3.

This data reduction procedure, including the convolution of the predicted low-resolution ACIS spectra, was developed for stellar observations but is applicable to any X-ray point source. The current release of X-Atlas includes all point sources observed with HETG, including cataclysmic variables, X-ray binaries, and active galactic nuclei. The same methods are being adapted for use with observations of point sources using the ACIS-S/LETG, HRC-S/LETG, and HRC-I/LETG configurations as well. Because of the difficulties involved in the spectroscopy of extended sources, only point sources will be included in X-Atlas. There are no standard *CIAO* tools for the analysis of grating spectra from extended sources. The emission lines in such spectra will take on the shape of the zeroth-order spatial structure convolved with the instrumental Line Spread Function (LSF). Grating analysis of such sources therefore requires spatial/spectral analysis because there is not a unique mapping of wavelength to diffraction angle for extended sources.

2.2. Spectral Line Metrics

Generally, it is difficult to summarize the information contained in a high-resolution spectrum in a few variables that capture the relevant details about the behavior of the source. This is because a coronal source spectrum is dominated by a large number of lines from many elements at different ionization stages, in addition to having an underlying continuum that is determined by the metallicity of the plasma. We have identified a set of line and continuum fluxes that together encompass the major parameters that describe coronal plasmas: temperature, composition, and density. We measure the counts in typically strong lines, such as the H-like and He-like lines of O, Ne, Mg, Si, and S, as well as the prominent Fe XVII lines at 15Å and 17Å. The counts due to the continuum are also measured over different wavelength ranges ($< 12.1\text{\AA}$, $> 12.1\text{\AA}$) to characterize the general shape of the spectra. The various ratios formed by these fluxes serve as proxy for a complete description of the spectrum, but in lower dimensional space. These metrics are listed in Table 1, and are provided in addition to the nominal hardness ratios and quantile widths that are calculated after converting the grating spectra to the lower resolution spectra corresponding to the imaging CCDs.

2.3. Coadding Multiple Observations of the Same Target

For observations of a single target that have been split over multiple observing periods, additional processing is necessary to combine the various exposures into a single dataset. We accomplish this by adding the PHA spectra from each observation together after ensuring that the source or instrument did not experience major variability between observations.

To determine whether a set of observations should be coadded, we developed a number of simple tests. First, we check to see if the actual source appeared to be variable from one observation to the next by examining the count rates in both the 0th-order image spectrum and the HEG and MEG grating spectra. The differences in the total count rates between observations should not be significantly greater than the combined error in the count rates. If either the 0th-order or gratings spectra count rates have shifted more than two-sigma between observations, then either the source or the instrumental effective area has likely changed between observations.

To roughly determine the degree to which changes in the effective area could have contributed to a shift in the observed count rates from one observation to the next, we compare the average fractional changes in the effective area to the previously calculated fractional changes in the count rate. As long as the fractional shifts in effective area are statistically small compared to the fluctuations in the count rates, changes in the HETG/ACIS-S instrument between each observation can be deemed insignificant.

After confirming that the source did not vary between observations, the actual coadding process consists of summing together the $\pm 1^{st}$ order PHA datasets from each observation in their original binning. The wavelength bins for each observation should coincide; if not, the observations must be rebinned to the same wavelength grid. Methods for testing the accuracy of the coaddition are described in section 3.3. There are currently four X-Atlas targets for which the coaddition of multiple observations has been performed (Table 2).

2.4. Extracting Spectra from Crowded Star Fields

A significant proportion of the stars featured in the atlas are proximate to other X-ray bright sources, presenting both a scientific bonus and a technical challenge. Since relatively few stars have been observed at high-resolution, HETG observations of relatively crowded star fields such as the Trapezium or Cyg OB2 present valuable opportunities to enhance the science return of a single observation. Actually performing multiple spectral extractions often proves difficult, particularly if the spectral arms or zeroth-order image of a source fall on the dispersed spectra of another. In such cases, all sources must be extracted simulta-

neously, starting with the tool *tg_create_mask*.⁷ Otherwise, artifacts may be present in the extracted spectra. In general, we recommend that X-Atlas users extract any spectra of interest themselves before undertaking detailed spectral analysis, especially for stars situated in crowded fields.

For the initial release of X-Atlas, we have extracted only the primary target of the observation, usually the brightest star close to the ACIS-S aimpoint. We are beginning to extract secondary and tertiary sources from observations of clusters such as the Trapezium or Cyg OB2, using the *SIMBAD* database to identify bright sources near the aimpoint. We plan to limit the extractions to sources of more than 300 0th-order counts located no more than 4' off-axis. Beyond 4', the ACIS point-spread function broadens dramatically and the 90% encircled energy radius rises well above 1" (Proposers' Observatory Guide 2005).

2.5. Observation Summary

Although the X-Atlas archive will eventually contain all point sources observed with HETG or LETG, this article is intended to only cover stellar sources currently in the atlas. At the time of publication, X-Atlas consisted of all archived stellar HETG observations, including the more than 130 observations shown in Table 3, with the exception of observations that suffered instrumental malfunctions.

2.6. X-Atlas Website Interface

X-Atlas was conceived of as a public tool for research, and a primary goal of the project was to make the data and analyses described here readily available through a user-friendly web interface. We sought to present the data in a form intelligible to people unfamiliar with X-ray spectra while still offering useful capabilities to the expert X-ray astronomer.

The X-Atlas website is fully documented, with the main page containing links to descriptions of the data processing procedures and threads for navigating the website. Links to various *Chandra X-ray Center* pages, other stellar catalogs, and X-ray emission line lists are also provided. For an overview of the atlas's contents, a listing of all observations, ordered by spectral class, can be pulled up, and the proposal abstract and any publications associated with a particular observation can be viewed.

⁷http://cxc.harvard.edu/ciao/ahelp/tg_create_mask.html

The central purpose of the website is to provide an interface for searching, plotting, and retrieving the spectral data products contained in the atlas (Figure 1). The search interface is modeled after the query pages of the *Chandra* Data Archive. The database may be queried by observation or target parameters such as observation ID, target name, spectral type, object type, science category, and observation date, or through a cone search of the target RA and declination. Results may be sorted by spectral type, observation ID, target name, observation date, RA, or declination.

For those observations retrieved in the search, the instrumental configuration of the observation, hardness and quantile data, known physical parameters of the target, spectral fits of the 0th-order and predicted low-resolution spectra, light curves and variability analyses of the observation, the 0th-order image of the extracted target, and preview plots of the HEG and MEG spectra, are readily viewable. The spectral data products for the observation are also made available for download. Observations returned by the search may be marked for interactive, customized spectral plotting and data retrieval.

Three sample uses of the X-Atlas website are outlined below. Note that the procedures for generating the data products in the atlas are discussed below (see §3 and §4). Although these tasks are by no means a comprehensive list of the atlas’s capabilities, we believe that three particularly useful applications of the website will be to view target preview information for individual stars, create spectral plots for the comparison of multiple targets, and retrieve and compare spectral metrics such as hardness ratios and quantiles for a large sample of the observations in the database.

2.6.1. Retrieving Target Information

For the first task, we will retrieve target preview information, including spectral plots, hardness ratios, quantiles, spectral fits, and lightcurves of a star of interest, using FK Com as an example. We start at the X-Atlas search page, entering 'FK Com' as the target name, and run the search. We may also search the atlas without any search filters to retrieve all observations in the database and select FK Com from the list of observations returned.

In either case, after executing the search, we will find an entry for FK Com, Obsid 614, among the observations retrieved. Clicking on the Observation ID will call up *Chandra's* instrumental configuration during the observation. Clicking instead on the target name (FK Com) will bring up a preview of the target extracted from of the observation. Under some basic target information is a snapshot of the 0th-order image along with the 0th-order count rate and a rough estimation of the degree of pileup for a gauge of the reliability of the 0th-

order data. Below is a listing of predicted hardness ratios and quantiles (see Section 4.1) based on the predicted ACIS-S and ACIS-I spectra of FK Com (see Section 3), followed by plots of the spectral fits of the 0th-order and predicted ACIS-S and ACIS-I spectra (see Section 3.4). The relevant fit parameters are listed as well, including N_H , two values of kT, metal abundances, total flux, the flux emission ratio of the two kT components, and χ^2 values of the fit. Below the spectral fits is a light curve constructed from the HETG HEG and MEG data and binned at intervals of 1200 and 4000 s. Variability results from GLvary (described in section 4.2) accompany the plot. Following the light curve are preview plots of the 1st order HEG and MEG spectra in units of counts/s/Å vs. Å. Those wishing to create their own plots of the spectra can simply click on the 'Customize Spectral Plots' button provided on the page. Finally, at the bottom of the preview page, various spectral data products are offered for download, including PHA files for the HEG and MEG spectra, FITS and text files of the reduced HEG and MEG spectra, the predicted low-resolution ACIS and 0th-order spectra, and the actual 0th-order spectrum, and the accompanying gARFs and aimpoint ARFs and RMFs.

2.6.2. Customizing Spectral Plots

A second, more powerful use of the atlas is to create comparison plots of up to three targets at once. For the following example, we will compare the MEG spectra and the Fe XVII emission lines for three T Tauri stars: SU Aur, Speedy Mic, and TV Crt. To do so, we return to the main X-Atlas search page, enter 'T Tauri' as the object type and 'Normal stars and WD' as the science category, and execute the search. This particular search will return over ten observations of T Tauri stars, ordered by spectral type by default. As we scroll through the list, we can click on the checkboxes in the leftmost column for all observations of SU Aur (ObsID 3755), Speedy Mic (ObsIDs 2536 and 3491), and TV Crt (ObsID 3728). After selecting the appropriate observations, we click on 'Select Observation(s) for Plotting' to call up the plotting interface.

The plotting interface allows for the creation of customized spectral plots for up to three targets at once. Three plotting options are offered. The first, marked as 'Option A,' is to view pre-produced plots of the high-resolution HEG or MEG spectra over one of a number of pre-determined spectral ranges in units of counts and wavelength (counts/s/Å vs. Å). Alternatively, the output plots may be customized through a variety of plotting options. The most flexible option, 'Option B,' allows the plotting of multiple datasets of differing spectral resolution and the choice of plot units and spectral range of the output. The available datasets include the high-resolution HETG/ACIS-S HEG and MEG spectra,

the predicted low-resolution ACIS-S or ACIS-I Aimpoint data, and both the extracted and predicted low-resolution HETG/ACIS-S 0th-order spectra. These data may be plotted in units of counts/s/Å or counts/s/bin vs. Å, in counts/s/keV or counts/s/bin vs. keV, or, for the HETG spectra only, in flux units of ph/s/Å/cm² vs. Å. Optional parameters may be set to scale the low-resolution spectra, boxcar smooth the HETG spectra, define upper bounds for the y-axis, or control the pixel resolution of the output plots. These plots are generated with identifications of common spectral lines provided.

To plot the MEG spectra of SU Aur, Speedy Mic, and TV Crt from 5 Å to 25 Å, we begin at 'Option B' on the webpage. First, up to three desired targets are selected, and for each, the grating arm (HEG or MEG) and order (1, 2, or 3) of interest. For this example, we will select the 1st order MEG spectra of SU Aur (ObsID 3755), Speedy Mic (ObsID 2536), and TV Crt (ObsID 3728). The high-resolution HETG/ACIS-S spectrum is already selected as the default dataset for step 2 and counts/s/Å vs. Å is already selected as the default plot units for step 3. In step 4, we enter '5' as the low bound and '25' as the high bound and click on the button to 'Generate Plots.' To instead view the predicted ACIS-S and ACIS-I spectra and plot in energy space, we deselect the high-resolution HETG spectrum and select the predicted ACIS spectra instead, choosing counts/s/keV vs. keV as the plot units. The plot range may be either specified or left blank to use the default values. Any of the low-resolution datasets may also be scaled to the HETG spectrum for viewing on the same plot.

2.6.3. Emission Line Plots

Besides viewing pre-produced plots or specifying the dataset, plot units, and plot range, a final plotting option is offered for the more specific task of making comparisons of emission line profiles of the HEG or MEG spectra. Up to six common X-ray emission lines can be chosen from the drop-down boxes provided to create line profile montages in units of wavelength (counts/s/Å vs. Å or counts/s/bin vs. Å), energy (counts/s/keV vs. keV), or Doppler velocity (counts/s/Å vs. km/s). For instance, to view the Fe XVII emission lines for SU Aur, Speedy Mic, and TV Crt in wavelength units (counts/s/Å vs. Å), we leave all of the fields under 'Option B' blank and instead proceed to 'Option C.' Using any five of the six drop-down boxes, we select the Fe XVII lines at 15.01, 15.26, 16.78, 17.05, and 17.10 Å. We then make sure that the default plot units, counts/s/Å vs. Å, are selected. We may specify the distance from line center of each line profile plot and choose between viewing all lines of a given star on the same scale or plotting each line completely independently. When we are satisfied with the settings, we may click 'Generate Plot.'

The interactively customized plots take only a few seconds to create. The plots are then displayed on the screen along with options to download the plots in GIF, JPEF, and/or postscript form. However, we intend the plotting interface to be used mainly as a browsing tool rather than an end in itself. Therefore, the datasets used to generate the plots are provided for download in FITS files and ASCII text tables, and the HEG and MEG PHA spectral files for the target are offered as well, along with the appropriate grating ARFs and the ACIS-S and ACIS-I aimpoint ARFs and RMFs.

2.6.4. Retrieving X-ray Properties of the X-Atlas Dataset

Besides the capabilities for viewing the observation data and analysis products for individual observations or creating customized spectral plots, the X-Atlas website also provides the means to make quick comparisons of the X-ray properties of the entire X-Atlas dataset. For any subset of observations in the database, hardness ratios and energy quantiles derived from the predicted ACIS-S and ACIS-I spectra and spectral metrics calculated from the HETG data may be retrieved by clicking on the respective links for 'X-Atlas Hardness Ratios and Quantiles' and 'X-Atlas Spectral Metrics' on the X-Atlas home page, the observation search page, or any of the target preview pages. These links will call up tables of these metrics for every X-Atlas observation that can be filtered by the values of each metric and sorted by a variety of target and observation parameters as well as by any of the individual metrics themselves. A similar page is provided for the spectral fits of the predicted ACIS spectra.

2.7. Sample High-Resolution Spectra: Spectral Montages

X-Atlas was conceived as a means of enabling comparisons of stellar spectra across spectral type, hardness, or other characteristics of interest. For this purpose, we have constructed montages of the HETG spectra of both high-mass and low-mass stars to accompany the dynamic plotting capabilities of the website. Only MEG spectra are displayed below, but both HEG and MEG montages will be available on the website, along with montages of the convolved low-resolution spectra shown and described in Section 3. The spectra in the montages are displayed in counts $\text{s}^{-1} \text{\AA}^{-1}$ vs. \AA and are normalized for the purpose of comparison.

Normal OB stars are divided into one montage of supergiants and giants (Figure 2) and another of giants, sub-giants, and dwarfs (Figure 3), both ordered by spectral type. More

exotic high-mass stars are displayed as well. A separate montage is offered of two stars, θ^1 Ori C and τ Sco, in which a magnetic field clearly plays a role in X-ray emission (Gagne, et al. 2005; Donati, et al. 2007; Figure 4). Several peculiar OB stars with unconfirmed X-ray emission mechanisms are shown as well in Figure 5. Two Wolf-Rayet stars are shown in Figure 6, including γ Vel and five observations of WR 140. A series of spectra of η Car passing through periastron was obtained by Corcoran et al. (2005) and is displayed in Figure 7.

The discovery of X-ray emission from high-mass stars in the Carina nebula (Seward et al. 1979; Seward & Chlebowski 1982) and in the Cyg OB2 association (Harnden et al. 1979) with the *Einstein* satellite in the Carina nebula (Seward et al. 1979; Seward & Chlebowski 1982) and in Cyg OB2 (Harnden et al. 1979) came as a surprise. Since then, studies of the energy distributions of massive stars, their spectra, and their line profiles have continued to enlighten and puzzle us. Displaying normal OB stars in montages as a function of optical spectral type reveals a clear shift of mean X-ray flux to lower energies at lower photospheric temperatures for both the supergiants and giants (Figure 2) and giants, sub-giants, and dwarfs (Figure 3). These findings were also noted by Walborn (2006). As he discusses, the constant ratio between bolometric and X-ray luminosities implies such a spectral progression since bolometric luminosity and temperature are related. Stellar winds correlated with luminosity are likely to be the connection with X-ray luminosity.

Because of the diversity of astrophysical mechanisms at work in low-mass stars, spectral montages of these stars are organized by stellar type. In particular, separate montages have been made of normal or rapidly rotating low-mass stars (Figure 8), W UMa-type stars (Figure 10), RS CVn stars (Figure 11), pre-main sequence T Tauri-type stars (Figure 12), and active or flaring low-mass stars (Figure 13). Two unique objects, Algol and FK Com, are also shown (Figure 9).

2.8. Sample High-Resolution Spectra: Line Profiles

Line profiles have been a key diagnostic and continuing puzzle for both high-mass and low-mass stars. In addition to spectral montages, X-Atlas also offers comparison plots of selected targets and emission lines to illustrate some of their variety (Figures 14, 15). As described previously, the interactive plotting interface allows the creation of customized line profile comparisons for up to three observations at a time.

3. LOW-RESOLUTION ATLAS

The high-resolution spectra can be used to predict the low-resolution ACIS-S or ACIS-I image spectra that a source would have produced had the HETG not been in place. This low-resolution prediction can then be analyzed with spectral fitting tools such as *Sherpa* and compared with actual low-resolution ACIS image spectra. By doing so, we potentially gain greater insight into the spectral properties of sources in existing ACIS images for which no high-resolution grating observations currently exist.

3.1. Procedure

Convolving high-resolution HETG spectra to ACIS low-resolution imaging mode spectra involves correcting for the differences in the effective area response with and without the gratings in place. The effective area is a product of the physical light collecting area of the telescope, and the efficiencies of the mirror reflection, filters and gratings, and the detector quantum efficiency. The extracted high-resolution HEG and MEG spectra (C_{HEG} , C_{MEG}) and the relevant effective areas (gA_{HEG} , gA_{MEG}) are first used to project how the target object’s high-resolution spectrum would appear at the 0^{th} -order (f^{0th}), or the ACIS-S or ACIS-I aimpoints (f^{aimS} , f^{aimI}) with no grating in place. The resulting fluxed spectra are then multiplied by the appropriate 0^{th} -order or aimpoint ARFs and convolved with the corresponding Response Matrix File (RMF) to predict the low-resolution spectra of each detector configuration (C^{0th} , C^{aimS} , C^{aimI}).

The extraction of the high-resolution HEG and MEG spectra, described in section 2.1, produces coadded $\pm 1^{st}$, $\pm 2^{nd}$, and $\pm 3^{rd}$ order HEG and MEG source and background spectra in units of counts per wavelength bin. An adaptive binning scheme is then applied to the source and background data using a custom-built IDL routine from PINTofALE (Kashyap & Drake 2000) such that every bin in the spectrum meets a minimum signal-to-noise ratio while overall flux is conserved.⁸ The appropriate signal-to-noise ratio for *smoothie* is determined independently for the source and background data and is generally set to be $\approx 3 - 4$. After the spectra are binned, the source and background errors on each adapted wavelength bin are calculated as the square root of the counts in that bin. The smoothed background is then subtracted from the smoothed source spectrum for both HEG and MEG, with all resulting instances of negative count levels set to zero. Errors on the background-subtracted counts/bin spectrum are calculated by propagating the errors from the separate unsubtracted

⁸<http://hea-www.harvard.edu/PINTofALE/doc/PoA.html#SMOOTHIE>

source and background spectra.

Before the high-resolution HEG and MEG spectra can be converted to low-resolution, we first must determine how the HETG spectrum would appear in high-resolution if observed with the effective area of ACIS-S or ACIS-I rather than the full HETG/ACIS-S configuration. The first step in this correction is to divide the HETG counts/bin spectrum by the effective area of the HETG configuration. The effective area of the gratings, in units of counts cm^{-2} photons $^{-1}$, is contained in a gratings ARF (gARF), one of which is produced for each grating arm and spectral order during the extraction of the high-resolution spectrum. The HEG and MEG gARF effective areas are interpolated onto the spectral range of the appropriate high-resolution data sets, and the adaptively binned high-resolution counts/bin spectrum is converted to a flux spectrum (photons cm^{-2} bin $^{-1}$) by dividing by the interpolated gARF effective area where the gARF is nonzero. Where the gARF effective area is zero, the high-resolution flux is set to zero. The errors on the flux bins are calculated simply by dividing the counts/bin errors by the gARF effective area and by setting the flux error equal to an arbitrary large value where the effective area is zero.

In order to predict the low-resolution spectrum of the ACIS-S or ACIS-I Aimpoint, the high-resolution HEG and MEG spectra must first be combined. Although the MEG sensitivity extends above 30 Å, the HEG spectra do not quite reach 20 Å. Therefore, for the combined spectrum, we define a new common HEG and MEG wavelength grid from 0 to 30 Å at the spectral resolution of the HEG data (0.0025 Å per bin). The MEG wavelength grid offers slightly lower resolution than the HEG (0.005 Å per bin), so the MEG flux spectrum is rebinned onto the common wavelength grid at the higher HEG resolution using another *PINTofALE* (Kashyap & Drake 2000) function.⁹ The MEG flux errors are rebinned in similar fashion.

Next, we calculate the combined HEG flux (f_{HEG}) and MEG flux (f_{MEG}) over the common wavelength grid. For HEG and MEG fluxes within the HEG wavelength range, the flux level in each wavelength bin is computed by weighting the HEG and MEG fluxes by their respective errors. The combined HEG+MEG flux,

$$f_{tot} = \frac{w_{HEG}f_{HEG} + w_{MEG}f_{MEG}}{w_{HEG} + w_{MEG}}, \quad (1)$$

where

$$w_{HEG} = \frac{1}{\sigma_{HEG}}, \quad w_{MEG} = \frac{1}{\sigma_{MEG}}, \quad (2)$$

⁹<http://hea-www.harvard.edu/PINTofALE/doc/PoA.html#REBINW>

where σ_X are the bin-wise propagated errors in each spectrum. For data beyond the HEG wavelength range, w_{HEG} was set to 0.

To predict the high-resolution spectrum of either the ACIS-S aimpoint, the ACIS-I aimpoint, or the HETG/ACIS-S 0^{th} -order, the combined HEG and MEG spectrum is then multiplied by the corresponding effective area of the aimpoint of interest, information contained in standardized ARFs available from the *Chandra* Data Archive,

$$\begin{aligned} f^{0th} &= A^{0th} f_{tot} \\ f^{aimS} &= A^{aimS} f_{tot} \\ f^{aimI} &= A^{aimI} f_{tot}. \end{aligned} \quad (3)$$

Finally, the resulting prediction of the high-resolution counts/bin spectrum at the desired aimpoint is convolved with the appropriate RMF, producing a low-resolution prediction of the ACIS-S aimpoint, ACIS-I aimpoint, or 0^{th} -order spectrum:

$$\begin{aligned} C^{0th} &= Conv(RMF^{0th}, f^{0th}) \\ C^{aimS} &= Conv(RMF^{aimS}, f^{aimS}) \\ C^{aimI} &= Conv(RMF^{aimI}, f^{aimI}). \end{aligned} \quad (4)$$

The ACIS aimpoint ARFs and RMFs are updated every *Chandra* cycle by the *Chandra* Data Archive. For consistency, we use the Cycle 06 calibration products to generate the low-resolution ACIS predictions for each observation in X-Atlas.

Since the HEG and MEG coaddition process is entirely linear, the combined HEG and MEG flux levels will fall between those found in the separate HEG and MEG spectra. However, contrary to intuition, the convolved low-resolution spectra do not follow this rule, i.e., it is possible that the low-resolution spectrum derived by combining both HEG and MEG data could occasionally be either greater or less than each of the component low-resolution spectra. This effect can occur unless one of the conditions

$$\begin{aligned} (a) \quad & f_{HEG} \leq f_{tot} \leq f_{MEG} \\ (b) \quad & f_{HEG} \geq f_{tot} \geq f_{MEG} \end{aligned} \quad (5)$$

holds exclusively for all wavelength bins (i.e., the averaged flux is greater than the MEG flux and less than the HEG flux for every bin – or the reverse) then the following conditions will not hold:

$$\begin{aligned} (a) \quad & C_{HEG}^X \leq C_{tot}^X \leq C_{MEG}^X \\ (b) \quad & C_{HEG}^X \geq C_{tot}^X \geq C_{MEG}^X. \end{aligned} \quad (6)$$

3.2. Test Results: Predicted Zeroth-Order Spectrum

To assess the accuracy of the convolution to low-resolution, we should ideally compare our predictions with actual ACIS image spectra of a given target. Unfortunately, ACIS imaging mode data are not always available for sources observed with the HETG. But every grating observation does contain, in addition to the high-resolution dispersed spectrum, a 0^{th} -order image from which a low-resolution spectrum may be extracted.¹⁰ Using the 0^{th} -order ARF and RMF in place of the ACIS aimpoint ARF and RMF in the high resolution to low resolution conversion process described above (§3), we can predict the 0^{th} -order spectrum and compare it with the actual extracted 0^{th} -order spectrum to determine whether the results of the convolution produce an accurate low-resolution spectrum.

This approach is unfortunately of limited use when the 0^{th} -order image has suffered significant pileup. Pileup occurs when multiple photons are detected as a single event, causing both a distortion the energy spectrum, as the apparent energy of a piled event is actually the sum of two or more photons' energies, and a decrease in the apparent count rate, as multiple photons are counted only once (Proposers' Observatory Guide 2005). For evaluation of the low-resolution convolution procedure, we therefore selected several observations with average count rates below 0.05 cts/s within a fifteen pixel radius of the 0^{th} -order, indicating relatively low to mild pileup (Table 4). For these observations, we calculated the χ^2 values for the comparison of the observed and predicted 0^{th} -order spectra. Errors used to calculate the χ^2 values include an extra 10% systematic error attributable to effective area uncertainties (Drake et al. 2006).

For these observations, the predicted low-resolution 0^{th} -order counts spectrum exhibits a close correspondence to the actual 0^{th} -order spectrum. ξ Per, from observation ID 4512, is shown in Figure 16. From the success of the 0^{th} -order convolution, we have confidence that our ACIS-S and ACIS-I aimpoint predictions of low-resolution spectra are indeed accurate.

3.3. Test Results: Coadded Observations

For spectra that have been obtained over multiple observations (see §2.3), the principles and methods described in the previous section for predicting the low-resolution spectrum can be applied to confirm the accuracy with which the observations were coadded. Specifically, comparing the low-resolution prediction of the 0^{th} -order spectrum of the coadded observation to the actual coadded 0^{th} -order spectrum can give a measure of the success of both the

¹⁰<http://cxc.harvard.edu/ciao/threads/pieces/index.html>

coaddition and the convolution to low-resolution.

A low-resolution prediction of the 0^{th} -order spectrum can be generated from the HEG and MEG 1^{st} order spectra of the combined observation using the same steps described in §3.1. The actual extracted 0^{th} -order spectrum of the combined observation is created simply by adding together the 0^{th} -order Pulse Invariant counts spectra of the individual observations and rebinning if necessary.

The comparison of the extracted and predicted 0^{th} -order spectra is shown for the combined observation of HD 93250 in Figure 17, composed of Observation IDs 5399, 5400, 7189, 7341, and 7342. χ^2 values are listed in Table 2 and include additional 10% errors in the observed spectra to approximate calibration errors in the effective area.

3.4. Test Results: Spectral Fitting

Spectral fitting offers a powerful means to extract stellar information from low-resolution ACIS spectra, including absorption (N_H), temperature (kT), and metallicity. We have performed spectral fits on our predicted low-resolution ACIS spectra both to extract such information and to further evaluate the convolution methods that produced the predicted spectra. Spectral fitting is art as well as science, and developing automated fitting routines for bright sources such as are found in X-Atlas has proven difficult. In addition, we have been forced to use techniques developed for non-dispersed spectra on spectra that have been first dispersed by HETG and then un-dispersed with the methods described above. However, by comparing the results of our spectral fits with previously published values, we have been able to verify the quality of our data and the potential for extracting for accurate and useful scientific information from the predicted ACIS spectra.

The predicted ACIS spectra cannot be fit directly, since the statistical errors of the original observation are scrambled during the convolution process, and the errors on the predicted counts in the different channels are no longer independent. In order to obtain a realistic error on these spectra, we first adjust the nominal exposure time such that a total of 1500 counts are predicted, as in a well-exposed low-resolution ACIS observation. We then add Poisson deviates corresponding to the counts intensity in each bin to simulate the statistical error of an actual observation. (Note that this process is similar to that adopted by the `fakeit` commands in *Sherpa* and *XSPEC*.) We then use *Sherpa* to perform two-temperature fits of the predicted ACIS-S spectra. Where $E(B - V)$ values are known (as is the case for a sample of high-mass stars), we estimate the foreground H column density

(N_{H}) ,

$$N_{\text{H}} = 5.9 \cdot 10^{21} \times E(B - V) \text{ cm}^{-2} \quad , \quad (7)$$

and use this estimate to fix the column density during the spectral fit. For hot stars, we estimated $E(B - V)$ from the observed $(B - V)$ and the intrinsic $(B - V)_0$ for O and early B stars ($(B - V)_0 = -0.32$ (Schmidt-Kaler 1982)). Where $E(B - V)$ values are not known, we choose $N_{\text{H}} = 10^{20} \text{ cm}^{-2}$ as the starting value. We then employ *Sherpa* to fit the spectrum with a 2-component **mekal** (Mewe-Kaastra-Liedahl) thermal plasma model (Mewe et al. 1985, 1986; Kaastra 1992; Liedahl et al. 1995), using the **cstat** statistic and the Powell optimization method, extracting temperatures, metallicities, and fluxes from each source. In order to ensure that the fitting is robust, we carry out the fitting process in multiple stages. We first fit the two temperatures, constrained to lie in disjoint regions ([0.01-1] and [1-10] keV) for a fixed metallicity of 0.3 solar. The temperatures found in this way are used as starting values to refit the grouped spectrum, this time using the χ^2 model-variance statistic and the Levenberg-Marquardt optimization method, and allowing for an overlap in the temperature ranges ([0.01-2] and [1-10] keV). The grouped spectrum is then fit again, with N_{H} also being fit if $E(B - V)$ is not known. Next, the temperatures and N_{H} are fixed at their best-fit values and the metallicity is fit. In many cases, especially when the N_{H} is known, this series of steps yields an excellent fit. For those cases which could not be well fitted with four free parameters (N_{H} , two temperatures and metallicity) as noted by temperatures up against range limits and/or $\chi^2/\text{d.o.f.} > 2$, the data are refit in a modified manner. The temperatures (and N_{H} , if necessary) are fit again, freezing the metallicity to the best-fit value, before finally fitting the spectra with three free parameters (N_{H} and two temperatures). We obtain error bars using the *Sherpa* command **projection**.

A selection of the fit results is displayed in Table 5. The fit values compare favorably with published results for θ^1 Ori C. Schulz et al. (2000) report temperatures ranging from 5 to 61×10^6 K, or 0.4 to 5.3 keV, whereas our analyses finds high-temperature components of about 10 to >15 keV and low-temperature components of 1.1 to 1.4 keV. For θ^2 Ori A, Schulz et al. (2006) measure temperatures of above 25×10^6 K (2.2 keV) in the low activity phase and temperatures from 3 to 100×10^6 K (0.3 to 9 keV) in the high activity phase. We find temperatures of 0.79 and 0.34 keV in the low phase and 3.52 and 1.14 keV for the high phase, in reasonable agreement for a variable target.

For γ Cas, Smith et al. (2004) report that the X-ray emission is dominated by a heavily absorbed hot component at 12 keV, with cooler components near 0.1, 0.4, and 3 keV exhibiting much lower absorption. We found only a hot component at >15 keV with a relatively high absorption. The inability of our methods to differentiate the absorptions of the different emission components mostly likely explains why the cooler components were not detected despite comprising about 14% of the total emission (Smith et al. 2004).

Our methods produced highly consistent results over fifteen observations of Capella. Each observation returned a primary temperature component between 0.56 and 0.61 keV, with three observations also returning hotter components ranging from 4 to >10 keV. Canizares et al. (2000) examined plasma diagnostics in the high-resolution HETG spectra and found a broad range in temperatures from $\log T = 6.3$ to 7.2 (~ 0.1 to 1.2 keV), while Brickhouse et al. (2000) report a peak emission measure near $\log T = 6.8$ (0.4 keV) from extreme ultraviolet measurements.

While spectral fits of the Capella observations usually returned only one temperature, all eight observations of the RS CVn star IM Peg returned two emission components when fit. The high temperature component ranged from 1.3 to 3.4 keV, while the low temperature component fell between 0.3 and 1.0 keV. These values agree reasonably well with Huenemörder et al. (2001), who found emission peaks at $\log T = 7.2$ (~ 1.2 keV) in the non-flaring state and $\log T = 7.6$ (~ 2.5 keV) in the flaring state.

On the whole, our results are similar to those published by more painstaking high-resolution analyses. Our goal is not to supplant these more accurate methods but to establish the credibility of our predicted low-resolution ACIS data. The variations between our results and those published emphasize the oversimplification that is necessarily involved in reducing the coronal temperature to two distinct values.

3.5. Sample Predicted Low-Resolution Spectra: Spectral Montages

For every high-resolution spectral montage we have produced (see section 2.4), we have also created a montage of the predicted low-resolution spectra of the same targets. Only predicted ACIS-S spectra are displayed here, but montages of the predicted ACIS-I spectra will also be made available online. As with the HETG montages, all spectra shown here are normalized for viewing purposes (Figures 18 – 29).

4. DISCUSSION

We proceed with a discussion of the properties of the ensemble of stellar spectra, continuing from the summary of high-resolution spectra in Section 2.7. We discuss the hardness ratios and quantiles derived from the predicted low-resolution spectra in section 4.1 and the X-ray variability of individual observations in Section 4.2.

4.1. The X-ray Color of Stars: Quantiles and Hardness ratios

While high-resolution spectral studies by *Chandra* have proven uniquely powerful in their ability to uncover the detailed astrophysics in the source, the time required by these observations limits them to no more than about 20 stellar observations per year. A database such as X-Atlas enhances the high-resolution dataset by providing capabilities for comparison of the low-resolution spectra of the vast numbers of stars in ACIS images in the *Chandra* archive with the relatively few well-studied examples. Two techniques for reducing spectral data to X-ray "color" are hardness ratios and quantiles.

Hardness ratios are comparisons of the total number of counts observed in different X-ray passbands. Using a Bayesian estimation approach developed by Park et al. (2006), we calculated projected hardness ratios for each star in the atlas, using the predicted ACIS-S and ACIS-I low-resolution spectra derived from the original HETG observations. For each target, the predicted ACIS counts were divided into soft, medium, and hard passbands, with energies of 0.3-0.9 keV, 0.9-1.5 keV, and 1.5-8.0 keV respectively.

Then, for each star, two hardness ratios were calculated (see Table 6):

$$HR_1 = \frac{H - M}{H + M} \quad (8)$$

and

$$HR_2 = \frac{M - S}{M + S} \quad (9)$$

S, M, and H are the total number of predicted counts in the soft, medium, and hard energy passbands, respectively. Error bars were also calculated using the methods described in Park et al. (2006). For most observations, the number of predicted counts was high enough that the error bars were insignificant compared to the scatter of the hardness plots. Capella, for instance, exhibits relatively consistent hardness over twelve observations spanning 1999 to 2006. However, the dispersion in the hardness ratios among observations exceeds the 1-sigma error bars, implying that even a relatively unvarying star will undergo statistically significant shifts in hardness over time. Capella's variability is discussed further in Section 4.3.

When the values of each star are plotted with HR_1 vs. HR_2 , a clear trend emerges (Figure 30). Both high-mass and low-mass stars appear to follow a common, confined locus arcing from softer emission near $\sim (-0.6, -0.8)$ through $(0.0, -0.7)$ to harder emission at $(0.9, 0.6)$. The high-mass stars actually occupy the extrema of the locus and the cool stars occupy a smaller range extending from $\sim (0.0, -0.2)$ to $(0.5, 0.0)$. The outliers, which include a ~ 25 ks observation of the Wolf-Rayet star WR 140 and several observations of η Carinae, will be discussed further below.

The observed hardness of a source is a function of temperature and interstellar absorption. To model this dependence, we used a Mekal emissivity model (Mewe et al. 1985, 1986) to predict the expected relationship between HR_1 and HR_2 . Model photon fluxes in each hardness band were calculated from the integrated Mekal emissivities for a range of temperatures and N_H values, assuming interstellar medium (ISM) absorption cross-sections. Normalization of the emissivities was not necessary since hardness ratios depend solely on the ratio of the defined energy bands. We then used the Cycle 06 ACIS-S and ACIS-I response functions to predict the X-ray counts in each passband, yielding hardness ratios derived from the Mekal fluxes for targets observed at the ACIS-S and ACIS-I aimpoints.

In Figures 31 and 32, we show the results of modeling the predicted dependence of HR_1 on HR_2 for ACIS-I count spectra. Using Mekal emissivities for typical coronal temperatures and absorptions, we overlay lines of constant temperature and absorption on separate plots for two abundance values: solar abundance in Figure 31 and 0.1 times solar abundance (for all elements except H) in Figure 32. The lines of constant temperature range from 2.5 to 50 MK (0.16 to 3 keV) for N_H values between 0.01 and $2.5 \times 10^{22}/\text{cm}^2$, with absorption increasing from left to right along each contour. Similarly, the lines of constant N_H include values between 0.01 and $2.5 \times 10^{22}/\text{cm}^2$, with temperature increasing from 2.5 to 50 MK left to right on each contour. According to this model, sources with low absorption and temperature will appear in the lower left of the hardness plot, and hotter, more highly absorbed stars will fall at the harder end of the plot towards the upper right. In addition, at the soft end of the hardness plot, both the temperature and N_H contours exhibit degeneracy, indicating that we cannot uniquely determine a given star's temperature and N_H from its hardness ratios with this model. However, since the majority of the stars observed with HETG have low absorption, we expect most of the stars in X-Atlas to fall close to the leftmost endpoints of the appropriate temperature contour. Under this assumption of low absorption, we can use the HR_2 value of a star as a rough measure of temperature up to around (0.5, -0.6), or ~ 15 MK (~ 1 keV), where the constant temperature contours fall perpendicular rather than parallel to lines of constant N_H .

As noted previously, the high-mass stars show in Figure 30 occupy two distinct ranges at the endpoints of the locus sweeping from $\sim (-0.6, -0.8)$ to $(0.9, 0.6)$, with the majority at the soft end of the plot between approximately $(-0.5, -0.8)$ and $(0.0, -0.7)$ and the remainder falling at the hard end from around $(0.4, -0.3)$ to $(0.9, 0.5)$. The low-mass stars lie in the phase space between these two groups on the hardness plot, with some overlap between the groups. Assuming low absorption, we can identify the group of high-mass stars in the lower left of the plot as corresponding to single-temperature fits of below ~ 7.5 MK (~ 0.5 keV), while the low-mass stars reside in a warmer region between roughly 7.5 and 15 MK (0.5 to 1 keV). The second grouping of high-mass stars is indicative of harder emission and therefore

some combination of higher temperatures and N_H values than are seen in the first group of high-mass stars and the low-mass stars. While the first, cooler high-mass star grouping consists largely of normal OB stars, the second, harder grouping of high-mass stars includes several unusual objects, including the magnetic O star θ^1 Ori C, the Wolf-Rayet stars WR 140 and HD 68273, and peculiar stars Cyg OB2 8A and Gamma Cas. τ Sco, another known magnetic O star, appears in the cooler group of high-mass stars, though at the harder end of that subset. Intriguingly, one star, θ^2 Ori A, has moved from the first high-mass star group to the second in two observations separated by 20 days. This shift between two X-ray emission states is further corroborated by differences in the HETG spectra, quantile measurements and variability tests and is explored further below. For a more thorough discussion of θ^2 Ori A’s variability see Schulz et al. (2006).

Both high-mass star groups fall roughly within the contour lines for both solar and 0.1 times solar abundance. This correspondence suggests that hardness ratios do not provide a useful means of distinguishing high-mass coronal abundances. The low-mass stars, however, do not show good agreement with the Mekal model calculated with solar abundance (Figure 31) but the fit improves dramatically when the non-H abundances are lowered by a factor of 0.1. To some extent, this relatively low abundance value may accurately reflect low coronal abundances in low-mass stars. Scelsi et al. (2007), for example, found that the coronal abundances of 20 X-ray bright pre-main sequence stars were significantly depleted in Fe, with an average of less than 0.2 of the solar photosphere. In addition, spectral fits of the predicted ACIS spectra of low-mass stars generally found abundances in the 0.1 to 0.4 times solar range. However, lowering the abundance may treat the symptoms of deviations between the model and the observations without telling the whole story. For OB stars, Waldron (1994) has shown that if a point on the hardness ratio plot does not fall within the predicted range using ISM opacities, then stellar wind absorption, not a variation in abundance, is most likely responsible for the discrepancy. The presence of multiple X-ray emission components could similarly skew the calculated hardness ratios and imitate a decrease in abundance. In addition, our hardness model depends on the Mekal model’s treatment of abundances in calculating emissivities. Therefore, although the coronae of low-mass stars might conceivably have depleted abundances relative to solar, our model lacks the sophistication to differentiate between actual variations in abundance and other effects.

The models shown in Figures 31 and 32 do account for the outlying observations of WR 140 at approximately (0.42, 0.95) and of η Car between $\sim(0.0, 0.95)$ and $\sim(0.6, 0.95)$. WR 140 was observed pre- and post-periastron with observations separated by five months. The hardness model suggests that some combination of a large shift in column density and a rise in temperature could be responsible for the observed change in hardness. The model does not enable us to characterize the change in temperature, since thermal information is lost in

the hardness plots at high absorption. We can confirm, however, that the HETG spectrum of the post-periastron observation appears strongly absorbed between 1-2 keV in a way not present in the first observation. This discrepancy is most likely due to absorption by the cool WC material along the line of sight between *Chandra* and the region of wind interaction. This observation, then, is the only one that appears strongly affected by absorption besides the six observations of η Car. η Car is a massive, highly-luminous star thought to produce X-rays through wind collisions with a massive companion (Hamaguchi et al. 2007). The spectra from series of *XMM-Newton* and *Chandra* observations have been fit by Hamaguchi et al. (2007), who report kT values ranging from 2.9 to 5.4 keV (33 to 63 MK) and N_H between 4.8 and $42 \times 10^{22}/\text{cm}^2$. The combination of high temperature and high absorption values places η Car at the extreme hard end of the temperature contours in Figures 31 and 32. The appropriate N_H contours for η Car are not shown on the plots.

Both ACIS-I and ACIS-S versions of the hardness plots are available on the X-Atlas web page for each observation, although only the ACIS-I plot is shown here. To see the plots, use the main search page to find an observation, and then click on “Object Spectral Type”. The web page offers the additional capability of quickly identifying and highlighting individual stars of interest for both ACIS-I and ACIS-S plots.

Hardness ratio plots for ACIS-I and ACIS-S are very similar. Any systematic shifts between the ACIS-I and ACIS-S versions of the hardness plots are due to the increased sensitivity at low energy of the back-illuminated S3 chip. This characteristic leads to more counts for soft sources in the “S” passband and hence lower values of HR_2 for the predicted ACIS-S data. While S3 provides a somewhat broader range in HR_2 , the majority of stars observed without benefit of the gratings have been observed on front-illuminated CCDs.

Hardness ratio calculations are most useful if the spectra in question have multiple counts in each passband. While that criterion is certainly met for any of the predicted ACIS spectra in X-Atlas, actual ACIS observations can contain thousands of detectable sources with of order one hundred counts. When a source has few counts or is absorbed, there is a strong likelihood of low counts in one of the three pre-determined passbands. These circumstances can lead to very large and non-uniform errors in hardness calculations due to the location or type of the source.

For such sources, quantile analysis provides an alternative technique to hardness ratios for classifying X-ray sources through X-ray color measurements (Hong et al. 2004). Since the method uses the quantile (in this case quartile) of the source’s own photons, the statistics are uniform across all bands. We have applied the quantile analysis methods to X-Atlas to enable comparisons between faint X-ray sources found in ACIS images and the bright stars observed with HETG.

Like the hardness ratio calculations, quantile analysis is performed on the predicted ACIS-S or ACIS-I aimpoint spectra. Using the methods described in Hong et al. (2004), we take the total predicted counts within a 0.3-8.0 keV range and determine the energies that divide those predicted counts into fractions of 25%, 50%, and 75%. Upon finding $E_{x\%}$, the energy below which $x\%$ of the total counts fall, we calculate normalized quantiles Q_x :

$$Q_x = \frac{E_{x\%} - E_{lo}}{E_{hi} - E_{lo}}, \quad (10)$$

where $E_{lo} = 0.3$ keV and $E_{hi} = 8.0$ keV.

The typical quantile based color-color diagram (QCCD) plots $3*Q_{25}/Q_{75}$, a measure of the emission from the middle half of the spectrum, against the median ($m=Q_{50}$), a measure of the overall hardness of the source, in the form $\log_{10}[m/(1-m)]$. The particular form of the x-axis median expression is chosen to avoid compressing the regions of phase space corresponding to harder X-ray emission (Hong et al. 2004). The ratio of the 75th percentile photon to the 25th percentile photon is a function of both the temperature and the absorption of the source. This dependence means that as the absorption varies, the quantile ratio (Q_{75}/Q_{25}) for a given temperature may be different. In order to interpret the resulting QCCD, we overlay a model grid of hydrogen column depth (N_H) and temperature (kT). This grid is determined from the ACIS-S or ACIS-I aimpoint ARF and combined interstellar absorption and Raymond-Smith (1977) thermal models (Figures 33, 34). We used Raymond-Smith plasma (Raymond & Smith 1977) for general purpose fitting of low resolution coronal spectrum. While more recent models including MeKa (Mewe et al. 1985) and APEC (Smith et al. 2001) have more lines included, Raymond-Smith models were found by Wolk et al. (2006) to have the lowest residual χ^2 (degree of freedom) and/or less outliers in a direct comparison of fitting about 80 moderately bright stellar sources using Sherpa. The same study found that all three models gave similar results for kT and nH for stars with between 100 and 1000 counts. On the quantile plots Figures 33 and 34 one can distinguish changes in temperature from extinction and even thermal and non-thermal changes. Further, the grids shown in Figures 33 and 34 are sensitive to metallicity.

Two things become immediately clear from these plots. First, as noted previously, the vast majority of stars observed with HETG had relatively low absorption. No low-mass star exceeds $\sim N_H 5 \times 10^{21} \text{ cm}^{-2}$ and only about five high-mass stars exceed that value. Second, while low-mass stars are smoothly distributed along the temperature axis in this plot, with temperatures ranging from about 1 to 3 keV, the high-mass stars are clearly congregated at the edges. The appropriate one-temperature representations appear to be either below about 1 keV or above about 3 keV with few high-mass stars occupying the middle ground dominated by the low-mass stars. This distribution has two clear implications. First, the X-ray generation mechanism is clearly different between the high and low-mass stars. This

result is not unexpected, as many other lines of argument have led to the development of various dynamo-driven models for the generation of X-rays in low-mass stars. More surprising is the bimodal distribution of high-mass stars, which suggests that two different physical states are at work. A similar bimodality was noted in the hardness ratios of the high-mass stars (Figure 30), and as expected, the same stars that appear at the warmer, harder end of the hardness ratio plot generally lie in the high-temperature group on the quantiles plots. Once again, θ^2 Ori A has moved from one group to the other between the two observations.

Chandra grating spectra have provided material for deliberation about complexities and puzzles in high-mass star interpretation. There are a number of possible explanations for high-mass stellar X-ray emission relevant to X-Atlas. Colliding winds in binaries provide high temperature plasma in some cases (e.g. Hamaguchi et al. (2007)), while magnetic activity plays a role in others. Quantile measurements of stars in the atlas reveal that about 50% of the high-mass sample is cool with one-temperature component fits below ~ 1 keV. This result is consistent with the standard model of X-rays originating in shocked material in line-driven spherically symmetric winds (MacFarlane et al. 1991). Typical temperatures in these models are about 10MK (~ 900 eV). Hot X-ray emission from OB stars has been the subject of recent investigations. Schulz et al. (2000, 2001, 2003) reported temperatures of about 5 keV from θ^1 Ori C. Schulz et al. conclude that the component of the emission at this temperature must be formed “near the terminal velocity of the wind,” at about seven stellar radii from the photosphere. Gagné et al. (2005) show that such emission can be fitted by a two-dimensional MHD magnetospheric wind model due to ud-Doula & Owocki (2002). Several other examples of X-ray hot O and B stars have since been found (Lopes de Oliveira et al. 2006; Rakowski et al. 2006). Mullan & Waldron (2006) have proposed a two-component scenario by which the cooler X-ray emission is generated by line-driven, spherically-symmetric winds, and a second component of the wind emerges from magnetically active regions in polar caps that may extend as low as 45° . In such a scenario, whether an O star is found to be a relatively hot or soft source may simply be a function of inclination.

We note that in the star-forming region RCW 108, about 75% of the OB star candidates in the field are found to have X-ray temperatures above 3 keV (Wolk et al. 2007). The fraction of high-temperature stars was greatest in the RCW 108–IR embedded cluster, which is still actively forming stars. The inner group indicates an evolutionary aspect to the observed temperature, in contradiction of models that propose that the observed temperature may be a function of the observation’s line-of-sight unless the extent of the polar cap decreases in time. X-Atlas contains a sample of relatively old high-mass stars in which the cooler variety are in the majority. This characteristic may indicate that X-ray temperatures in high-mass stars decline with time, just as they do in cool stars, although the X-ray

generation mechanisms are different.

The various types of low-mass/cool stars studied with *Chandra* seem to be very tightly correlated in Figure 34. For example, the bulk of the F and G stars lie between y-axis values of 1.75 and 1.95, while the general RS CVn and T Tauri star populations have y-axis values between 1.4 and 1.7. We ran model grids at several metallicities ranging from 0.001 to 5 times solar. While no particular metallicity seemed to improve the relation between the positions of the high-mass/hot stars and the model grids, we found that for low-mass/cool stars with cool coronae at < 1 keV, a best fit to the data was a metallicity of about 0.3. For the warmer coronae, the best fit was a metallicity of about 0.1 (See Figure 34). The fact that the stars are still tightly correlated despite the high metal sensitivity of the model grids is indicative of very uniform metallicity among the observed coronae. This leads us to believe that the handling of the metallicity by the models as a function of temperature, not a change in the metallicity, is the root of the apparent metallicity discontinuity. Indeed, given the sensitivity of quantiles to metallicity shown here, the metallicity must be very similar in all the observed low-mass/cool star coronae.

4.2. Variability Analysis

Variability studies allow us to assess the plausibility of different X-ray generation mechanisms. These can be constrained by the timescales and flux changes observed in the variability. Specifically, for low mass stars, the cooling time depends on the loop length, plasma density, conductivity and emissivity (See Reale (2002) for a review). Testa et al. (2004) undertook one such study based on 26 observations of 22 low-mass stars observed with HETG during the first three years of the *Chandra* mission. They concur with the findings of Huenemoerder et al. (2001) who found that while the continuum emission changes significantly during flares, the line emission does not. However, this is not uniformly the case. Audard et al. (2001) found that in the case of the RS CVn HR 1099 Ne stays constant at the quiescent level during a flare but the detected a flux increase in the Fe XXIV lines during a flare. Güdel et al. (2001) also found enhancement in the Fe XXIV lines during a flare of the rapidly rotating ZAMS star AB Dor.

A large proportion of the stars in X-Atlas appear to be variable. To test for variability in the flux level over the course of an observation, we constructed light curves and performed variability analysis on the observations using two methods. The first method was simple binning. *ACIS Grating Light Curve (aglc)*¹¹ was used to create light curves from the HEG

¹¹<http://space.mit.edu/cxc/analysis/aglc/index.html>

and MEG HETG data. Light curves with bin sizes of 4000 and 1200 seconds were extracted.

In a more quantitative approach, all observations were analyzed using the algorithms developed by Gregory & Loredó (1992) as adapted specifically for *Chandra* data (Rots 2006). This algorithm uses maximum-likelihood statistics and evaluates a large number of possible break points against the prediction of constancy.

An overview of the Gregory–Loredó analysis is presented in Table 7. At the time of this analysis there were 131 observations of 64 sources (24 hot stars and 40 cool stars) in the database. The criteria for variability was the probability returned by the Gregory–Loredó test. If the probability exceeded 99% the star was considered "variable." If the probability was between 90% and 99%, the star was deemed "probably variable." Stars with variability probability below 90% were considered "not variable." A source was considered variable if any observation of that source was noted to be variable. Epoch to epoch comparisons were not undertaken in a systematic way for this study.

Table 7 is designed only to give an example of the content of the database. The high-mass star classification combines single OB stars, multiple OB stars and Wolf-Rayet stars. We find a variability rate of $\sim 40\%$ among the high-mass stars. This is a remarkably high rate since the X-ray production mechanisms of high-mass stars are expected to be wind driven and hence more stable than dynamo-driven low-mass stars, which are subject to loop reconnection at all scales. A closer examination of the data reveals that of the variables, several are unique objects, including Algol, γ Cas, θ^1 Ori C, and η Carina.

Although it contains a B8 star, Algol also contains a K1 subgiant. The latter tends to be active. The flare seen from Algol *is of particular interest*, though, as it appears to have induced a change in the apparent characteristic flux level. HD 150136, 9 Sgr, τ Sco, τ CMa and HD 206267 are generally well-behaved OB stars that all exhibited small deviations on short time scales (10-20 ks). γ Cas is a unique hot star that shows fluctuations of about 25% on short time scales. The variability of θ^1 Ori C has been previously reported (Schulz et al. 2001; Gagné et al. 2005) and is thought to be related to its relatively high temperature and strong variable magnetic field. Support for this hypothesis comes from the observations of θ^2 Ori A (discussed in further detail in Schulz et al. (2006)). This star shows variability in only one of its two HETG observations but is also seen to shift from a cool to a hot state as evidenced by the two-temperature fit in which the kT value jumps from a single temperature of around 0.7 keV in epoch one to two temperatures of approximately 17 and 2 keV in epoch two (Table 5). The flux is seen to drop steadily and by 25% over the course of the hotter, but generally brighter, epoch.

About 85% of the low-mass stars are found to be variable. This proportion is well in

excess of the typical fraction reported in star forming regions, which is about 30% in a 100 ks observation (Cf. Getman et al. (2002); Wolk et al. (2006)). This apparent discrepancy is undoubtedly due to counting statistics and selection effects. Wolk et al. (2007) report that in a 90 ks observation of RCW 108, 66% of stars with over 200 counts are detected as variable but only 21% of stars with between 100 and 200 net counts. In the X-Atlas database almost all the stars are bright and have over 1000 0^{th} -order counts. The results for low-mass stars here are consistent with the results of the COUP survey (Getman et al. 2005) which found the majority of the ~ 1600 stars monitored for ~ 10 days to be variable at some level.

With the exception of the composite system Algol, no high-mass star was seen to flare. Among the low-mass stars, TZ CrB, CC Eri, TW Hya, and DoAr 21 showed the strongest flares, more than doubling their flux in less than one hour with cooling times in excess of 10 ks. The cooling time of stars with disks, such as TW Hya, is of particular interest since the cooling time is related to the loop length. Such systems can provide direct evidence of star-disk coupling via the magnetic field. While these are the longest cooling times in the group, 10-30 ks is not unusually long (cf. Favata et al. (2005)). The X-Atlas database is a very biased sample for flare studies. Many stars were targeted precisely because they were known flare stars (e.g. AD Leo, EV Lac, and CC Eri) or rotationally variable (e.g. HD 223460, FK Com and AB Dor).

4.3. Variability of Capella

Over twelve observations from 1999 to 2006, Capella’s X-ray hardness ratios are clustered at $(HR_1, HR_2) = (-0.75 \pm 0.01, -0.058 \pm 0.025)$ (see Figure 30). These are significantly overdispersed compared to the typical errors in the individual hardness ratios, by factors ranging from 5x to 12x. Over this same period, the overall X-ray count rate undergoes variations of $\approx 17\%$. However, the hardness ratios are uncorrelated with the count rates: we find correlations of Spearman’s $\rho = -0.033$ ($p = 0.9$) for HR_1 versus rate, and $\rho = 0.11$ ($p = 0.7$) for HR_2 versus rate.

Within each observation, there is no evidence for any variability, as is confirmed by an application of the Gregory-Loredo test (Gregory & Loredo 1992): the odds that the star varies during any of the individual observation is $< 90\%$. In contrast, combining 15 of the 16 available observations (excepting ObsID 1199, a 2 ks observation) to construct a concatenated event list spanning over 350 ks, and applying the same test to this concatenated events list, we find that the odds of Capella being variable are 10:1, indicating a probability of over 0.99 that Capella is variable on timescales of years.

Capella, as the strongest coronal source, has been a common X-ray calibration target for many instruments. It has remained stable in its total X-ray output even as the detailed emission structure has shown considerable change (see e.g., Young et al. (2001)). For instance, Dupree & Brickhouse (1996) have shown based on EUVE data that the high-temperature component is variable, a finding confirmed by Raassen & Kaastra (2007) based on LETG data. There is also considerable evidence for the dominant emission to change between the G1 III primary and the G8 III secondary (e.g., Linsky et al. (1998); Johnson et al. (2002); Ishibashi et al. (2006)).

We confirm the primary conclusions of Raassen & Kaastra (2007), who found no evidence of changes in intensity over timescales of < 100 ks, but a large timescale variation that resulted in an increased flux early 2006. We find no evidence for variations at timescales < 50 ks, and conclusively find that the source is variable over larger timescales.

5. SUMMARY

By developing a uniformly processed stellar database, we intend to provide a powerful yet accessible tool for the study of stellar X-ray emission. As the early science results from X-Atlas demonstrate, the ability to compare the high-mass and low-mass stars observed with HETG opens up intriguing avenues of investigation. The spectral montages and line-profile plots created from the high-resolution HETG data offer a detailed glimpse at the physical mechanisms for X-ray generation among stellar types. In addition, by convolving the high-resolution spectra to low-resolution, we can compare the limited number of stars studied in high-resolution to the thousands of sources in *Chandra* images. Spectral fits and X-ray color analyses performed on the predicted low-resolution spectra reveal differences in the X-ray temperature distributions of high-mass and low-mass stars and provide evidence for at least two distinct classes of X-ray emission in high-mass stars. Variability studies help to further constrain the causes of stellar X-ray emission and suggest that the proportion of high-mass stars exhibiting X-ray variability may be greater than previously suspected. We also definitively establish the X-ray variability of Capella over timescales of years. We have made available the means to conduct systematic studies of the stellar HETG dataset, and therefore hope that these early results will represent only the beginnings of the scientific return of the database. Finally, we have applied the reduction and analysis methods described above to all non-stellar point sources observed with HETG, including neutron stars, X-ray binaries, and active galactic nuclei. Future releases of X-Atlas will adapt these methods to LETG point source observations as well, extending the atlas to all *Chandra* gratings observation of point sources.

We are happy to thank the referee John Pye for a careful reading and a number of improvements. Funding for this work was provided by *Chandra* Grants GO5-6006E and GO5-6007A, Chandra X-ray Center NASA Contract NAS8-39073, and by ANCHORS (AN archive of CHandra Observations of Regions of Star formation), *Chandra* archival project AR5-6002A. Wayne L. Waldron was supported in part by *Chandra* grant GO5-6006A.

We would like to thank N. S. Schulz, D. P. Huenemoerder, and P. Testa for feedback during the testing stages of the project.

REFERENCES

- Audard, M., Güdel, M., & Mewe, R. 2001, *A&A*, 365, L318
- Brickhouse, N. S., Dupree, A. K., Edgar, R. J., Liedahl, D. A., Drake, S. A., White, N. E., & Singh, K. P., 2000, *ApJ*, 530, 387
- Canizares et al., 2000, *ApJ*, 539, L41
- Canizares, C. R., Davis, J. E., Dewey, D., Flanagan, K. A., Galton, E. B., Huenemoerder, D. P., Ishibashi, K., Markert, T. H., Marshall, H. L., McGuirk, M., Schattenburg, M. L., Schulz, N. S., Smith, H. I., Wise, M., 2005, *PASP*, 117, 1144
- Chandra Interactive Analysis of Observations (CIAO), <http://cxc.harvard.edu/ciao/>
- Chandra X-ray Center, 'The Chandra Proposers' Observatory Guide,' Vers. 8.0, Cambridge, MA: Dec. 2005
- Corcoran, M. F., Hamaguchi, K., Henley, D. B., Ishibashi, K., Gull, T., Nielsen, K., Pittard, J. M., 2005, *BAAS*, 37, 1347
- De Becker, M., Rauw, G., & Swings, J. P., 2004, *Ap&SS*, 297, 291
- De Marco, O., & Schmutz, W., 1999, *A&A*, 345, 163
- Donati, J.-F., Howarth, I. D., Jardine, M. M., Petit, P., Catala, C., Landstreet, J. D., Bouret, J.-C., Alecian, E., Barnes, J. R., Forveille, T., Paletou, F., and Manset, N. 2006, *MNRAS*, 370, 629
- Drake, J. J., Ratzlaff, P., Kashyap, V., Edgar, R., Izem, R., Jerius, D., Siemiginowska, A., Vikhlinin, A., 2006, *Proc. SPIE*, 6270, 62701I
- Dupree, A.K., & Brickhouse, N.S., 1996, in *Poster Proc., IAU Symp. 176: Stellar Surface Structure* (Wien: Institut für Astronomie), 184
- Evans, N. R., Seward, F. D., Krauss, M. I., Isobe, T., Nichols, J., Schlegel, E. M., Wolk, S. J., 2003, *ApJ*, 589, 509
- Favata, F., Flaccomio, E., Reale, F., Micela, G., Sciortino, S., Shang, H., Stassum, K. G., Feigelson, E. D., 2005, *ApJS*, 160, 469
- Fruscione, A., 2006, *Proc. SPIE*, 6270, 62701V, D. R. Silvia & R. E. Doxsey, eds.
- Gagné, M., Oksala, M. E., Cohen, D. H., Tonnesen, S. K., ud-Doula, A., Owocki, S. P., Townsend, R. H. D., & MacFarlane, J. J., 2005, *ApJ*, 628, 986

- Getman, K. V., Feigelson, E. D., Townsley, L., Bally, J., Lada, C. J., Reipurth, B., 2002, *ApJ*, 575, 354
- Getman, K. V., et al., 2005, *ApJS*, 160, 319
- Gies, D. R., et al., 1993, *AJ*, 106, 2072
- González-Riestra, R. & Rodríguez-Pascual, P. M., 2007, “BiRD: A Browsing Utility for RGS Spectra,” X-ray Spectroscopy Workshop, July 11-13
- Gregory, P. C. & Loredó, T. J., 1992, *ApJ*, 398, 146
- Güdel, M., et al. 2001, *A&A*, 365, L336
- Hamaguchi, K., et al., 2007, *ApJ*, 663, 522
- Harnden, F. R., Jr., Branduardi, G., Gorenstein, P., Grindlay, J., Rosner, R., Topka, K., Elvis, M., Pye, J. P., & Vaiana, G. S., 1979, *ApJ*, 234, L51
- Hong, J., Schlegel, E. M. & Grindlay, J. E., 2004, *ApJ*, 614, 508
- Houck, J. C., & Denicola, L. A., 2000, in *ASP Conf. Ser. 216: Astronomical Data Analysis Software and Systems IX*, Vol. 9, 591
- Huenemoerder, D. P., Ramsey, L. W., Buzasi, D. L., Nations, H. L., 1993, *ApJ*, 404, 316
- Huenemoerder, D. P., Canizares, C. R., & Schulz, N. S., 2001, *ApJ*, 559, 1135
- Ishibashi, K., Dewey, D., Huenemoerder, D. P., & Testa, P., 2006, *ApJ*, 644, 117
- Johnson, O., Drake, J. J., Kashyap, V., Brickhouse, N. S., Dupree, A. K., Freeman, P., Young, P. R., & Kriss, G.A., 2002, *ApJ*, 565, 97
- Kaastra, J. S., 1992, ‘An X-Ray Spectral Code for Optically Thin Plasmas, Internal SRON-Leiden Report, version 2.0
- Kashyap, V. L. & Drake, J. J., 2000, *BASI*, 28, 475
- Liedahl, D. A., Osterheld, A. L., & Goldstein, W. H., 1995, *ApJ*, 438, 115
- Linsky, J. L., Wood, B. E., Brown, A., & Osten, R. A., 1998, *ApJ*, 492, 767
- Lopes de Oliveira, R., Motch, C., Haberl, F., Negueruela, I., & Janot-Pacheco, E., 2006, *A&A*, 454, 265

- MacFarlane, J. J., Cassinelli, J. P., Welsh, B. Y., Vedder, P. W., Vallergera, J. V., & Waldron, W. L., 1991, *ApJ*, 380, 564
- Maíz-Apellániz, J., Walborn, N. R., Galué, H. Á., Wei, L. H., 2004, *ApJS*, 151, 103
- Mewe, R., Gronenschild, E. H. B. M., & van den Oord, G. H. J., 1985, *A&A*, 62, 197
- Mewe, R., Lemen, J. R., & van den Oord, G. H. J., 1986, *A&A*, 65, 511
- Millour, F., et al., 2007, *A&A*, 464, 107
- Morrison, R. & McCammon, D., *ApJ*, 270, 119
- Mullan, D. J. & Waldron, W. L., *ApJ*, 637, 506
- Park, T., Kashyap, V. L., Siemiginowska, A., van Dyk, D. A., Zezas, A., Heinke, C., Wargelin, B. J., 2006, *ApJ*, 652, 610
- Preibisch, T., 1999, *A&A*, 345, 583
- Raassen, A. J. J., Kaastra, J. S., *A&A*, 461, 679
- Rakowski, C. E., Schulz, N. S., Wolk, S. J., & Testa, P., *ApJ*, 649, L111
- Raymond, J. C. & Smith, B. W., 1977, *ApJS*, 35, 419
- Reale, F., 2002, in *ASP Conf. Ser.*, Vol. 277, 103
- Rots, A. H., 2006, in *ASP Conf. Ser. 351: Astronomical Data Analysis Software and Systems XV*, Vol. 351, 73
- Schulz, N. S., Canizares, C. R., Huenemoerder, D., & Lee, J. C., 2000, *ApJ*, 545, 135
- Schulz, N. S., Canizares, C., Huenemoerder, D., Kastner, J. H., Taylor, S. C., & Bergstrom, E. J., 2001, *ApJ*, 549, 441
- Schulz, N. S., Canizares, C., Huenemoerder, D., Tibbets, K., 2003, *ApJ*, 595, 365
- Schulz, N. S., Testa, P., Huenemoerder, D. P., Ishibashi, K., & Canizares, C. R., 2006, *ApJ*, 653, 636
- Scelsi, L., Maggio, A., Micela, G., Briggs, K., & Gudel, M., preprint (astro-ph 0707.2857)
- Schmidt-Kaler, T., 1982, *Landolt-Börnstein, Group VI, Vol 2b*, eds. K. Schaifers and H. H. Voigt (New York: Springer Verlag), 14

- Seward, F. D., Forman, W. R., Giacconi, R., Griffiths, R. E., Harnden, F. R., Jr., Jones, C., & Pye, J. P., 1979, *ApJ*, 234, L55
- Seward, F. D. & Chlebowski, T., 1982, *ApJ*, 256, 530
- SIMBAD Astronomical Database, Strausborg, France
- Smith, R. K., Brickhouse, N. S., Liedahl, D. A., Raymond, J. C. 2001, *ApJ*, 556, L91
- Smith, M. A., Cohen, D. H., Gu. M. F., Robinson, R. D., Evans, N. R., Schran, P. G., 2004, *ApJ*, 600, 972
- Testa, P., Drake, J. J., & Peres, G., 2004, *ApJ*, 617, 508
- ud-Doula, A. & Owocki, S. P., 2002, *ApJ*, 576, 413
- van der Hucht, K. A., 2001, *New A Rev.*, 45, 135
- Walborn, N. R., *The UV Universe: Stars from Birth to Death*, 2006, 26th Meeting of the IAU, Joint Discussion 4, Prague, Czech Republic, 1
- Waldron, W. L., 1994, *AIP Conf. Proceed.*, 313, 279
- Weisskopf, M. C., Brinkman, B., Canizares, C., Garmire, G., Murray, S., Van Speybroeck, L. P., 2002 *PASP*, 114, 1
- White, N. E., Holt, S. S., Boldt, E. A., & Serlemitsos, P. J., 1980, *ApJ*, 239, 69
- Wolk, S. J., Spitzbart, B. D., Bourke, T. L., & Alves, J., 2006, *ApJ*, 132, 1100
- Young, P. R., Dupree, A. K., Wood, B. E., Redfield, S., Linsky, J. L., Ake, T. B., & Moos, H. W., 2001, *ApJ*, 555, L121

X-Atlas Database Query

Observation ID: Sequence Number: Science Category: ALL

Target Name: Spectral Type: Object Type:

Observer Name: Project Title: Gratings:

Observation Date Public Date between and

RA: (decimal degrees) Dec: (d. d.) Radius: (d. d.)

Sort Results By: Spectral Type

[Search](#) [Clear Fields](#)

[X-Atlas Home](#) [X-Atlas Target Listing](#) [X-Atlas Spectral Metrics Listing](#) [X-Atlas Spectral Fits Listing](#)

8 observations selected.

Select up to three targets for plotting:

Target 1: 4 - Theta-1 On C Grating Arm: MEG Order: 1

Target 2: 599 - IOTA ORIONIS Grating Arm: MEG Order: 1

Target 3: 4473 - Theta-2 On A Grating Arm: MEG Order: 1

[Quick Plot](#)

Option A: View pre-produced plots of the HEG or MEG HETG spectra of the selected targets

Plot Range: [View Plots](#)

Option B: Customize the output plots

Input desired plotting parameters and click 'Generate Plots' below.

1. Select desired datasets:

High-Resolution HETG/ACIS-S Spectrum

Predicted ACIS-S Aimpoint Low-Resolution Spectrum Predicted ACIS-I Aimpoint Low-Resolution Spectrum

Zeroth-Order HETG/ACIS-S Spectrum Predicted Zeroth-Order Spectrum

2. Select desired plot units:

Wavelength: counts/Å vs. Å counts/Å bin vs. Å

photons/Åcm² vs. Å (High-Resolution HETG/ACIS-S spectra only)

Energy: counts/keV vs. keV counts/channel vs. keV

3. Specify wavelength or energy range and additional plotting parameters

Low Bound: High Bound:

Scale the low-resolution spectra to the HETG spectrum: Yes No

Boxcar smoothing: Number of bins over which to average the HETG spectrum No smoothing 3 4 8 20

Set upper y-axis bound: counts

Specify resolution of output plots: Width: pixels Height: pixels

[Generate Plots](#) [Reset Fields](#)

X-Atlas Database: Search Results

13 records retrieved

Select observation(s) to plot spectral data interactively

Click on «Object Name» to preview an observation

Click on «Observation ID» # to view instrument configuration data

Click on «Spectral Type» to view X-ray hardness and quantile plots

Click on «Observer» to view publications associated with the observation

*Note that 'Observation Name' refers to the name given by the observer for the observation, and 'Object Name' refers to the object within that observation for which we have extracted a spectrum.

Select	Observation ID	Observation Date	Observation Name ^a	Object Name	Object Spectral Type	Aimpoint RA	Aimpoint DEC	Observer
<input type="checkbox"/>	4512	2004-03-22 02:10:13	Xi Per	Xi Per	O7.5III(n)(f)	59.743204	35.781508	Dr. Derek Mas
<input type="checkbox"/>	3738	2003-08-12 20:59:02	HD37468	Sigma Ori	O9.5V+B0.5V	84.685142	-2.590523	Dr. Stephen Skinner
<input type="checkbox"/>	3753	2003-12-12 12:06:50	EPSILON ORI	EPSILON ORI	B0f	84.051765	-1.203858	Dr. Wayne Waldron
<input type="checkbox"/>	3745	2003-05-02 11:57:20	ETA CARINAE	ETA CARINAE	3p	161.268556	-59.694007	Dr. Michael Corcoran
<input type="checkbox"/>	3746	2003-07-20 01:47:26	ETA CARINAE	ETA CARINAE	3p	161.248293	-59.689220	Dr. Michael Corcoran
<input type="checkbox"/>	3747	2003-09-26 22:46:56	ETA CARINAE	ETA CARINAE	3p	161.249380	-59.678969	Dr. Michael Corcoran
<input type="checkbox"/>	3748	2003-06-16 05:36:31	ETA CARINAE	ETA CARINAE	3p	161.254642	-59.692649	Dr. Michael Corcoran
<input type="checkbox"/>	3731	2003-08-26 08:48:55	HD 220657	HD 220657	F8IV	351.347282	23.404897	Dr. Frank Harnden Jr.
<input type="checkbox"/>	3756	2003-10-20 14:45:17	V987 TAU = HDE 283572	V987 TAU = HDE 283572	G2III	65.497301	28.300841	PROF. STEVE KAHN
<input type="checkbox"/>	3755	2003-11-27 09:43:46	SU AUR	SU AUR	G2IIIvar	74.000094	30.567023	DR. KESTER SMITH

High-Resolution MEG Spectrum, order = 1; ObsID 599

High-Resolution MEG Spectrum, order = 1; ObsID 4474

Standard Data Products: Aimpoint ARF, Aimpoint RMP, ACIS-S/ACIS-I/ACIS-S/ACIS-I

For additional line identification, use [ATOMDB](#).

To retrieve an observation from the Chandra Data Archive, use [WebChandra](#)

Fig. 1.— The X-Atlas web interface. The database can be searched on a variety of observation and target parameters (*top left*) and the basic astrophysical parameters, spectra, X-ray color data, and variability of sources in the observations can be previewed (*top right*). After selecting observations of interest, customized spectral plots of up to three sources of interest can be created (*bottom left*) and both the output plots and spectral data for those sources can be retrieved, including the high-resolution HEG and MEG spectra and the predicted low-resolution ACIS-S and ACIS-I spectra.

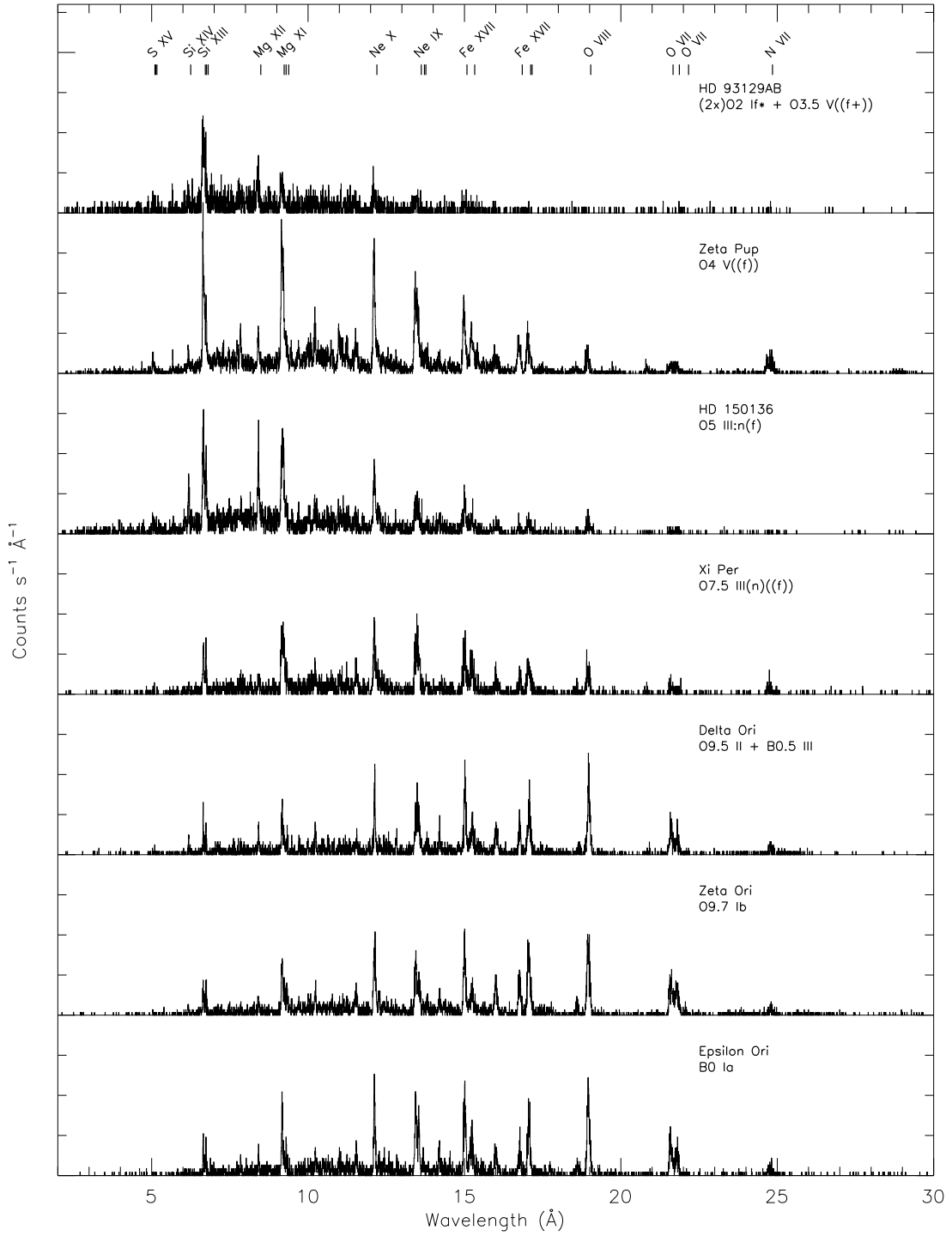


Fig. 2.— Montage of the high-resolution MEG spectra ($[\text{counts/s}/\text{\AA}]$) of normal OB supergiants and giants, ordered by spectral class. The locations of some strong lines are marked. The spectra from different sources are offset for clarity.

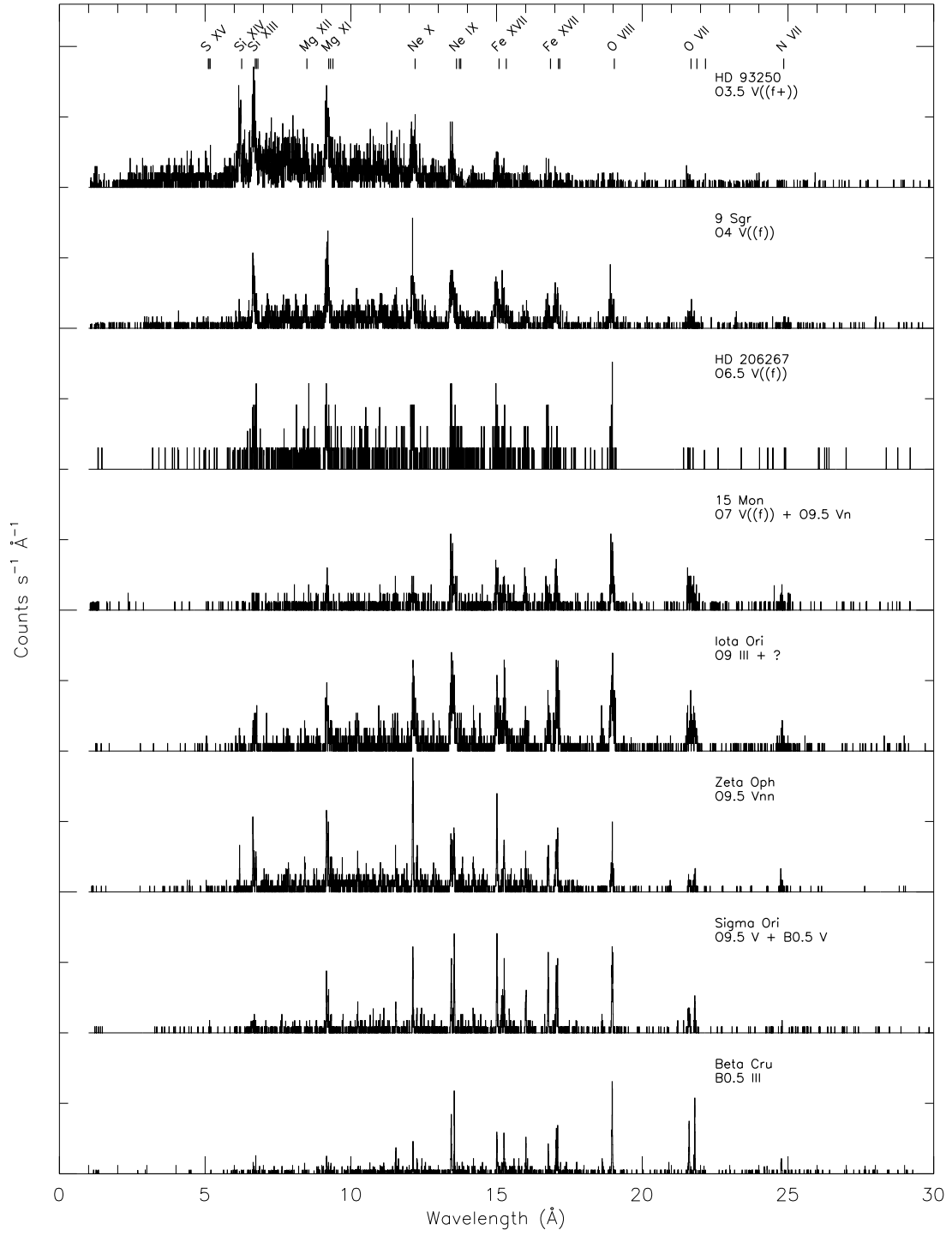


Fig. 3.— As in Figure 2, for normal OB giants, sub-giants and dwarfs.

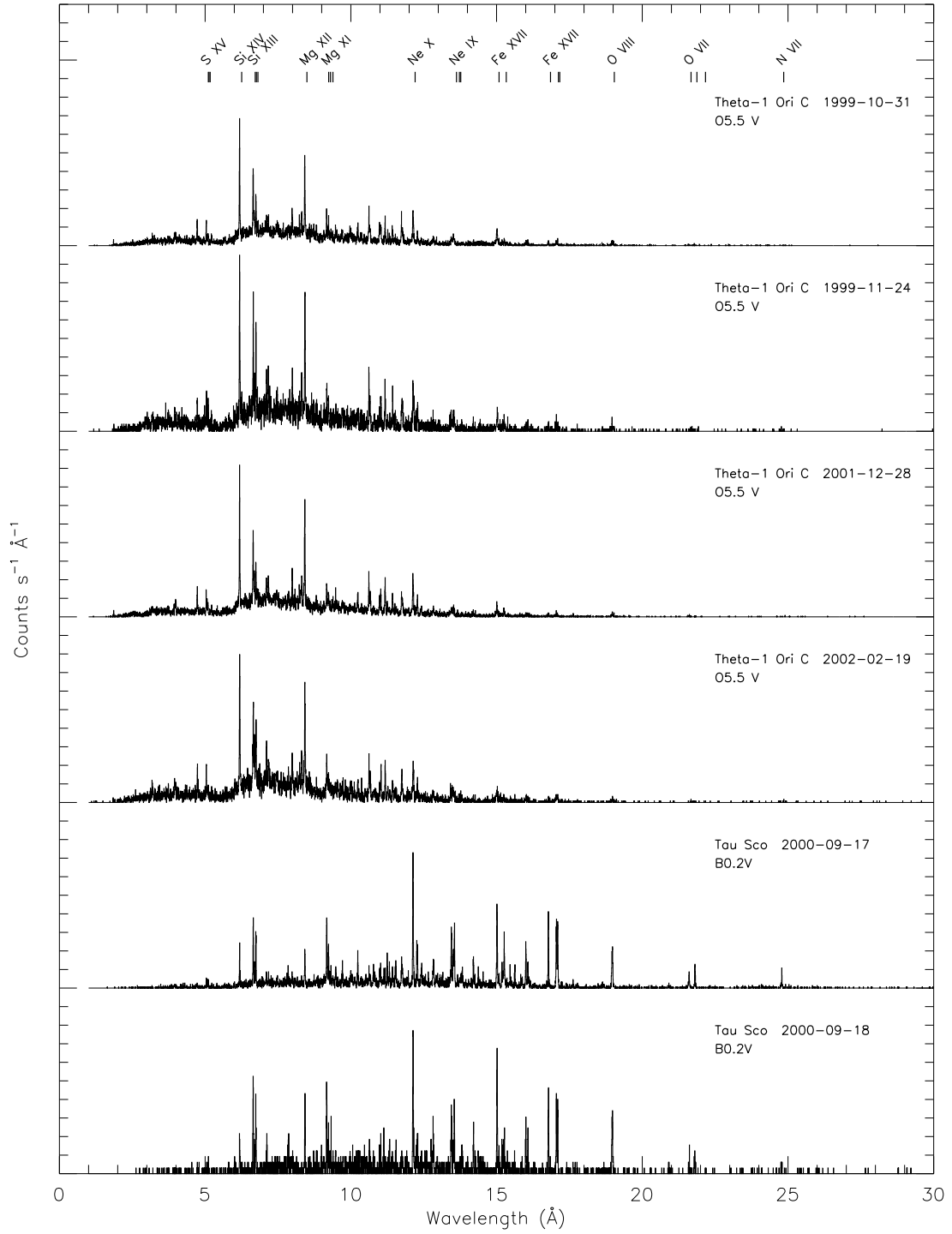


Fig. 4.— As in Figure 2, for four observations θ^1 Ori C and two observations of τ Sco, two high-mass stars thought to possess magnetic fields responsible for generating X-rays.

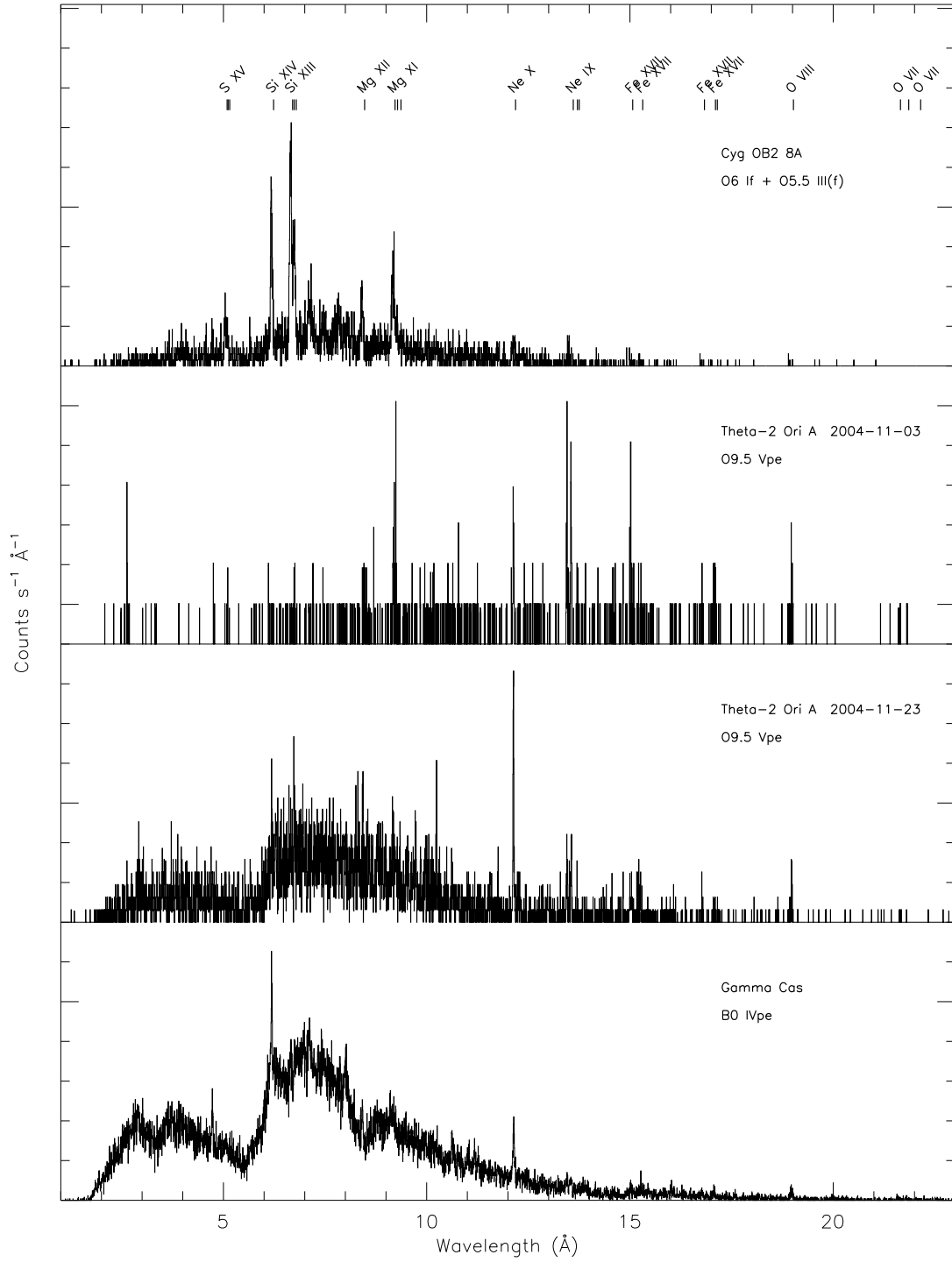


Fig. 5.— As in Figure 2, for three peculiar OB stars, γ Cas, Cyg OB2 8A, and θ^2 Ori A, approximately ordered by X-ray hardness, descending from hardest to softest.

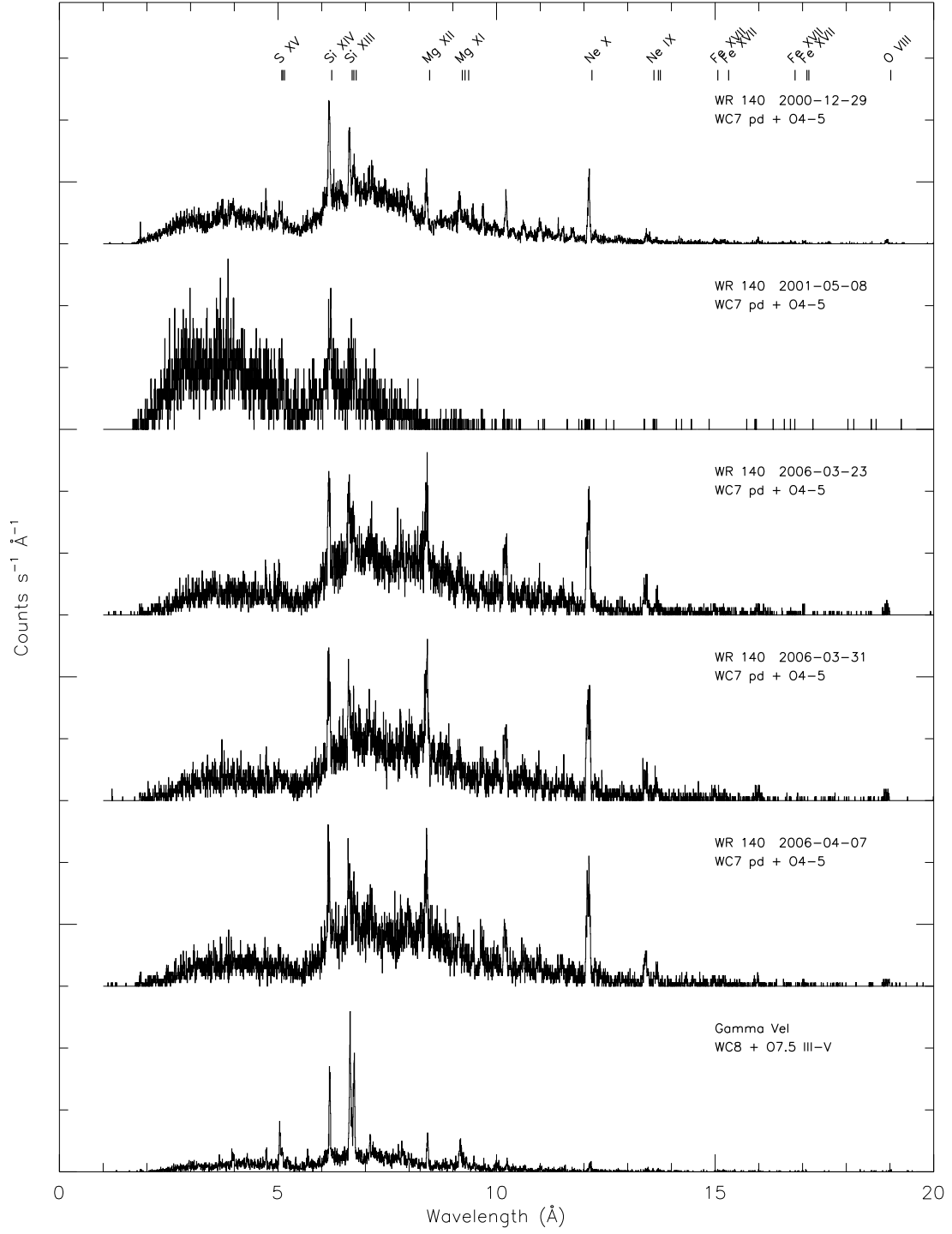


Fig. 6.— As in Figure 2, for two Wolf-Rayet stars observed thus far with HETG.

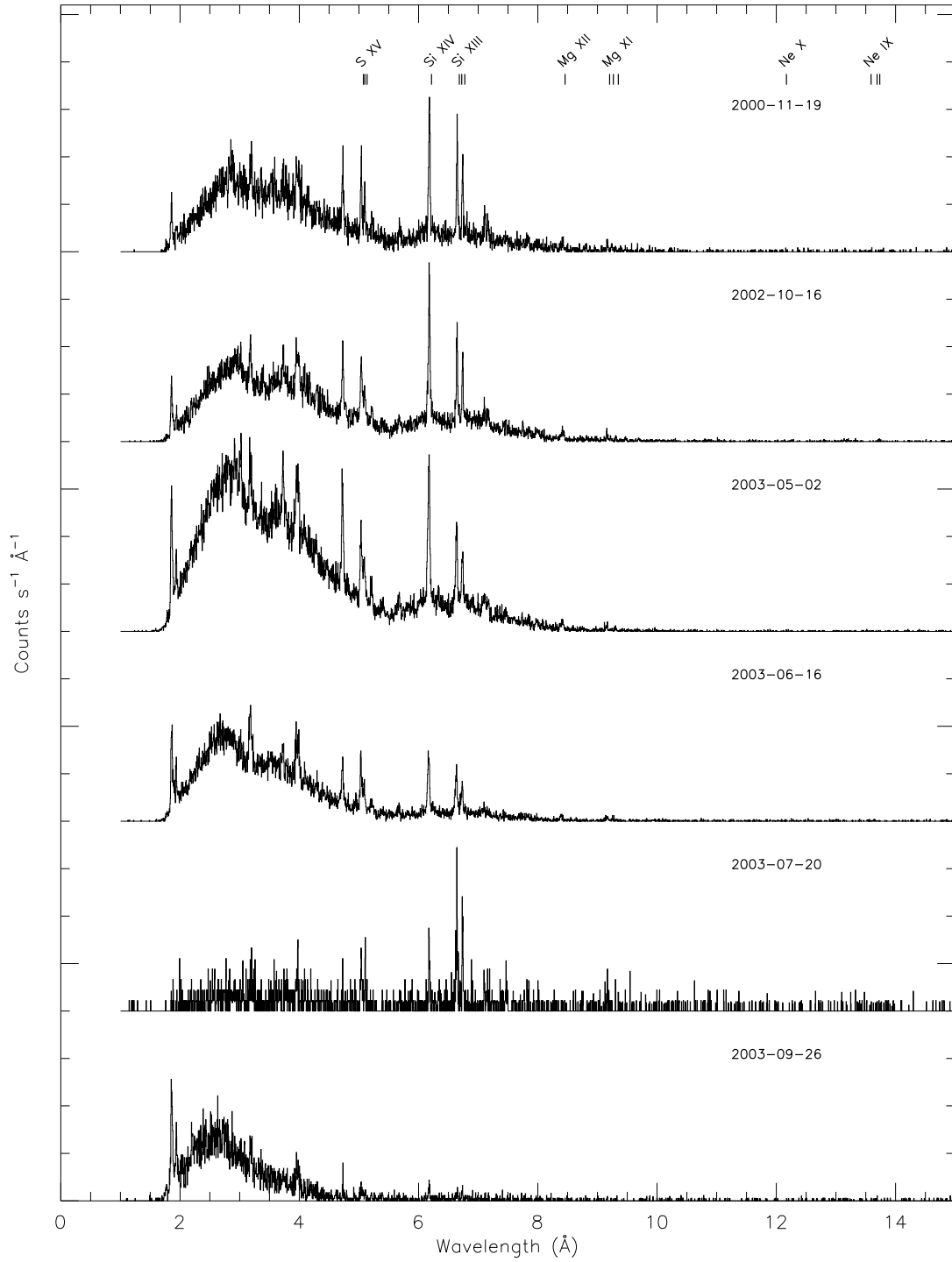
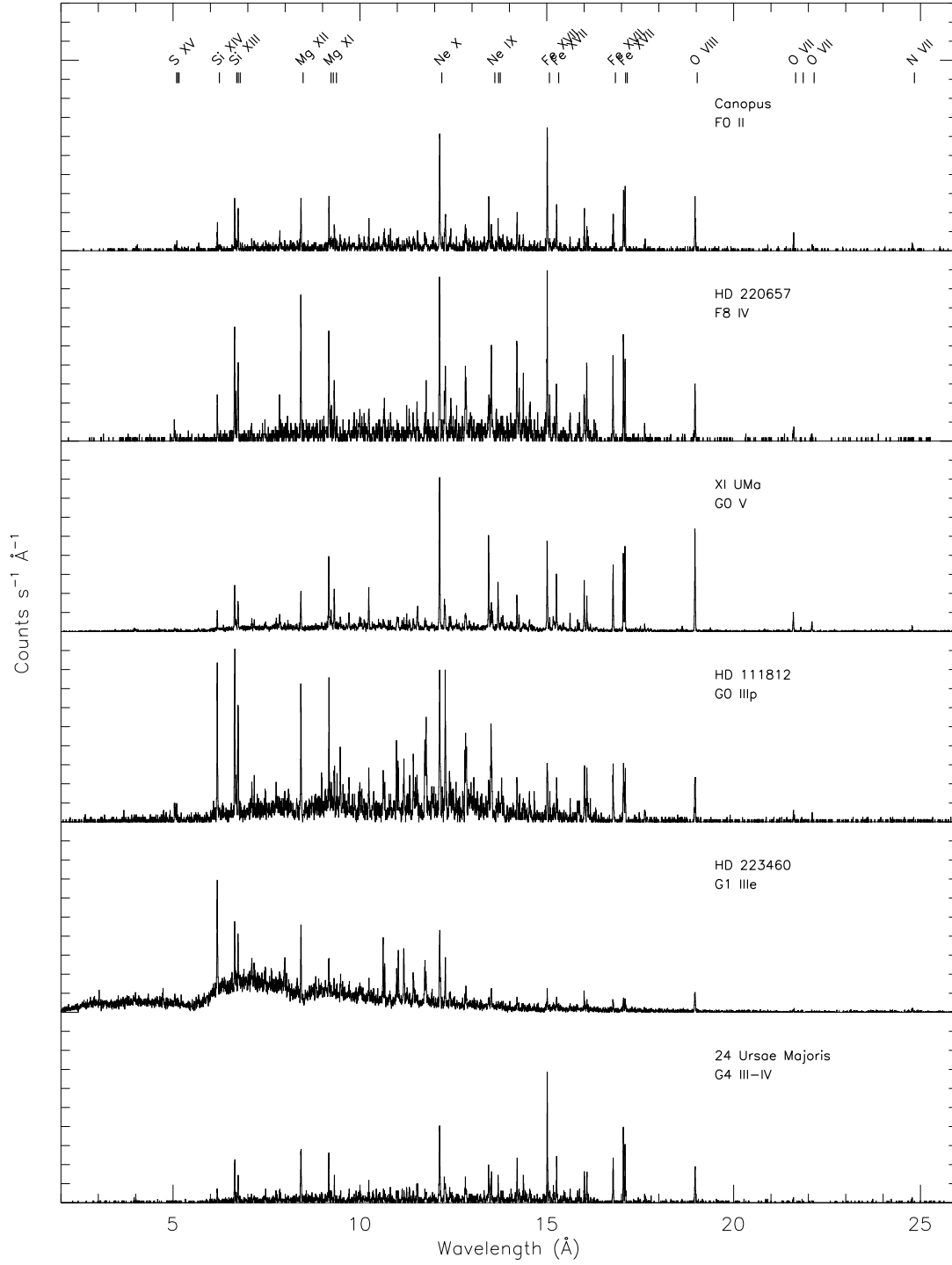


Fig. 7.— As in Figure 2, for six HETG observations of η Carinae. η Carinae underwent an X-ray eclipse in mid-2003: the 2003-05-02 observation was made close to X-ray maximum, and the 2003-07-02 observation was taken near X-ray minimum (Corcoran et al. 2005).



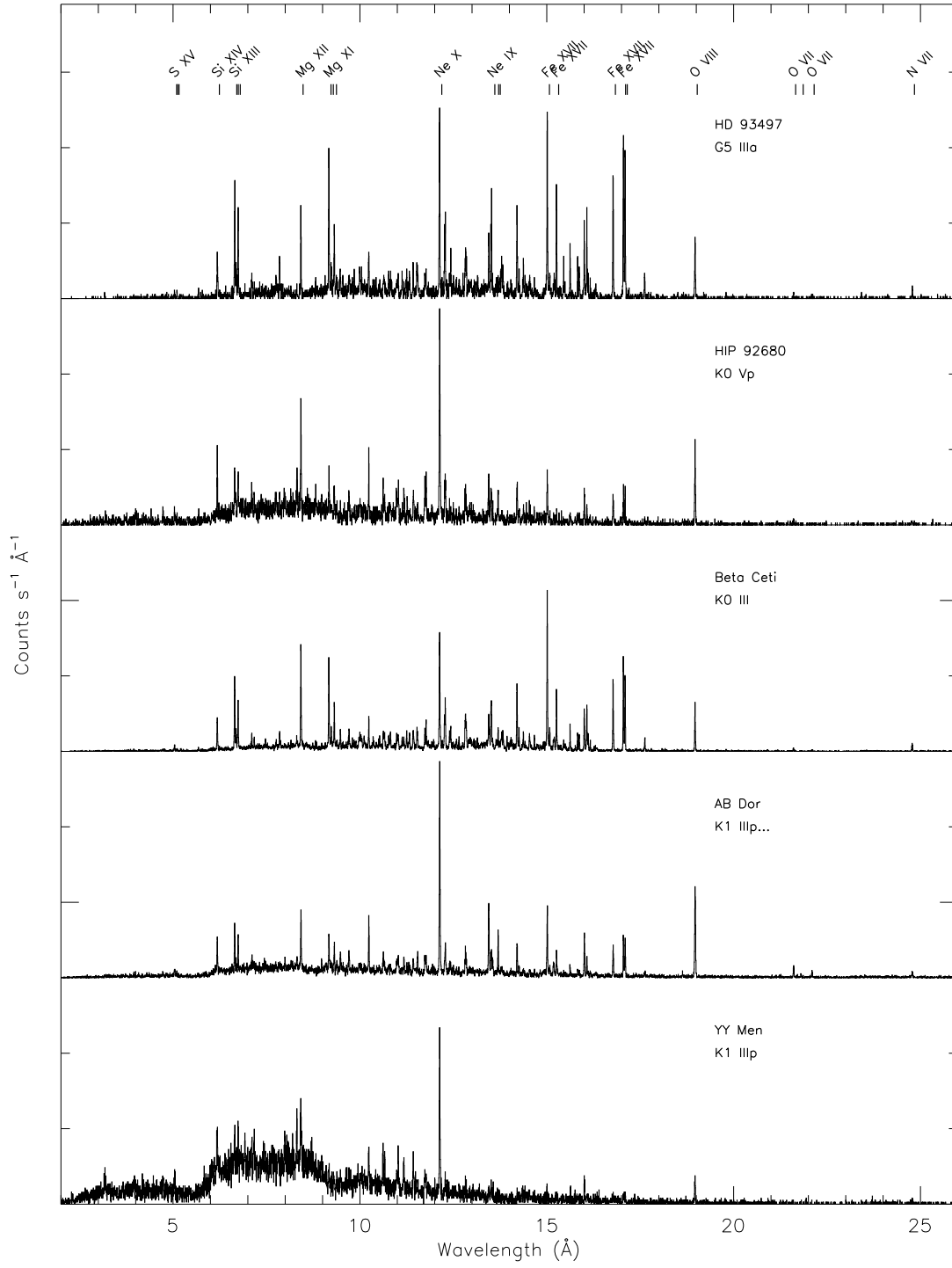


Fig. 8.— As in Figure 2, for normal and rapidly rotating low-mass stars in the atlas.

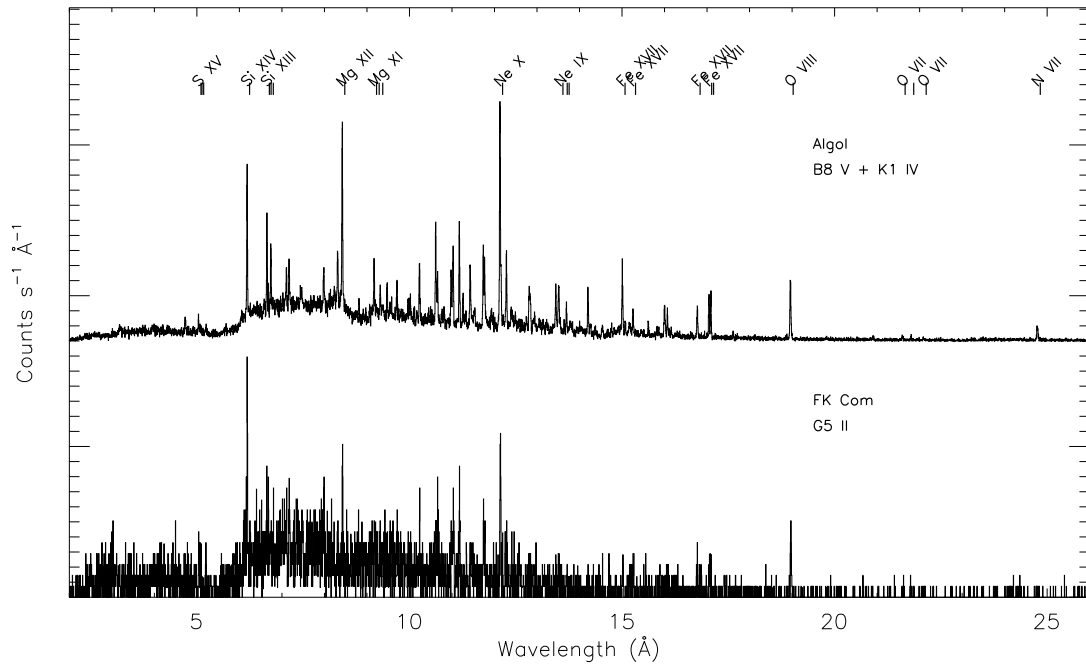


Fig. 9.— As in Figure 2, for two unique stellar systems, Algol (*top*) and FK Com (*bottom*). Algol is a three-star system with a semi-detached B8 V/K1 IV eclipsing binary in orbit with an A V star. The X-ray emission is believed to originate from the K1 star (White et al. 1980). FK Com is an active, variable G-type giant rotating near breakup velocity, possibly a recently coalesced binary (Huenemoerder et al. 1993).

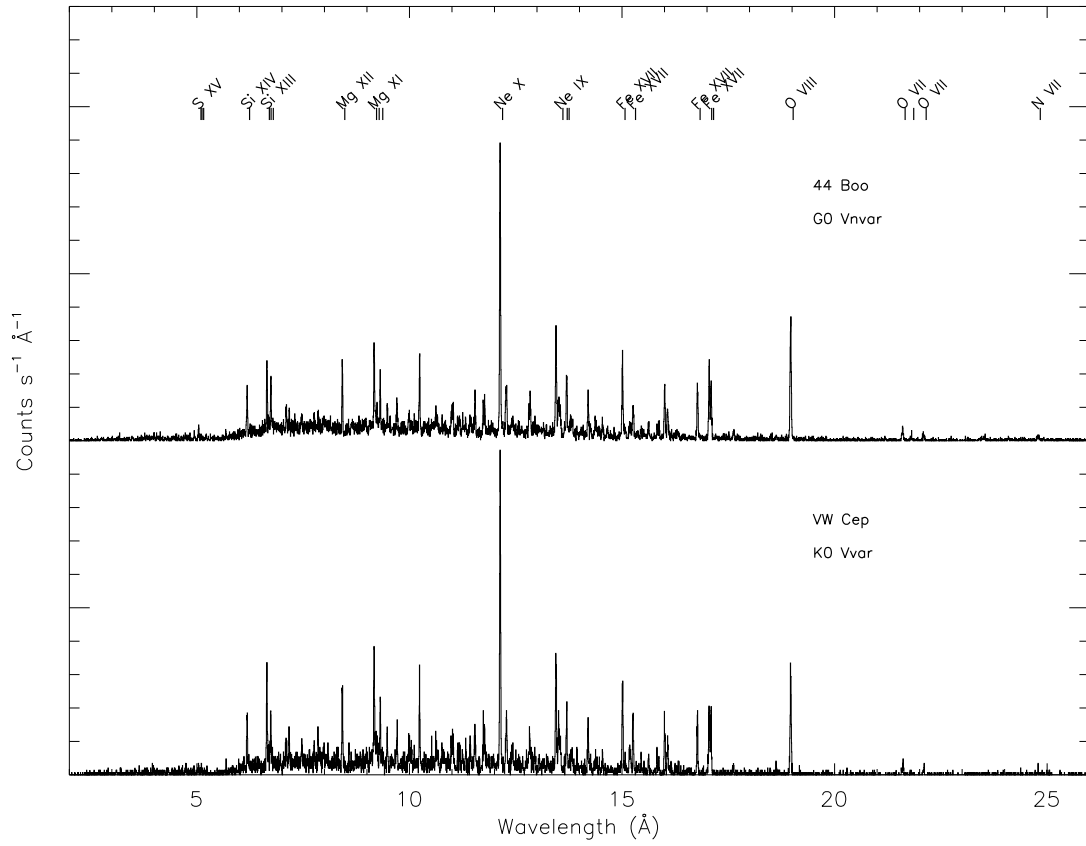
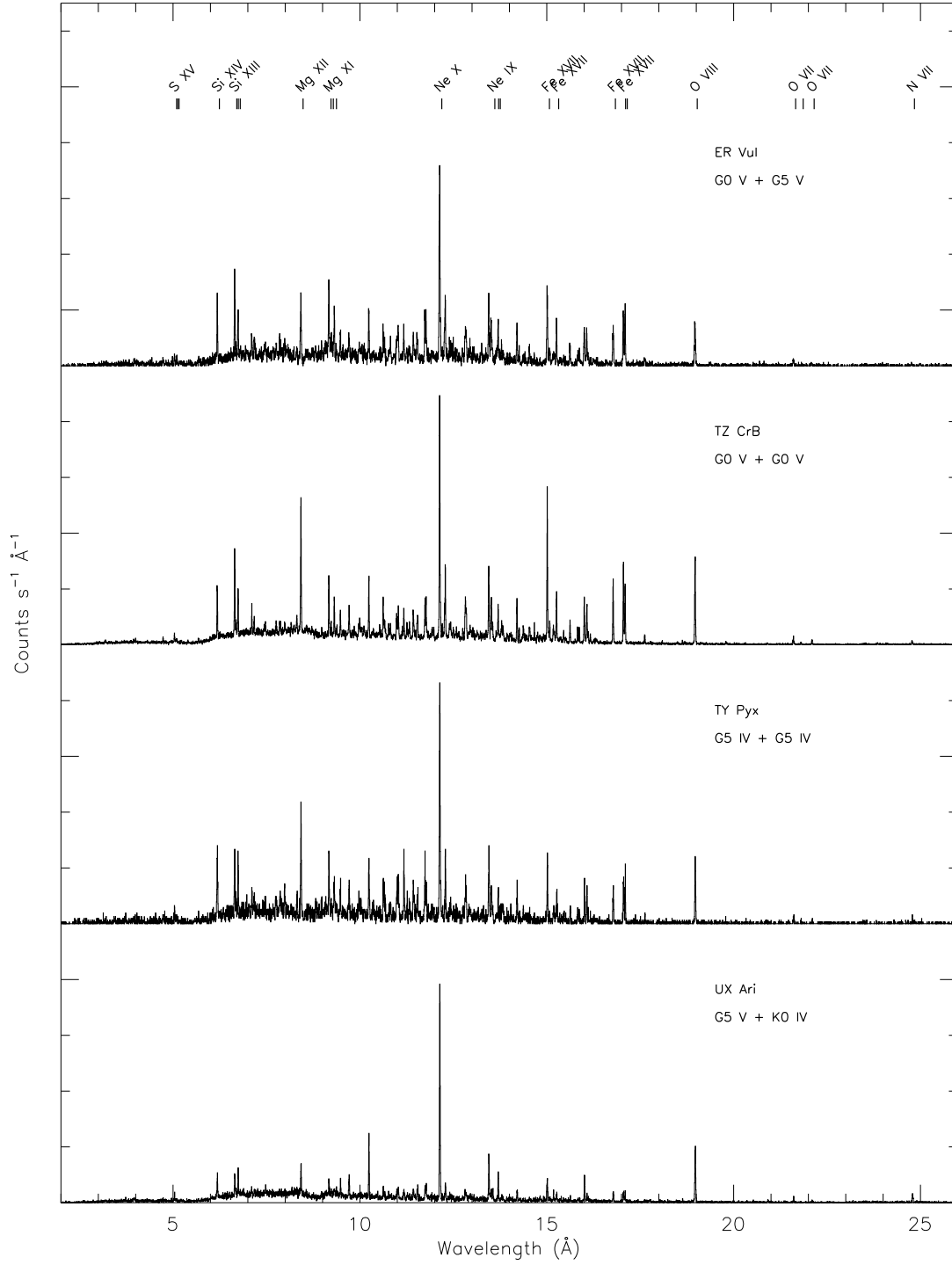


Fig. 10.— As in Figure 2, for two W UMa-type stars, 44 Boo and VW Cep.



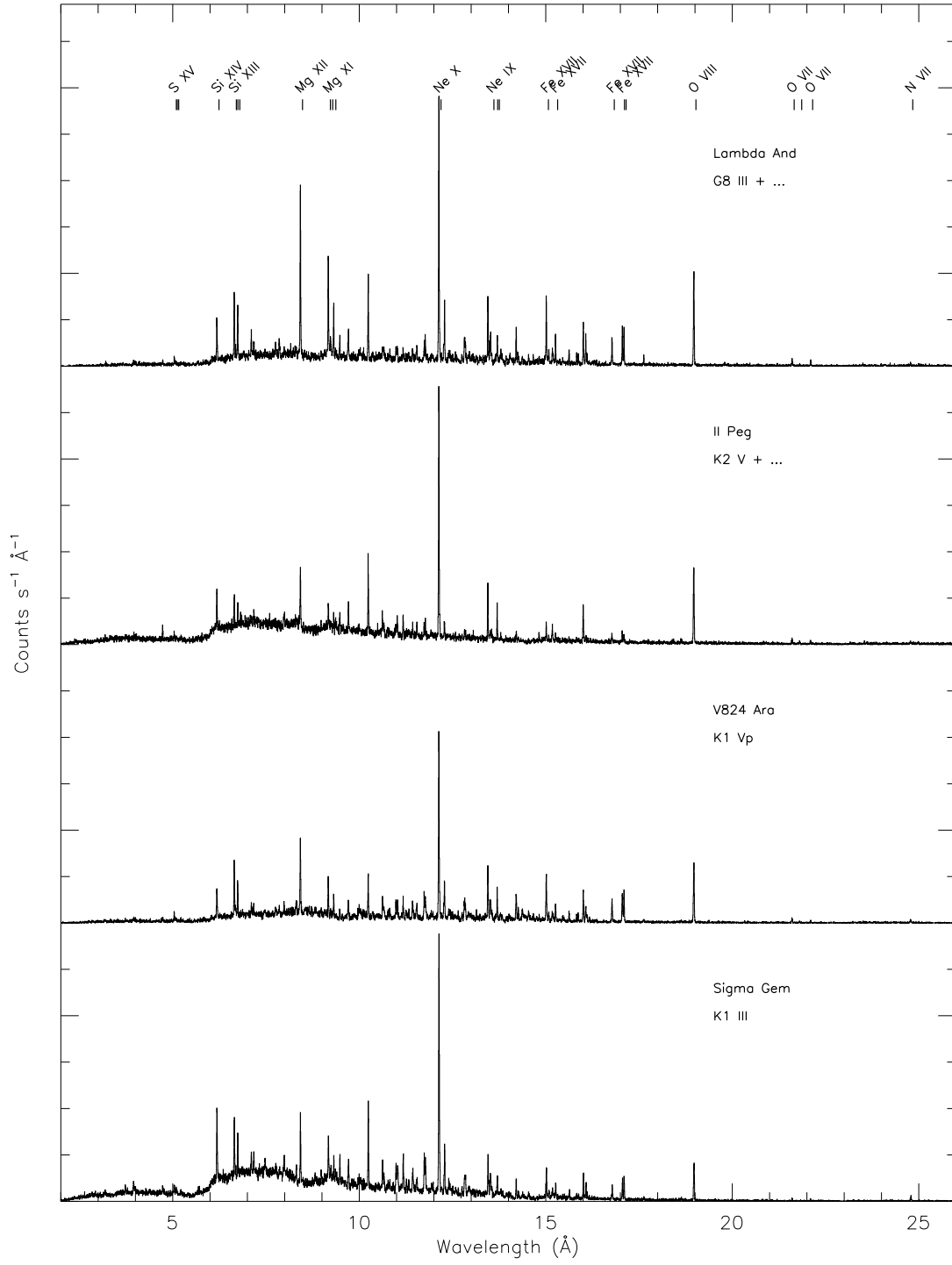
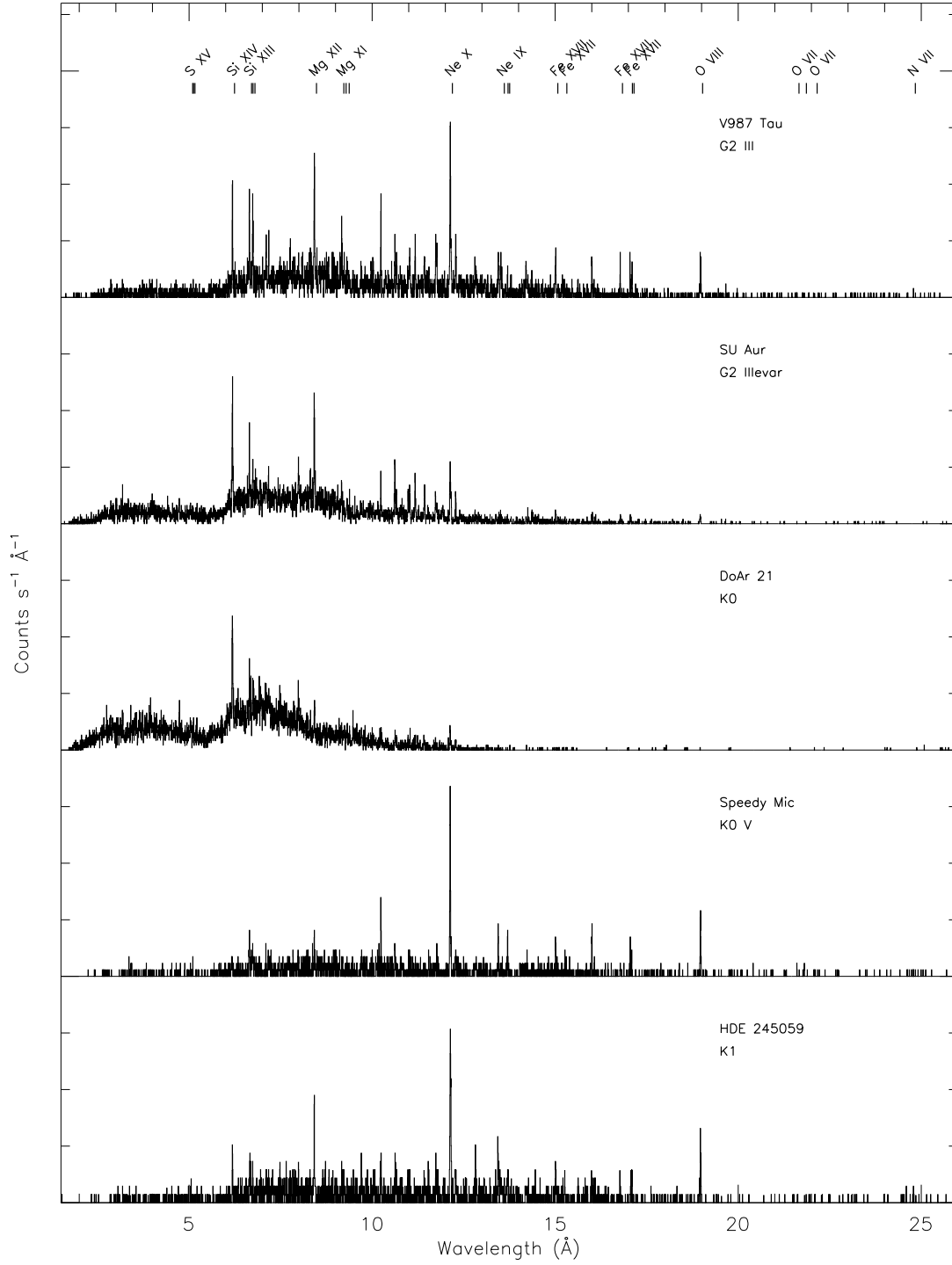


Fig. 11.— As in Figure 2, for RS CVn stars in the atlas.



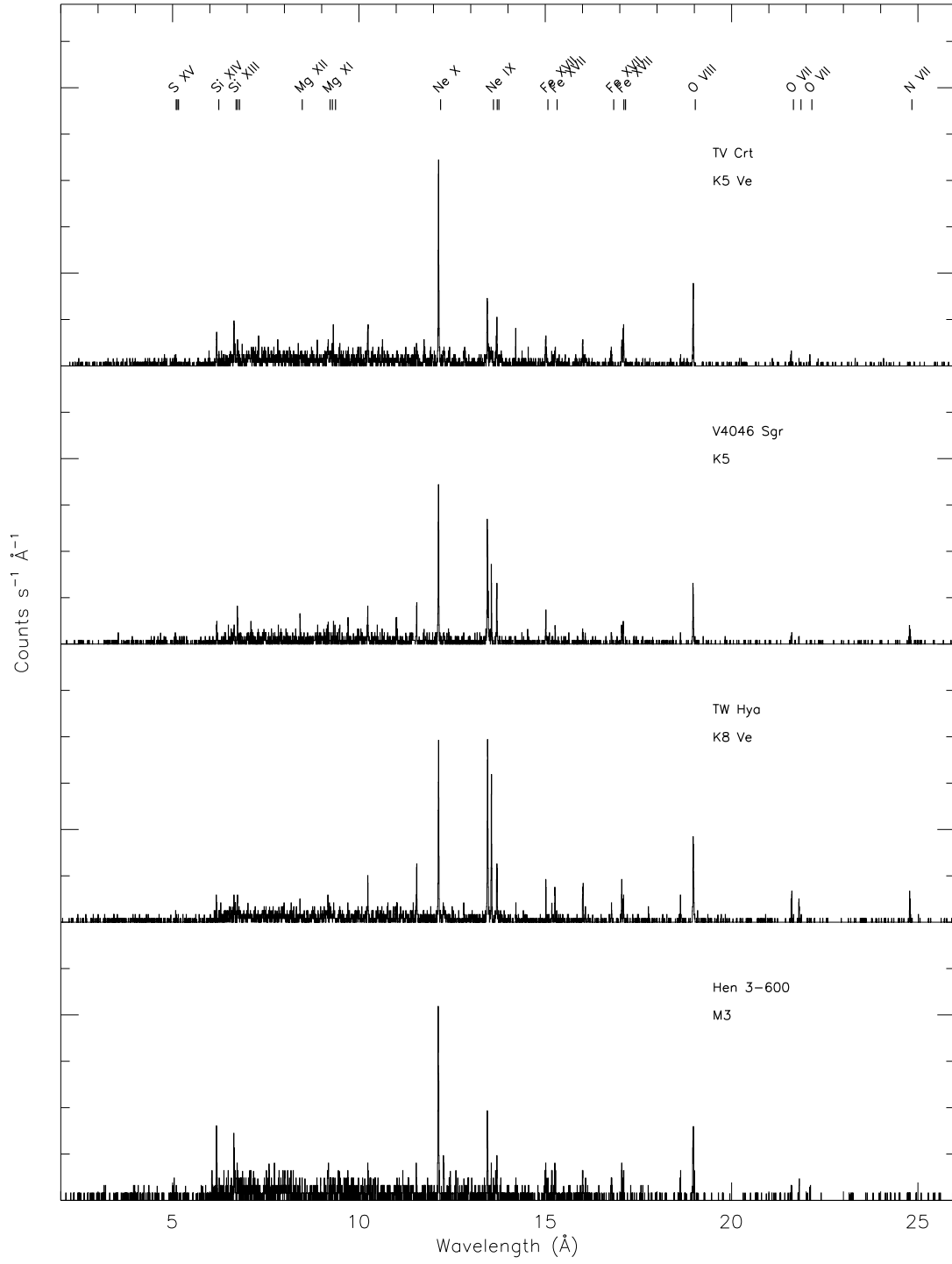


Fig. 12.— As in Figure 2, for T Tauri-type stars in the atlas.

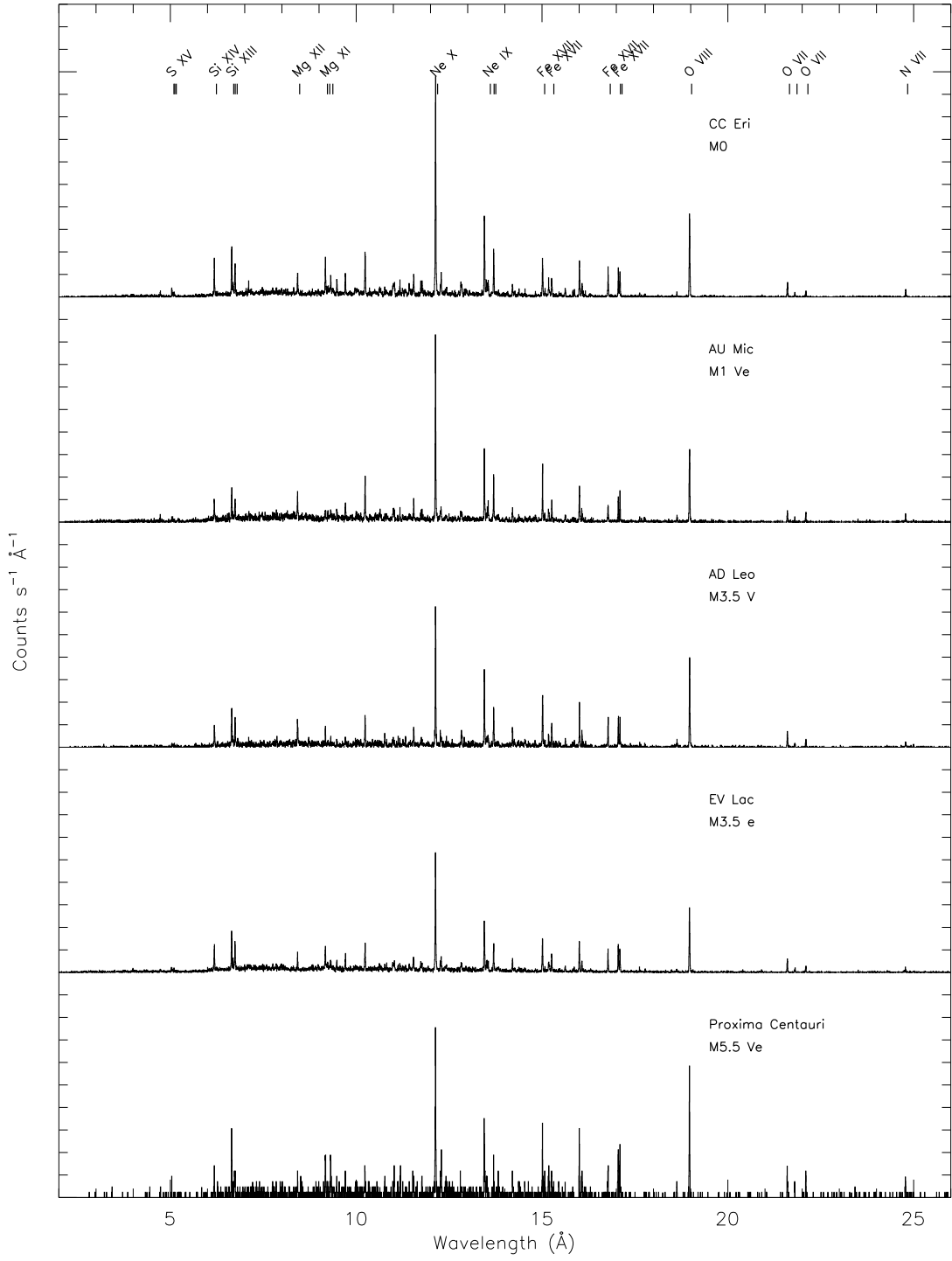


Fig. 13.— As in Figure 2, for active and flaring low-mass stars.

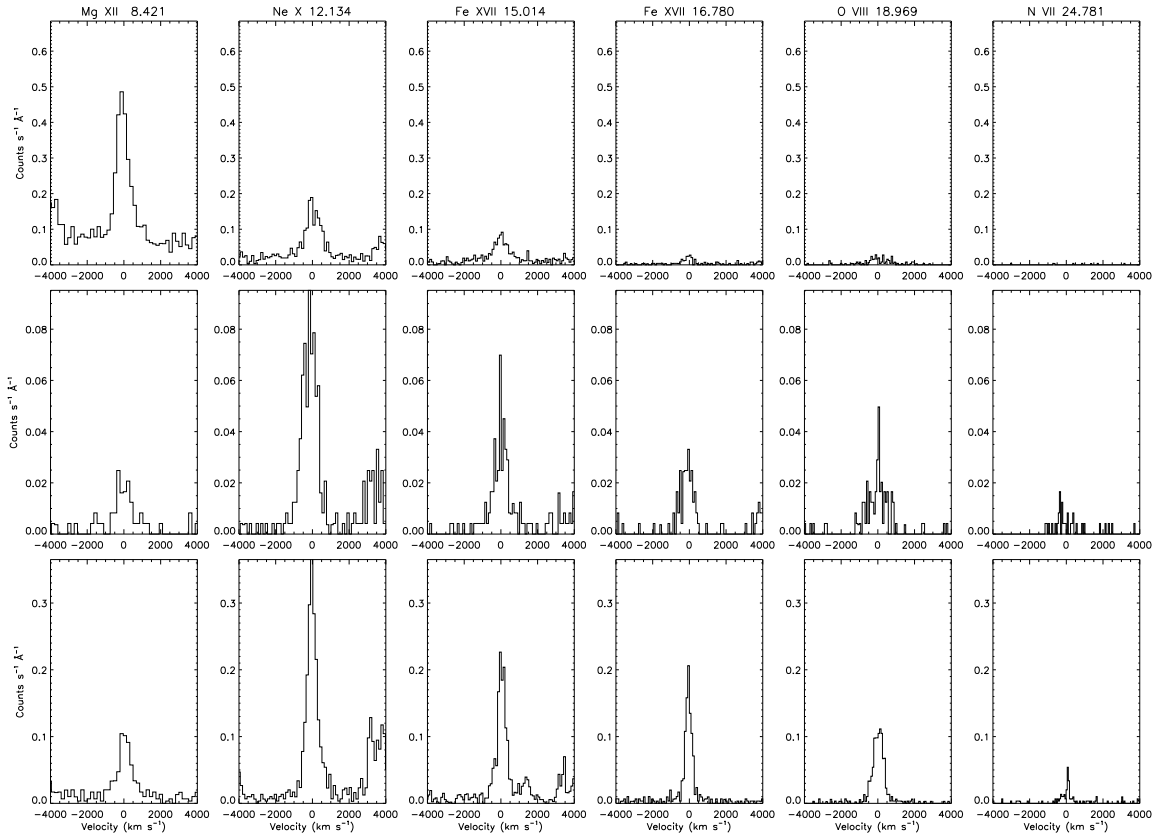


Fig. 14.— Line profiles of selected lines in MEG spectra. Columns from left to right: Mg XII λ 8.421, Ne X λ 12.134, Fe XVII λ 15.014, Fe XVII λ 16.780, O VIII λ 18.969, and N VII λ 24.781. Descending from top row: θ^1 Ori C, ζ Oph, and τ Sco.

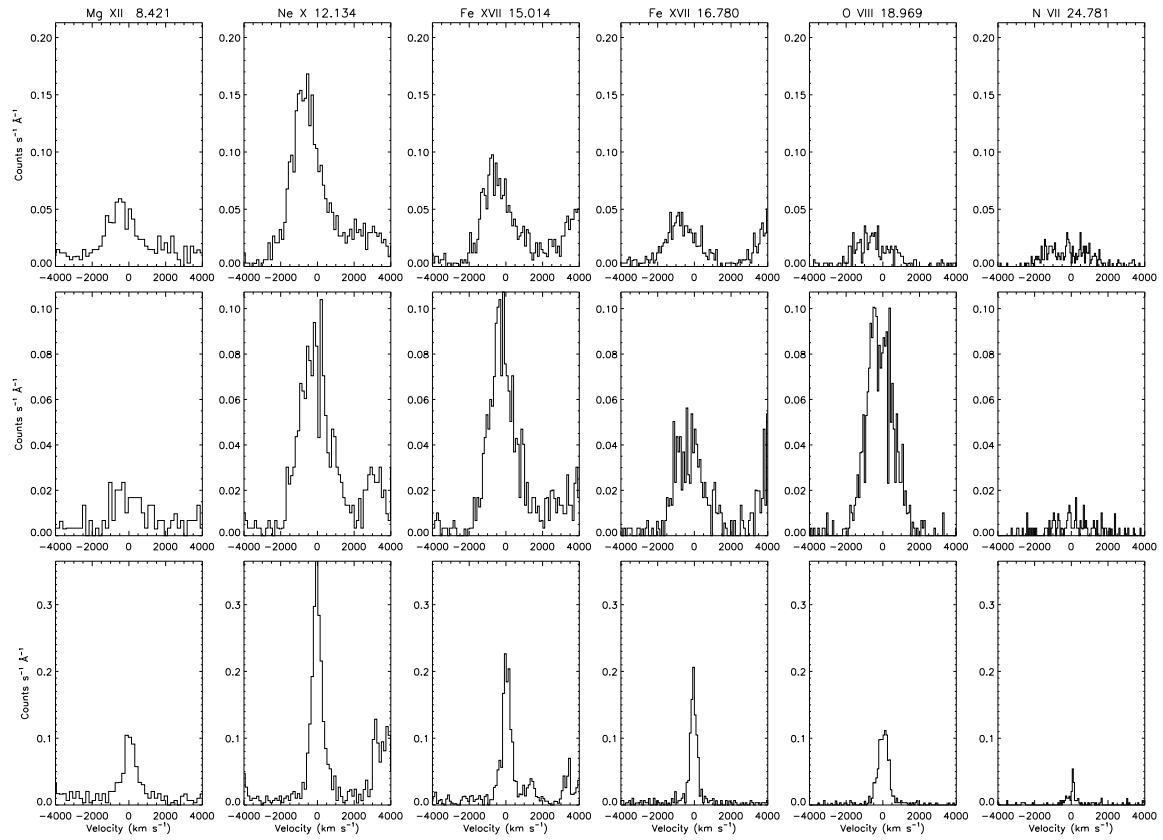


Fig. 15.— As in Figure 14, for the sources, descending from top row: ζ Pup, ζ Ori, ι Ori.

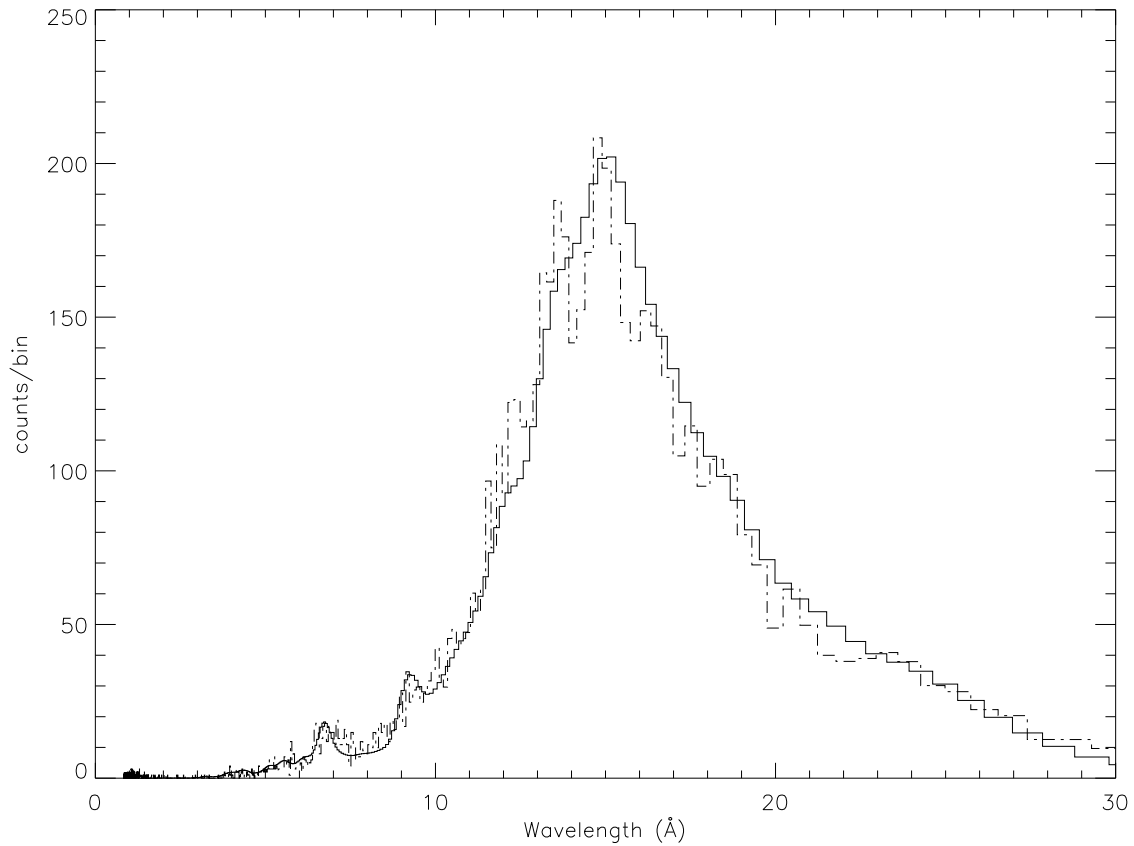


Fig. 16.— Predicted (solid line) and actual (dashed line) 0^{th} -order spectra for ξ Per (ObsID 4512). Bin sizes vary across the wavelength range, and are determined by the PHA binning in the RMF. For this observation, the predicted and observed spectra agreed to a χ^2 value of 381.7, with 340 non-zero bins. A 10% calibration error in the effective area was included in the observed spectrum for the χ^2 calculation.

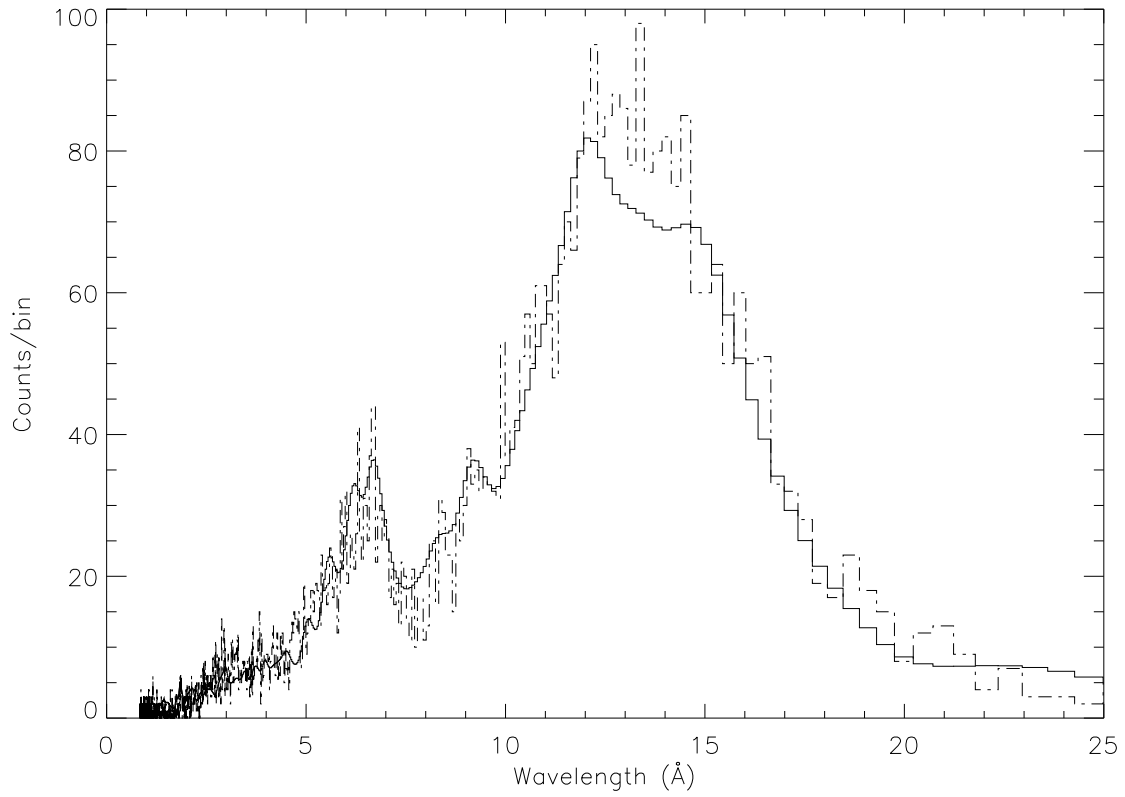


Fig. 17.— Predicted (solid line) and actual (dashed line) 0^{th} -order spectra for HD 93250, produced by combining ObsIDs 5399, 5400, 7189, 7341, and 7342. PHA binning is determined as in Figure 16. For this observation, the predicted and observed spectra agreed to a χ^2 value of 865.5, with 630 non-zero bins. A 10% calibration error in the effective area was included in the observed spectrum for the χ^2 calculation.

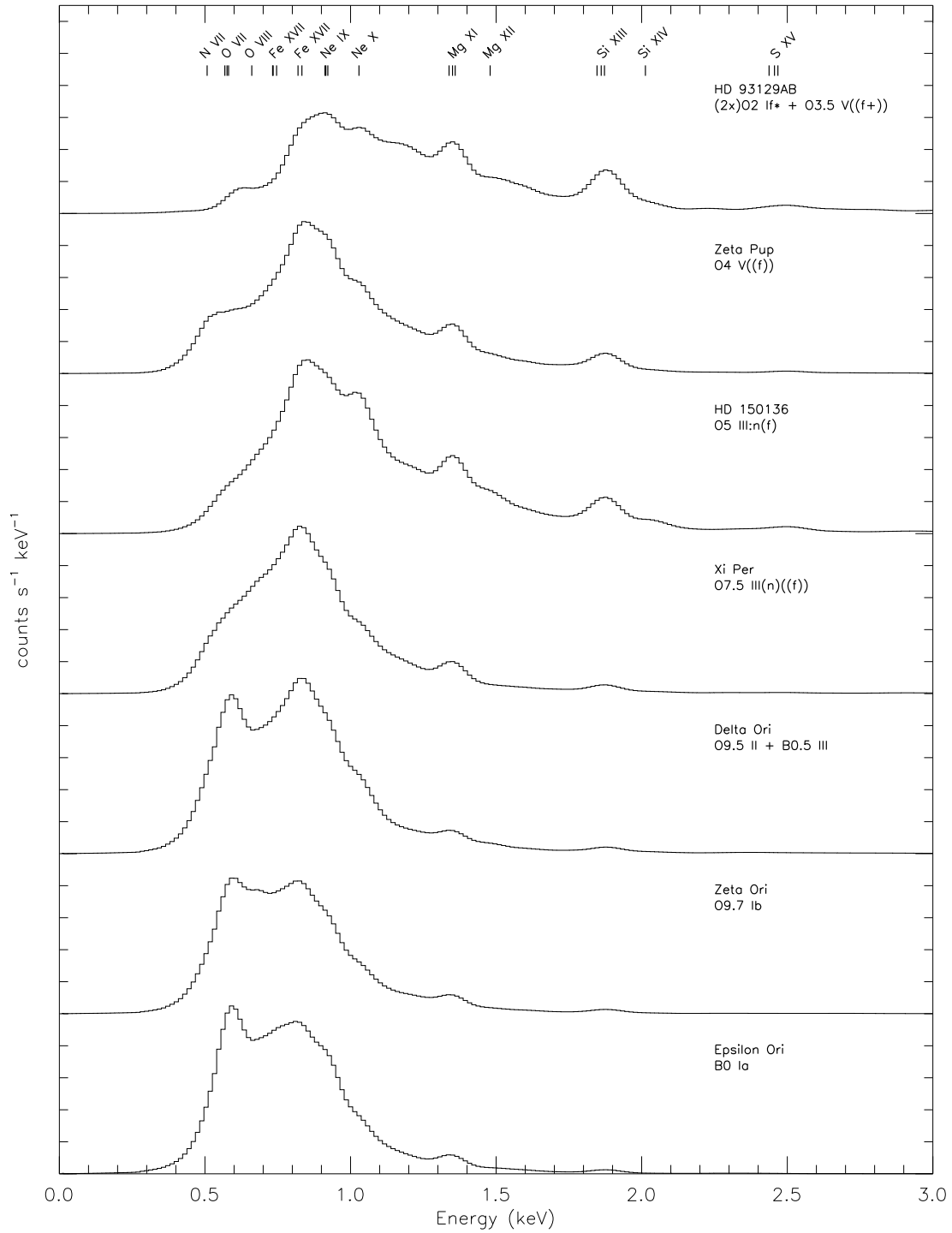


Fig. 18.— The predicted low-resolution ACIS-S spectra ([counts/s/keV]) of OB supergiants and giants, ordered by spectral class. The spectrum of each source is offset for clarity. The diminishing strength of S, Si, Mg, and Ne lines and the growth of O lines in later spectral classes is still evident in low-resolution.

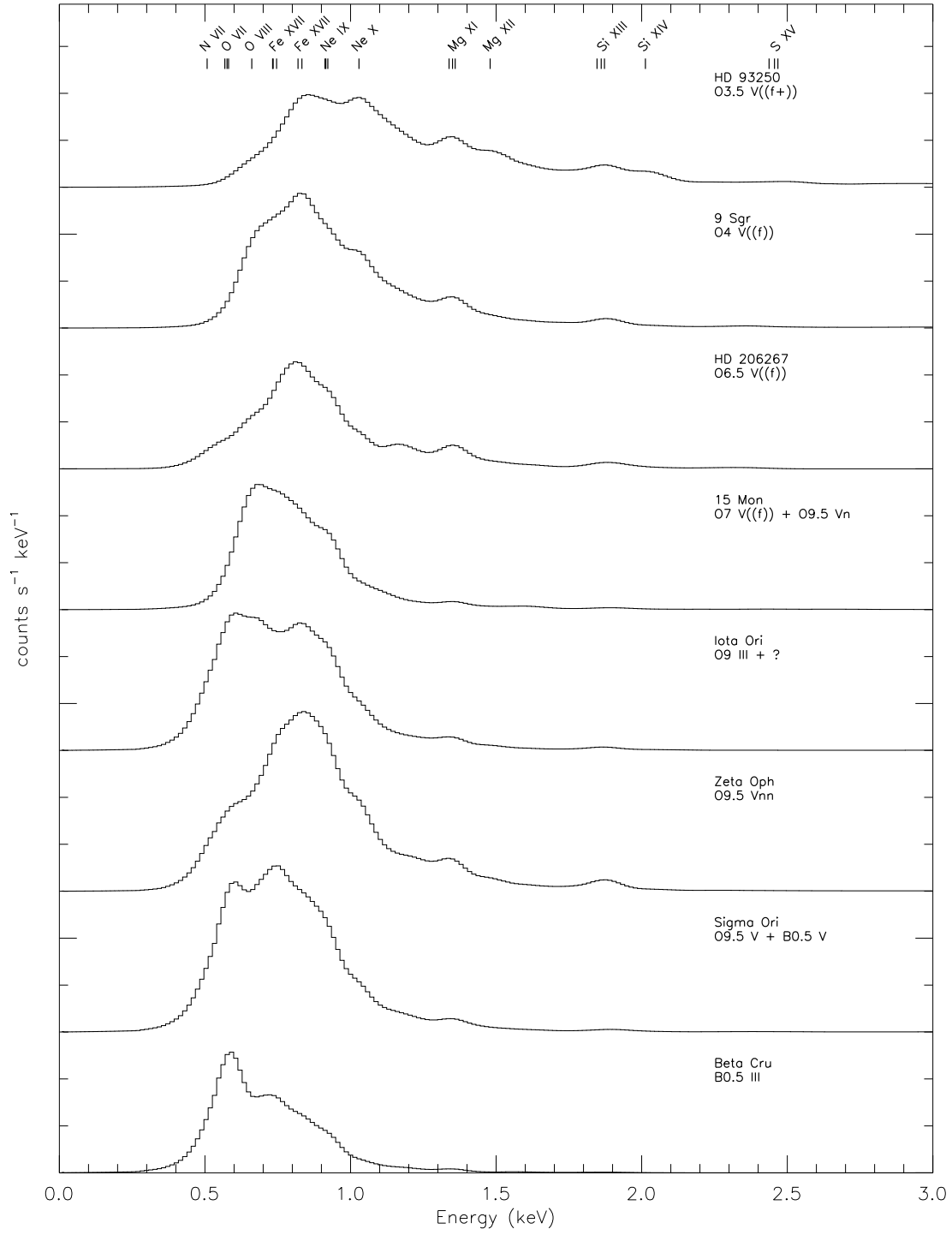


Fig. 19.— As in Figure 18, for OB giants, sub-giants and dwarfs, ordered by spectral class.

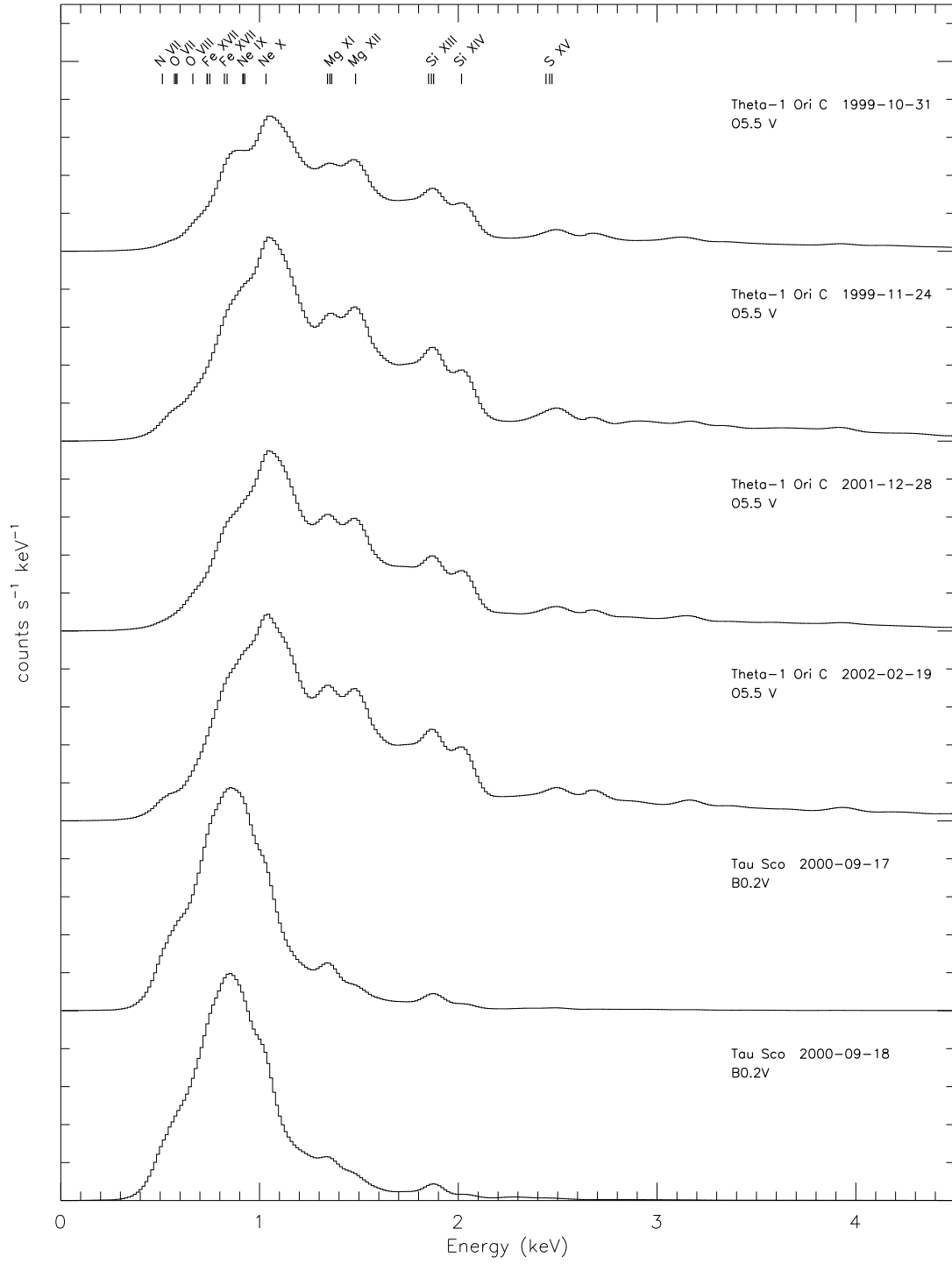


Fig. 20.— As in Figure 18, for the two OB stars, θ^1 Ori C and τ Sco, thought to have strong magnetic fields responsible for their X-ray emissions.

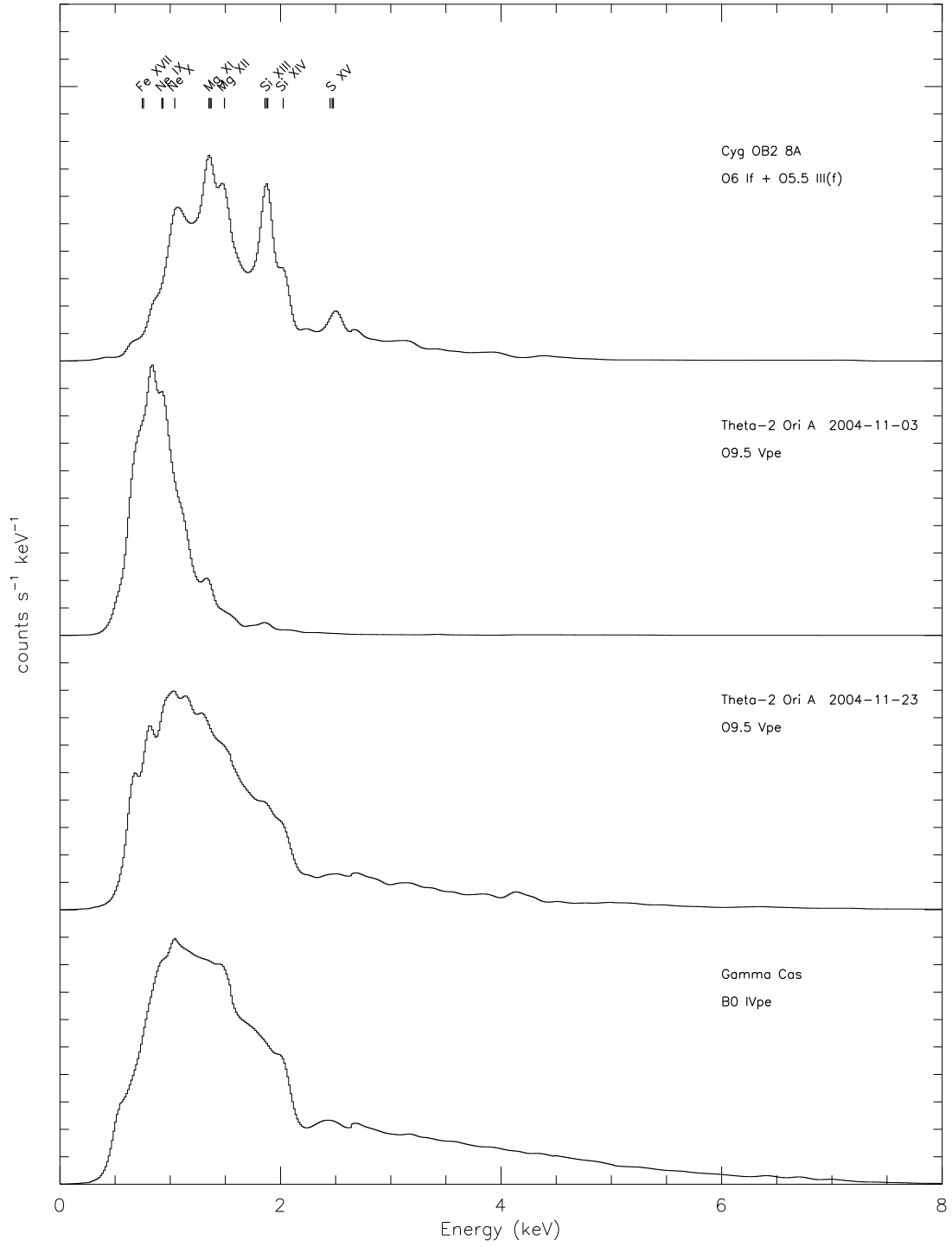


Fig. 21.— As in Figure 18, for the three peculiar OB stars: Cyg OB2 8A, θ^2 Ori A, and γ Cas.

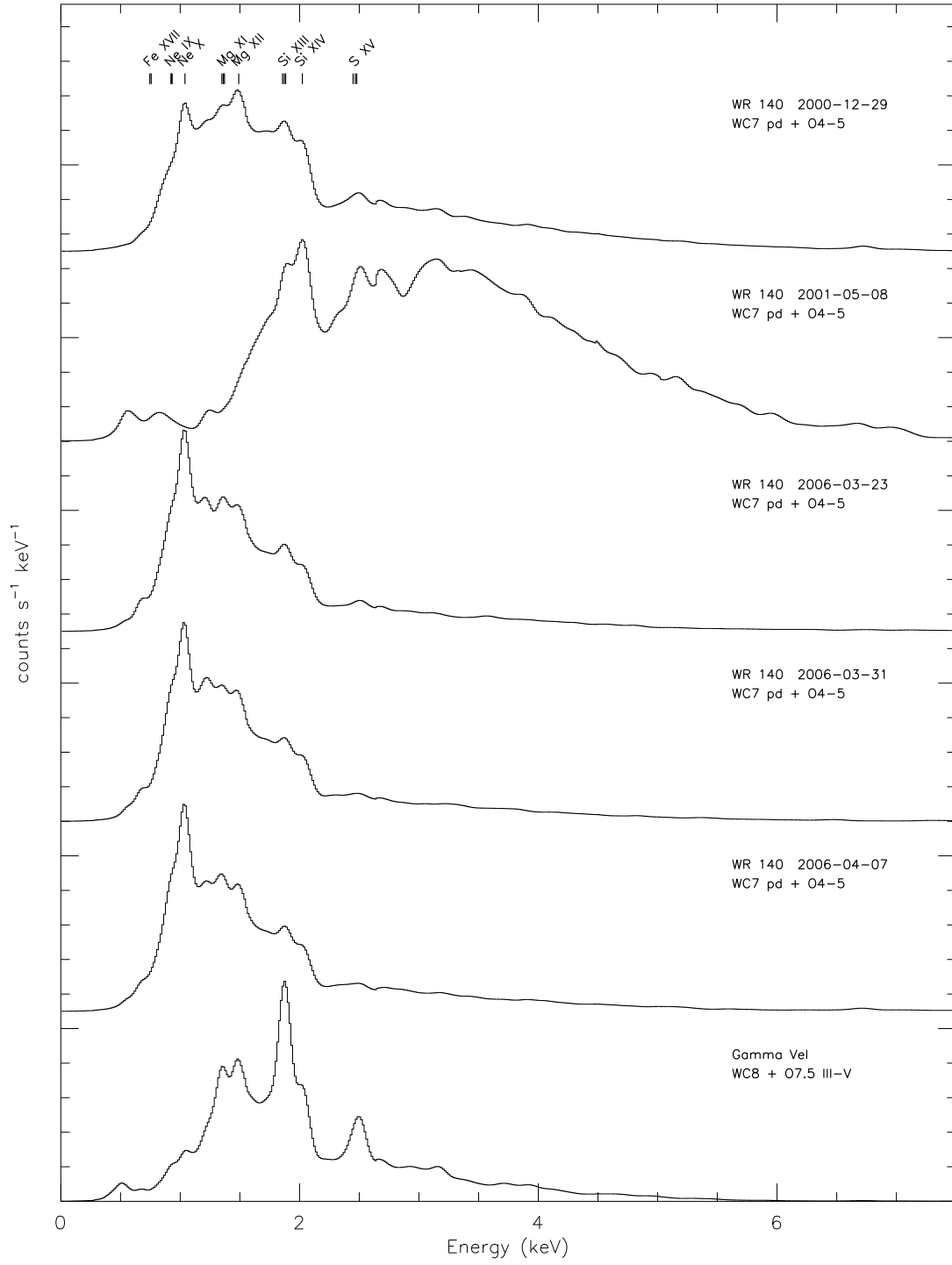


Fig. 22.— As in Figure 18, for the two Wolf-Rayet stars observed with HETG.

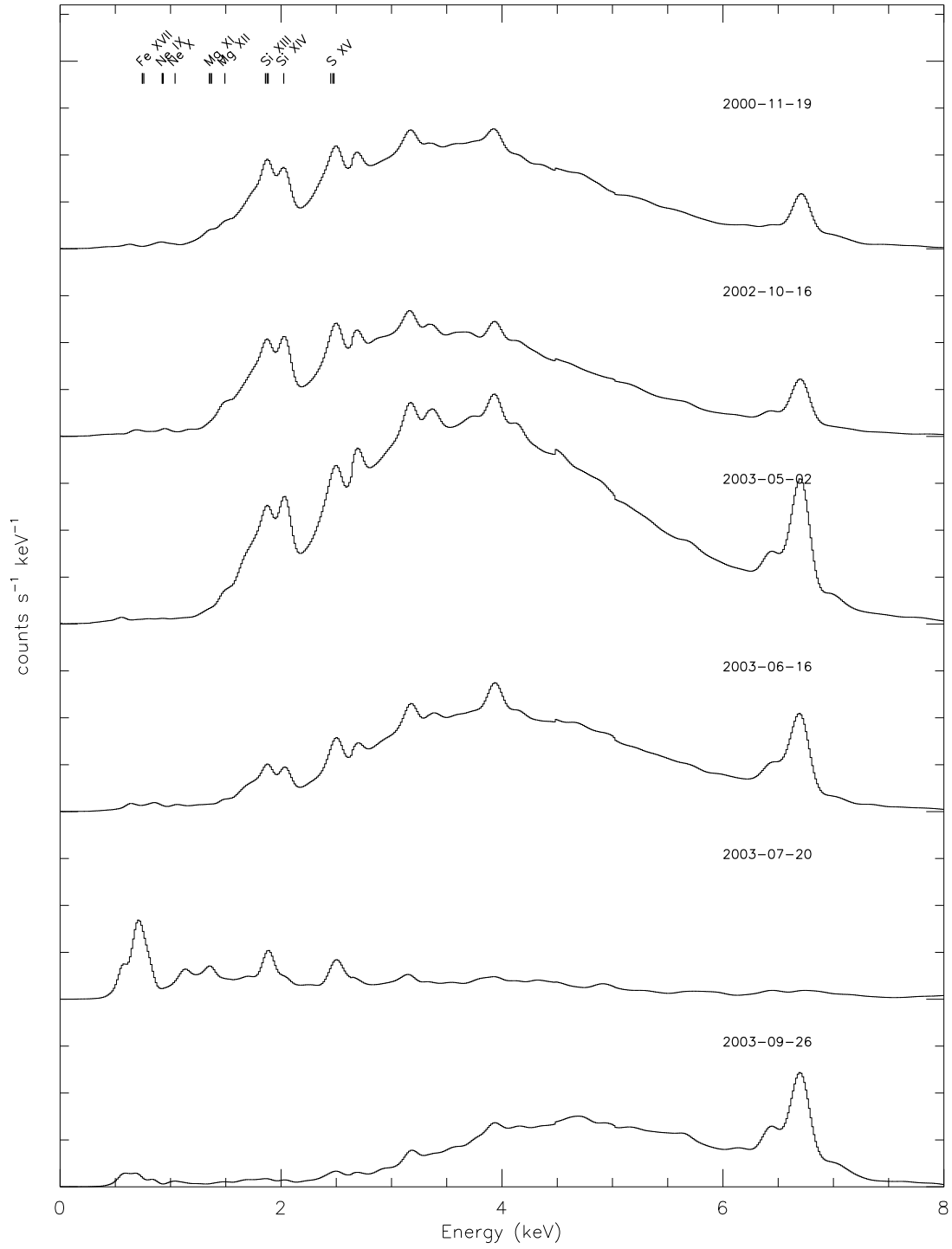
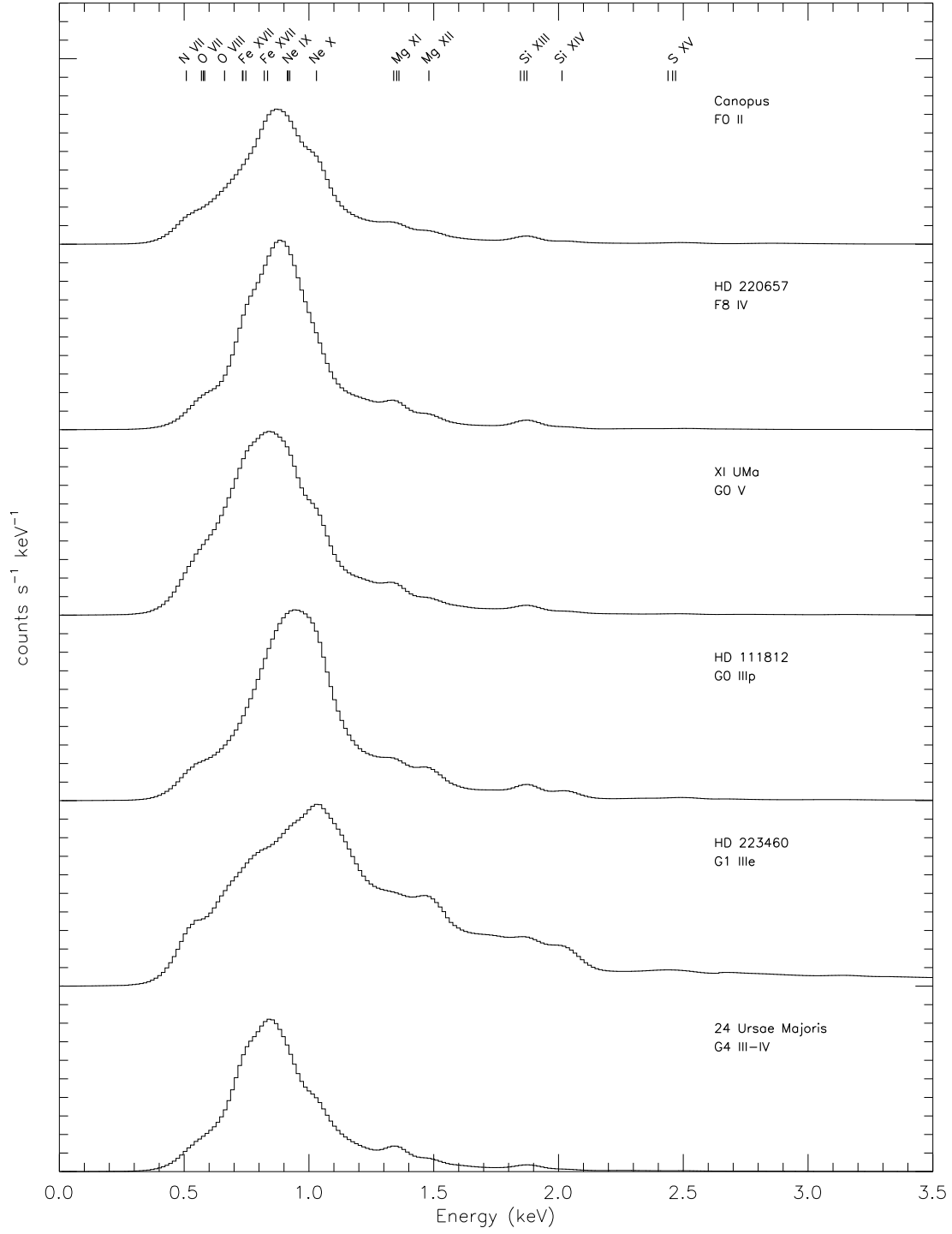


Fig. 23.— As in Figure 18, for the six HETG observations of Eta Carinae. η Carinae underwent an X-ray eclipse in mid-2003: the 2003-05-02 observation was made close to X-ray maximum, and the 2003-07-02 observation was taken near X-ray minimum (Corcoran et al. 2005).



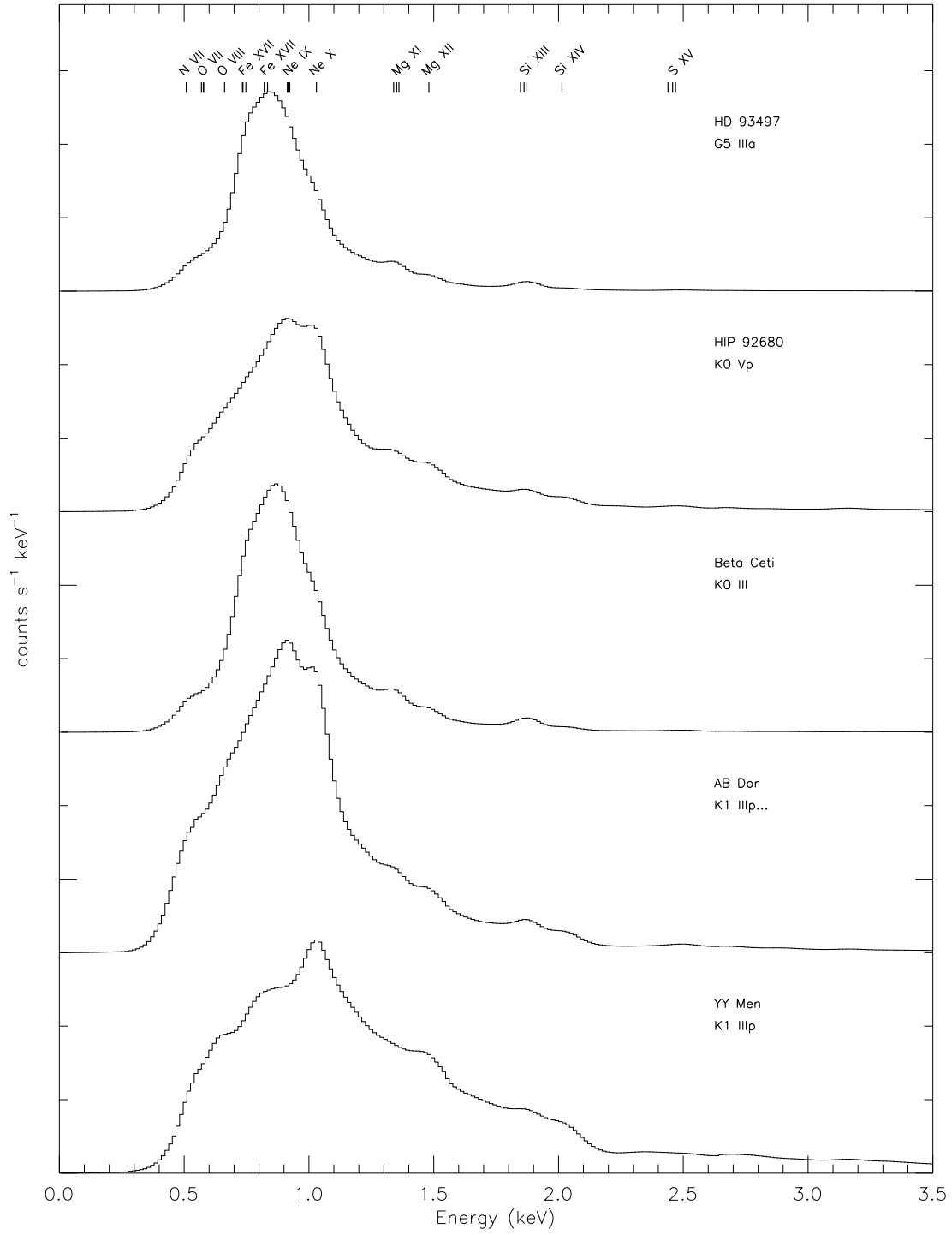


Fig. 24.— As in Figure 18, for normal low-mass stars. Capella is not included here but is featured in a separate montage available on the X-Atlas website.

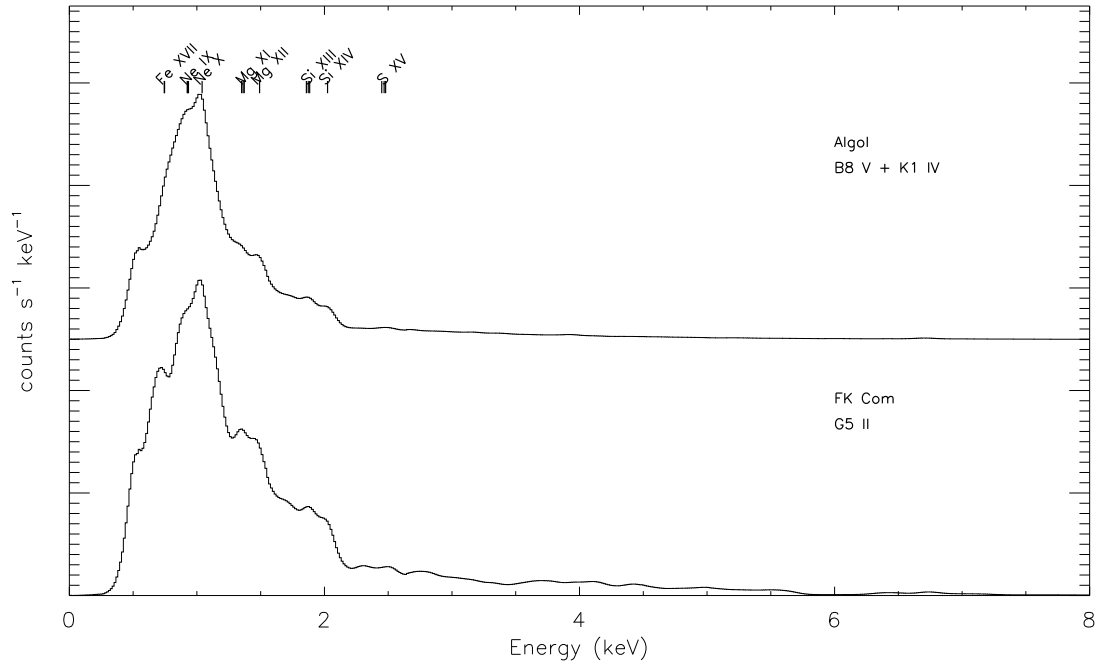


Fig. 25.— As in Figure 18, for two unique systems, Algol and FK Com.

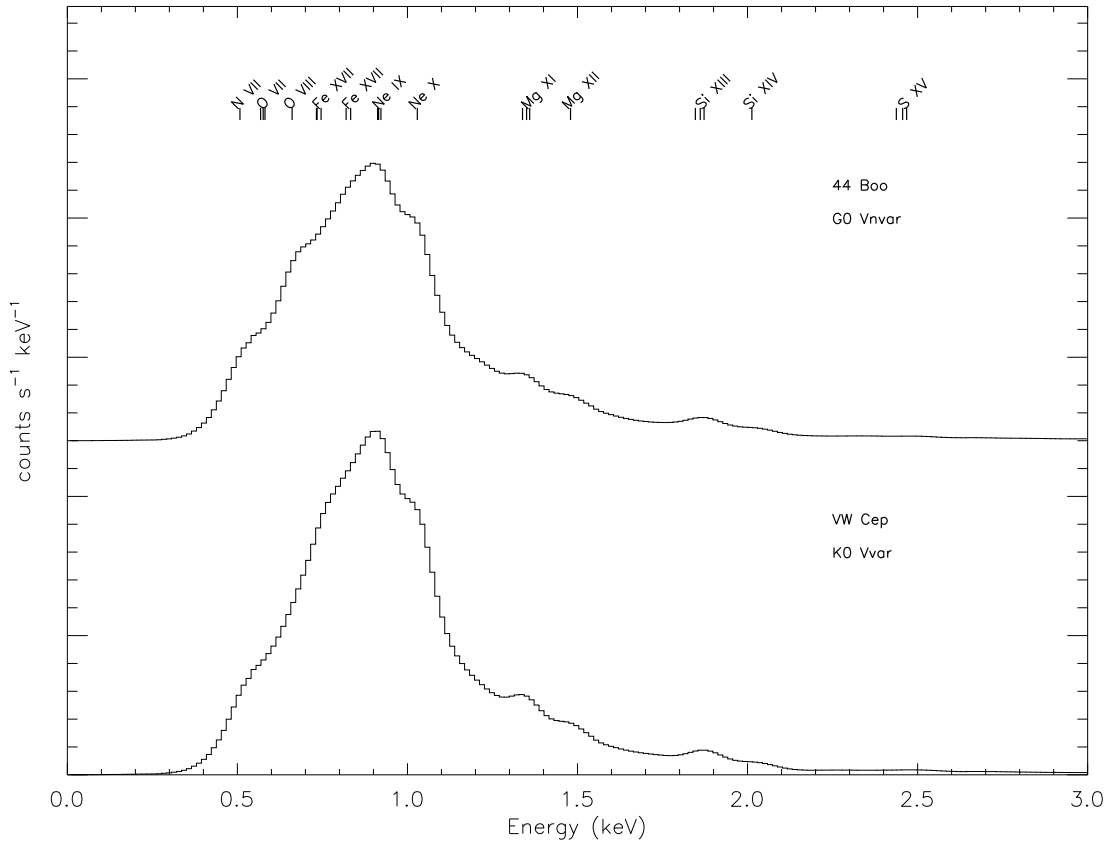
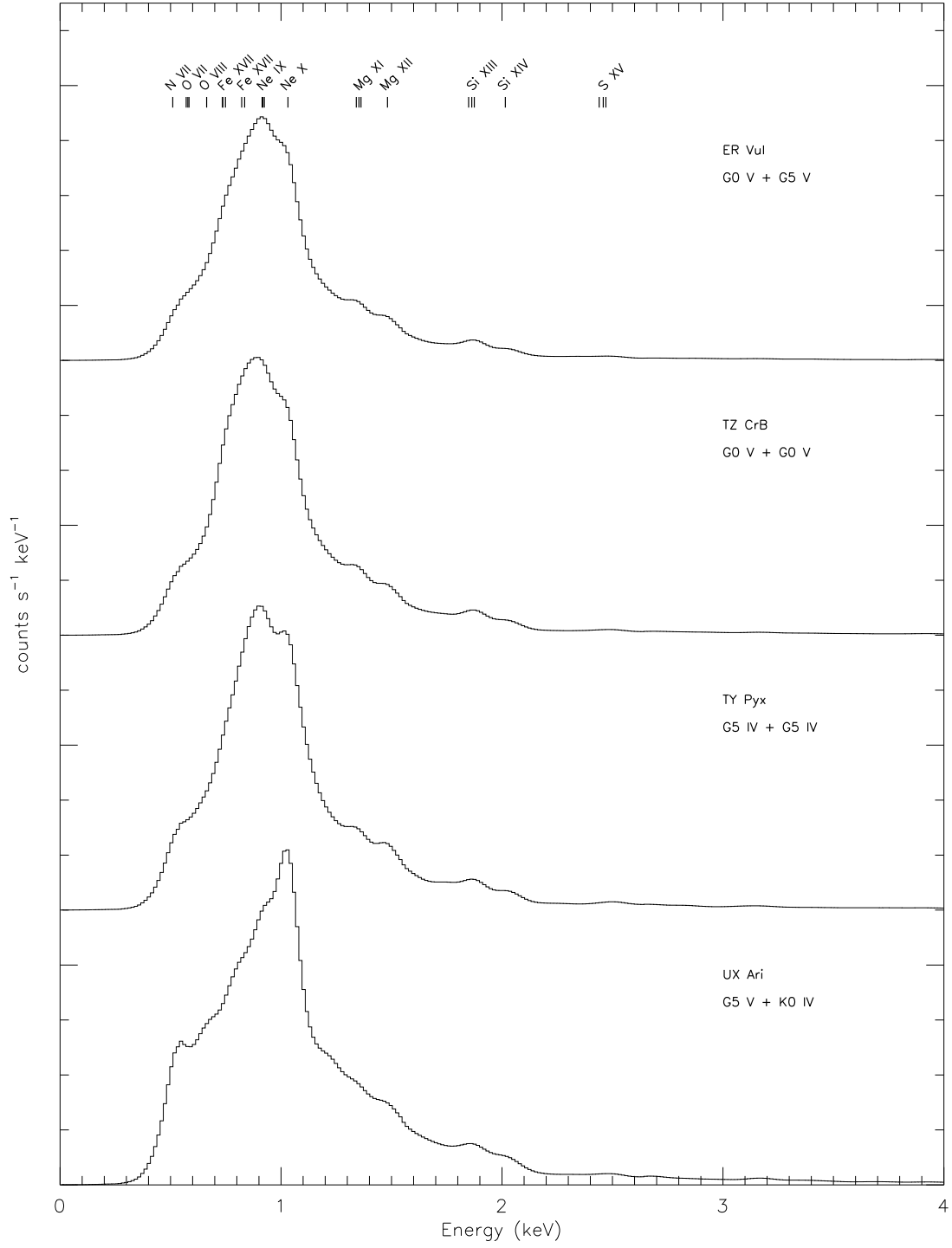


Fig. 26.— As in Figure 18, for W UMa-type variables in the atlas.



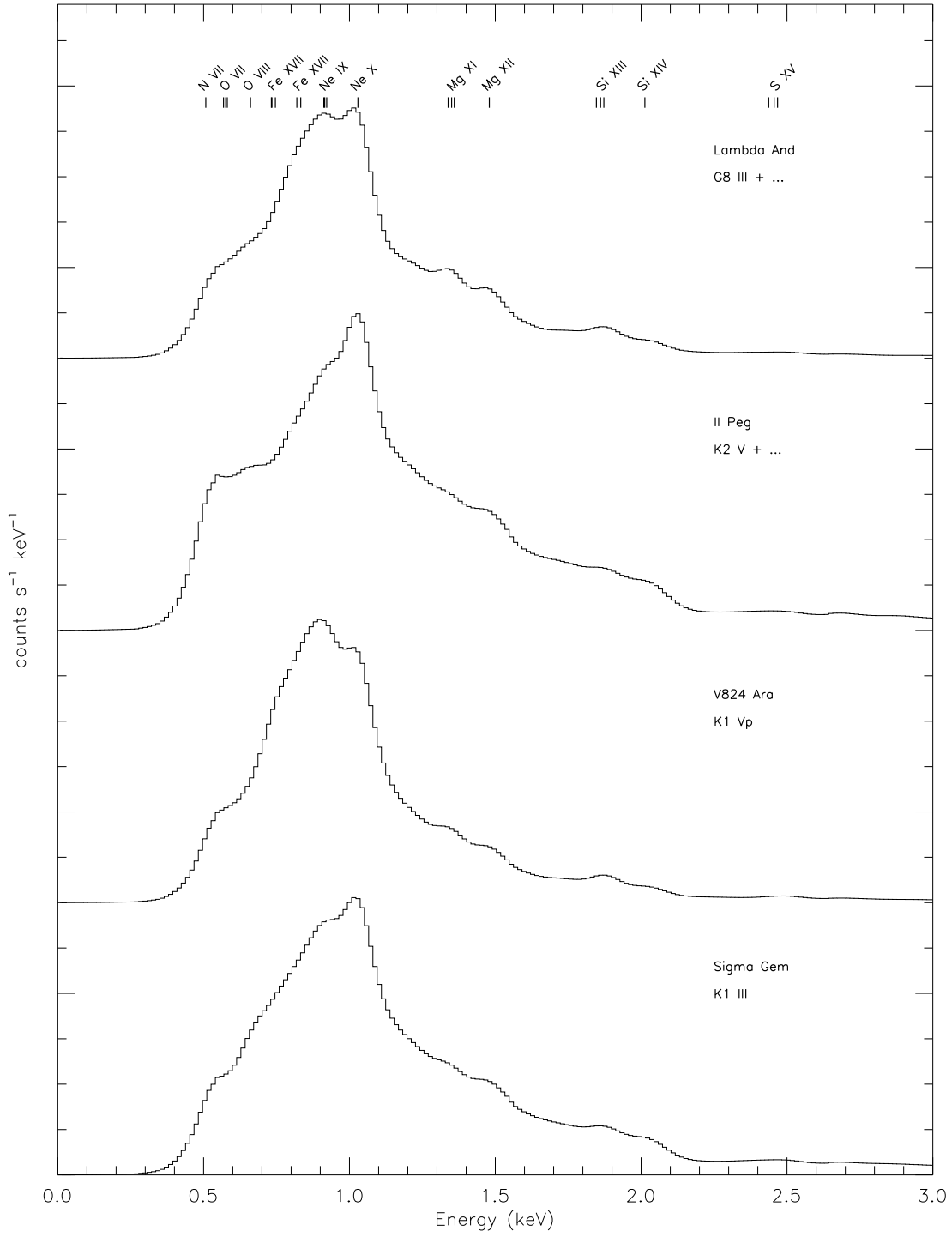
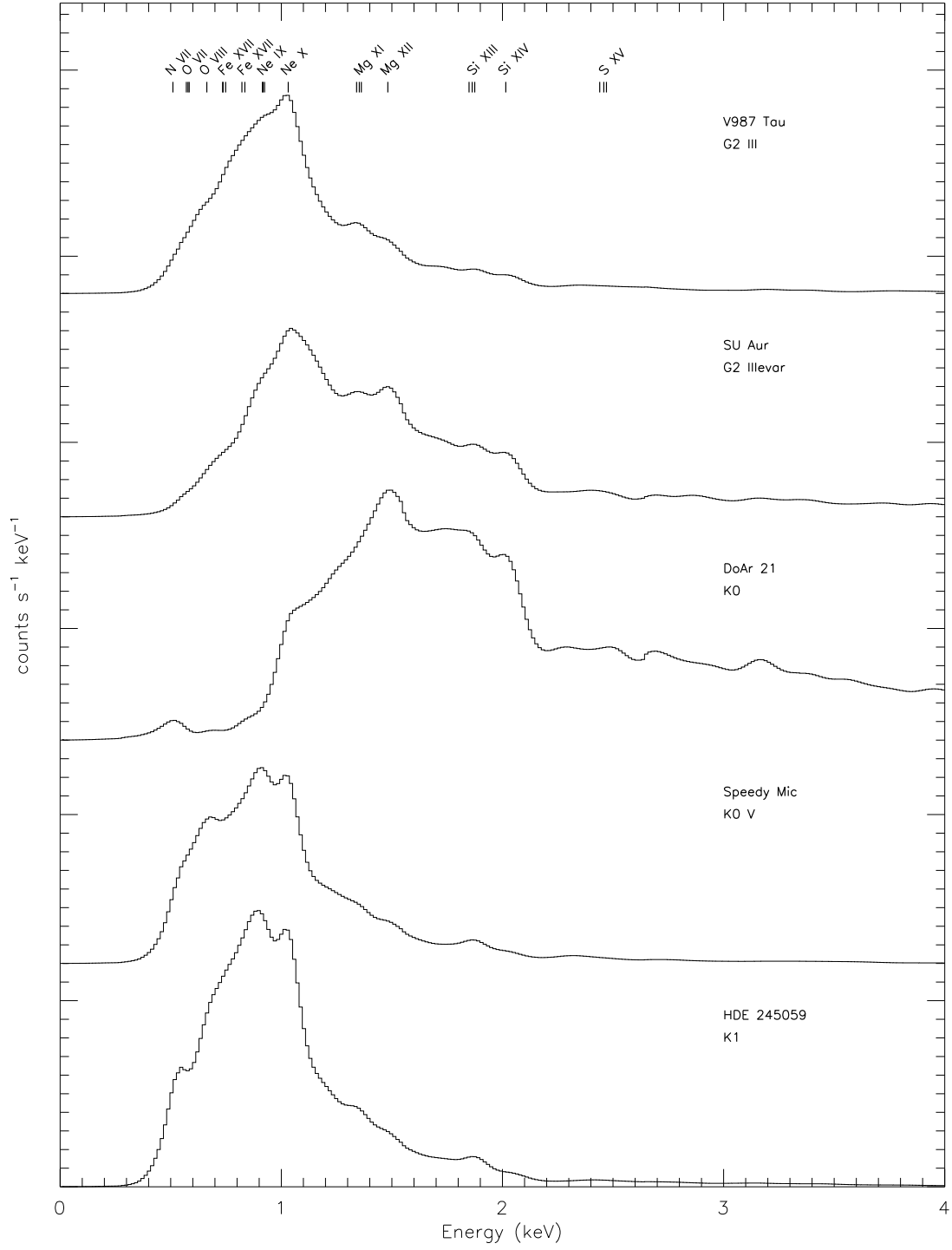


Fig. 27.— As in Figure 18, for eight RS CVn stars. AR Lac and IM Peg are not included here but are featured in separate montages on the X-Atlas website.



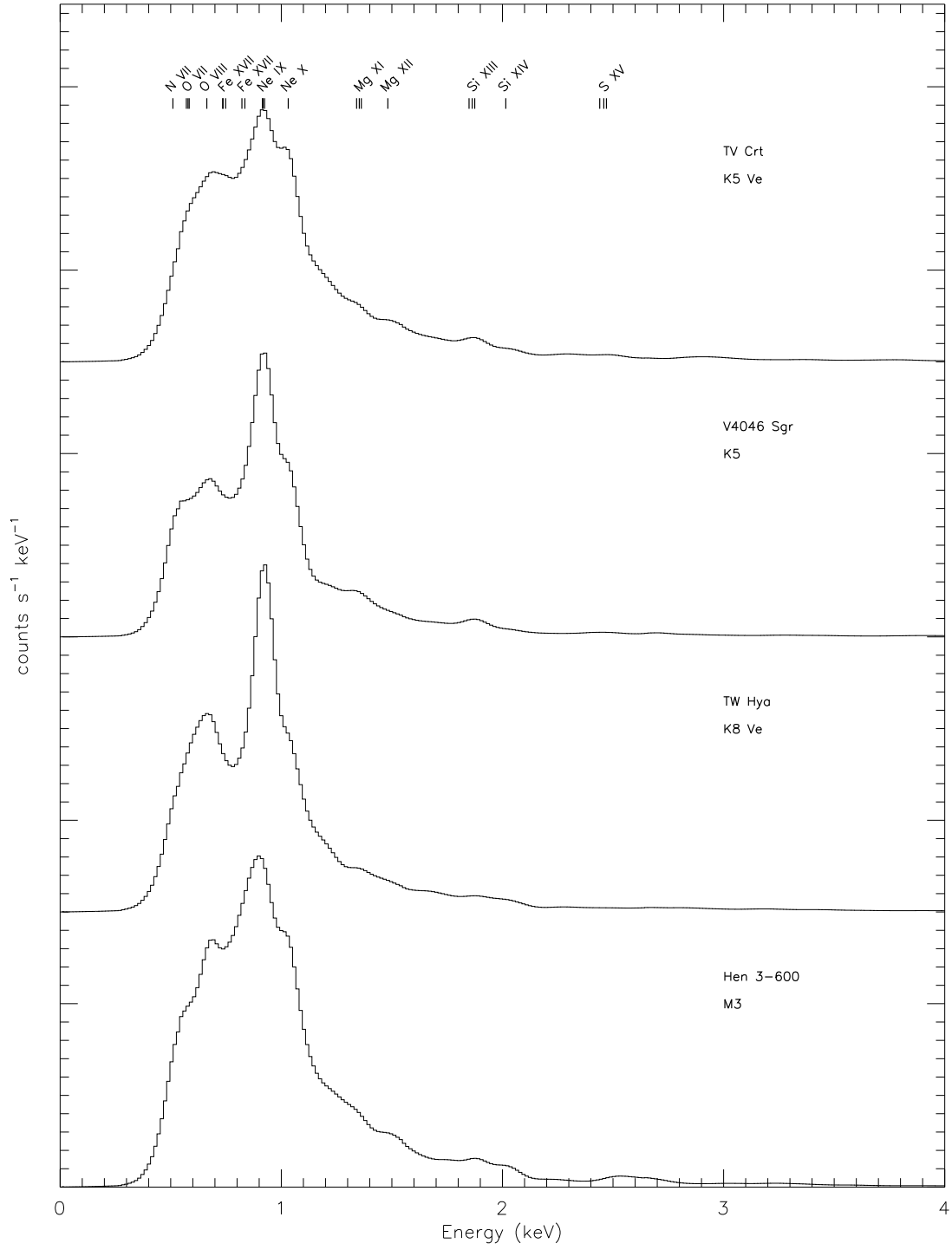


Fig. 28.— As in Figure 18, for nine T Tauri stars.

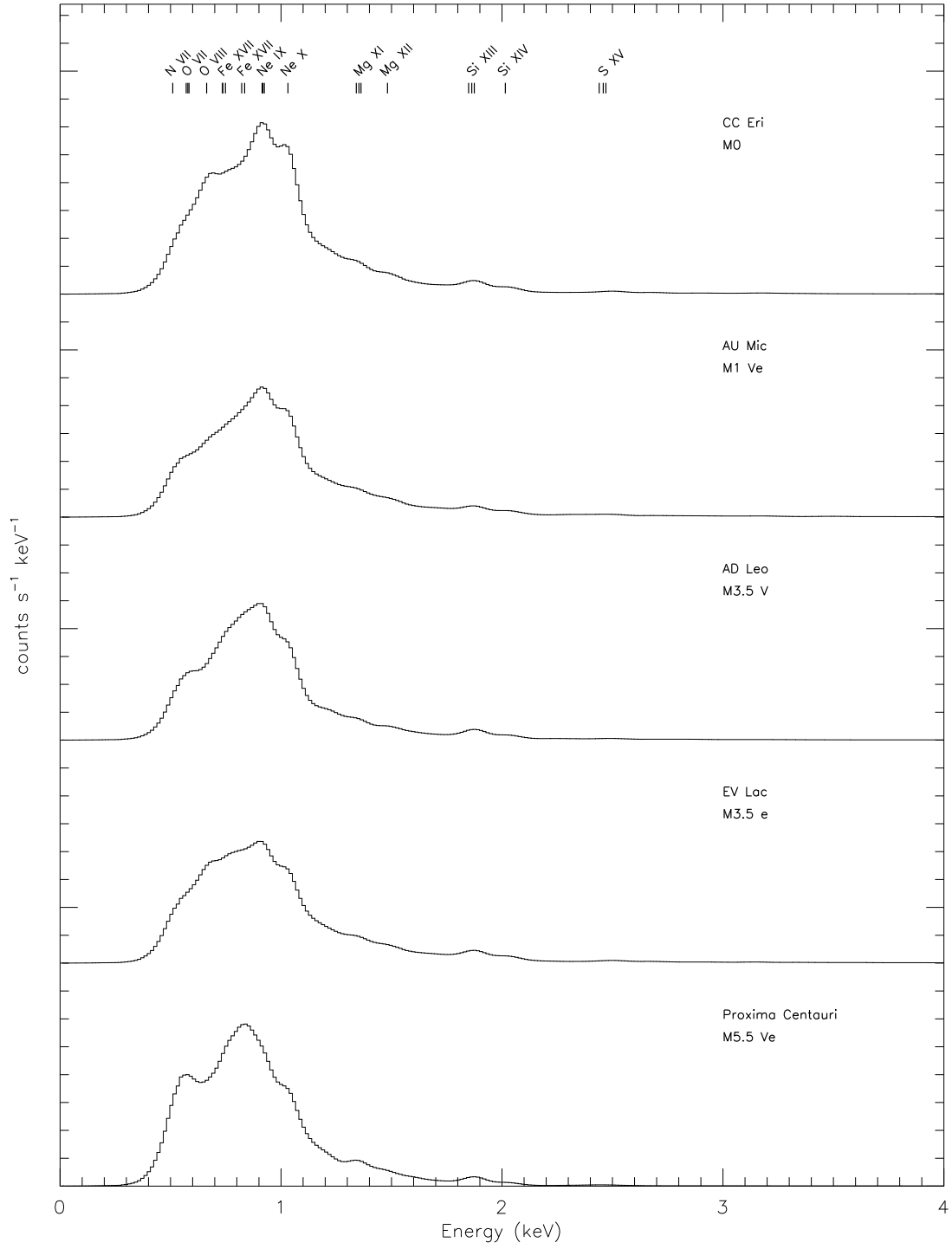


Fig. 29.— As in Figure 18, for four low-mass flare stars.

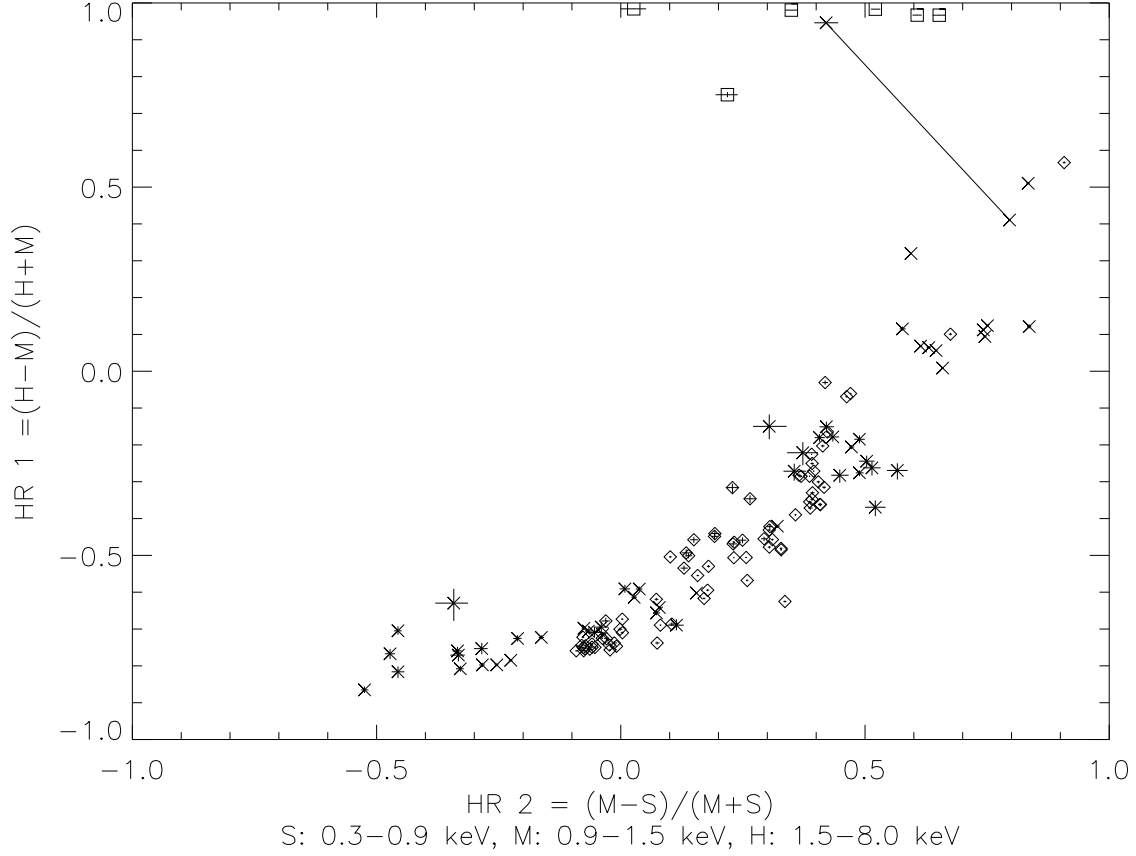


Fig. 30.— A comparison of predicted ACIS-I hardness ratios for each stellar observation in X-Atlas. $HR_1 = \frac{H-M}{H+M}$ and $HR_2 = \frac{M-S}{M+S}$ were calculated from the predicted ACIS-I aimpoint spectra (ACIS-S version, not shown here, is similar) of all stars in X-Atlas. H, M, and S are the predicted number of counts from the predicted ACIS-I spectra in the passbands designated on the plots. The softest X-ray emitters fall in the lower left, with hardness increasing towards the upper right. Errors were calculated using a Bayesian estimation technique (Park et al. 2006) and are typically smaller than the symbols. \times designates an observation of a hot star; \diamond designates a cool star; \square designates an observation of η Car. The outliers include six HETG observations of η Car and one, at approximately (0.42, 0.95), of WR 140, observed at high extinction. The lines on the plot connects that observation to another observation of WR 140 taken five months earlier at low extinction, indicating the direction of the reddening vector in the hardness ratio plot. Three observations of WR 140 made about five years later are also included, clustered around (0.75, 0.1).

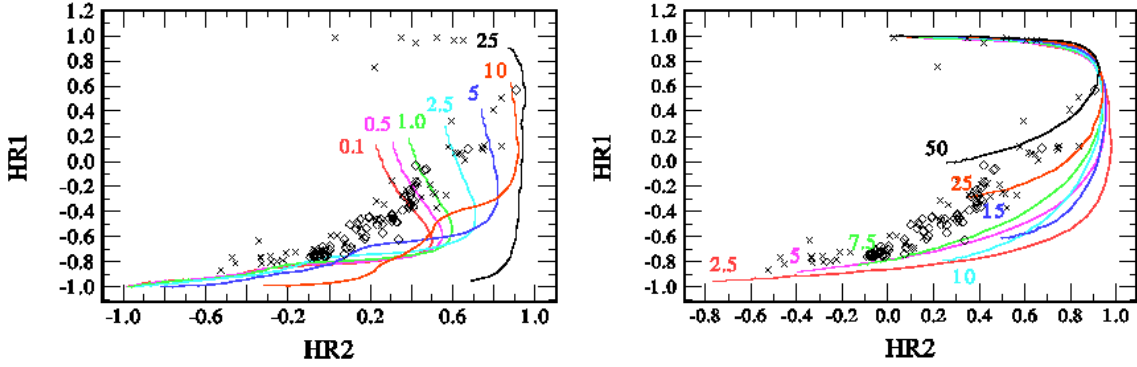


Fig. 31.— The predicted relation of HR_1 to HR_2 for ACIS-I count spectra (Cycle 06) generated with a Mekal emissivity model using solar abundances. The left plot shows lines of constant N_H in units of $10^{21}/\text{cm}^2$ for temperatures ranging from $\text{Log } T = 6$ to $\text{Log } T = 8$ starting from the bottom left along each contour. The right plot displays lines of constant T_x from 2.5 to 50 MK, with absorption increasing from 0.01 to $2.5 \times 10^{22}/\text{cm}^2$ starting from the bottom left along each contour. While this model is adequate to explain the high-mass star distribution (indicated by \times), it fails to account for the low-mass stars (indicated by \diamond).

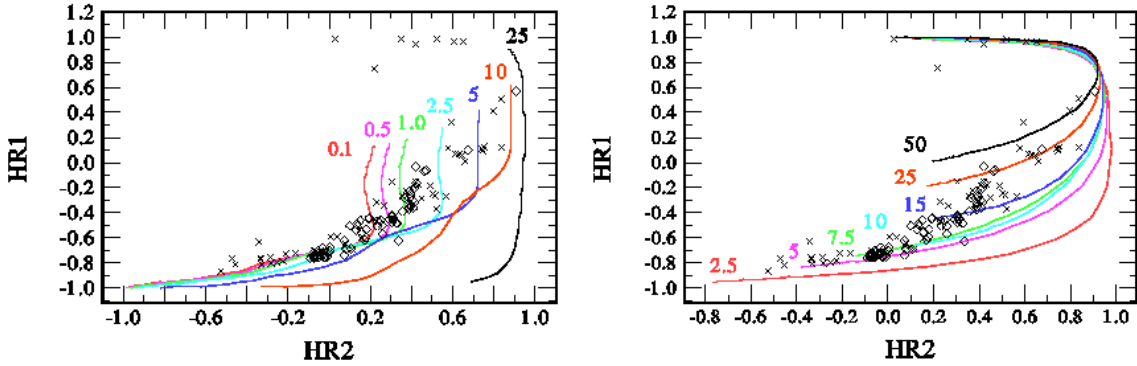


Fig. 32.— The predicted relation of HR_1 to HR_2 for ACIS-I count spectra (Cycle 06) generated with a Mekal emissivity model using an abundance of 0.1 of solar for elements except H. Contour lines are shown as in Figure 31, with lines of constant absorption in the left plot and constant temperature in the right plot. Both the high-mass and the low-mass stars fall on the model contours when the abundance is lowered to 0.1 of solar.

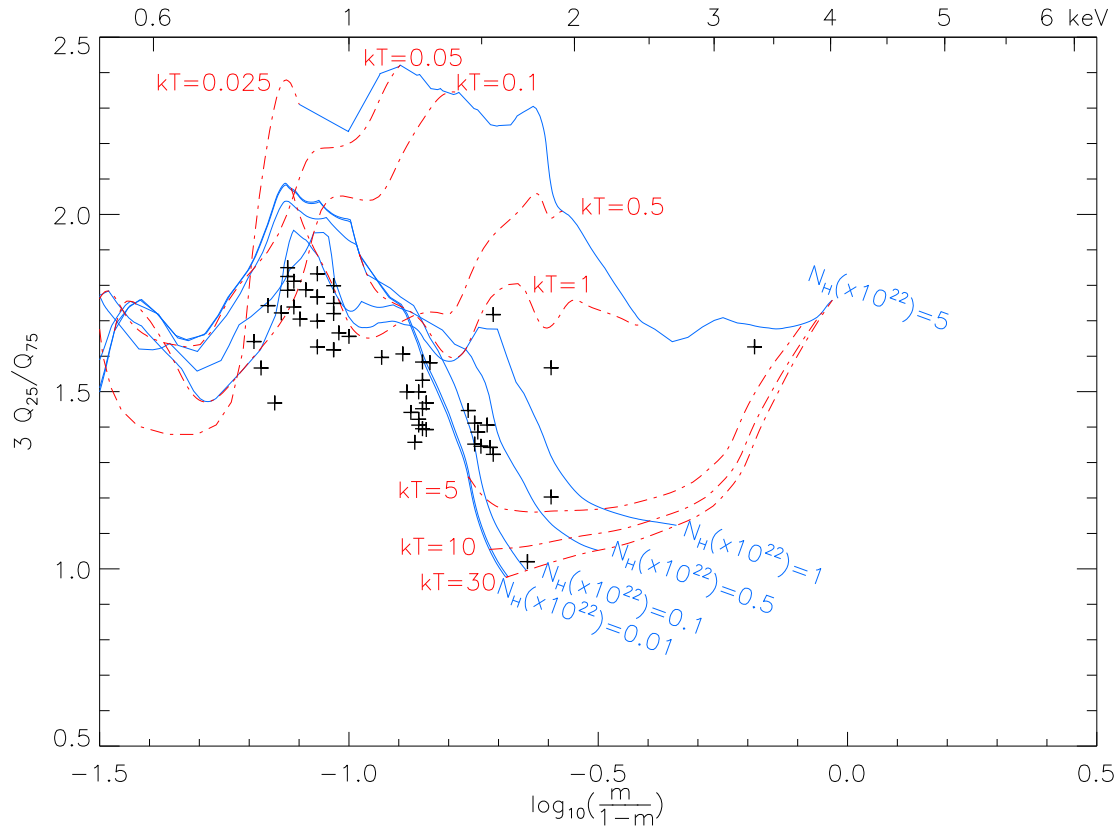


Fig. 33.— Quantile-based color-color diagram (see Hong et al. (2004)) for the predicted ACIS-I aimpoint spectra of the observations of high-mass stars in X-Atlas. The quantile grids were generated assuming solar metallicity. $m = Q_{50} = (E_{50} - E_{lo}) / (E_{hi} - E_{lo})$; $E_{lo} = 0.3$ keV; $E_{hi} = 8.0$ keV). The upper scale on the plots is the median energy in keV. The six HETG observations of the unique object η Car are not included in the plot.

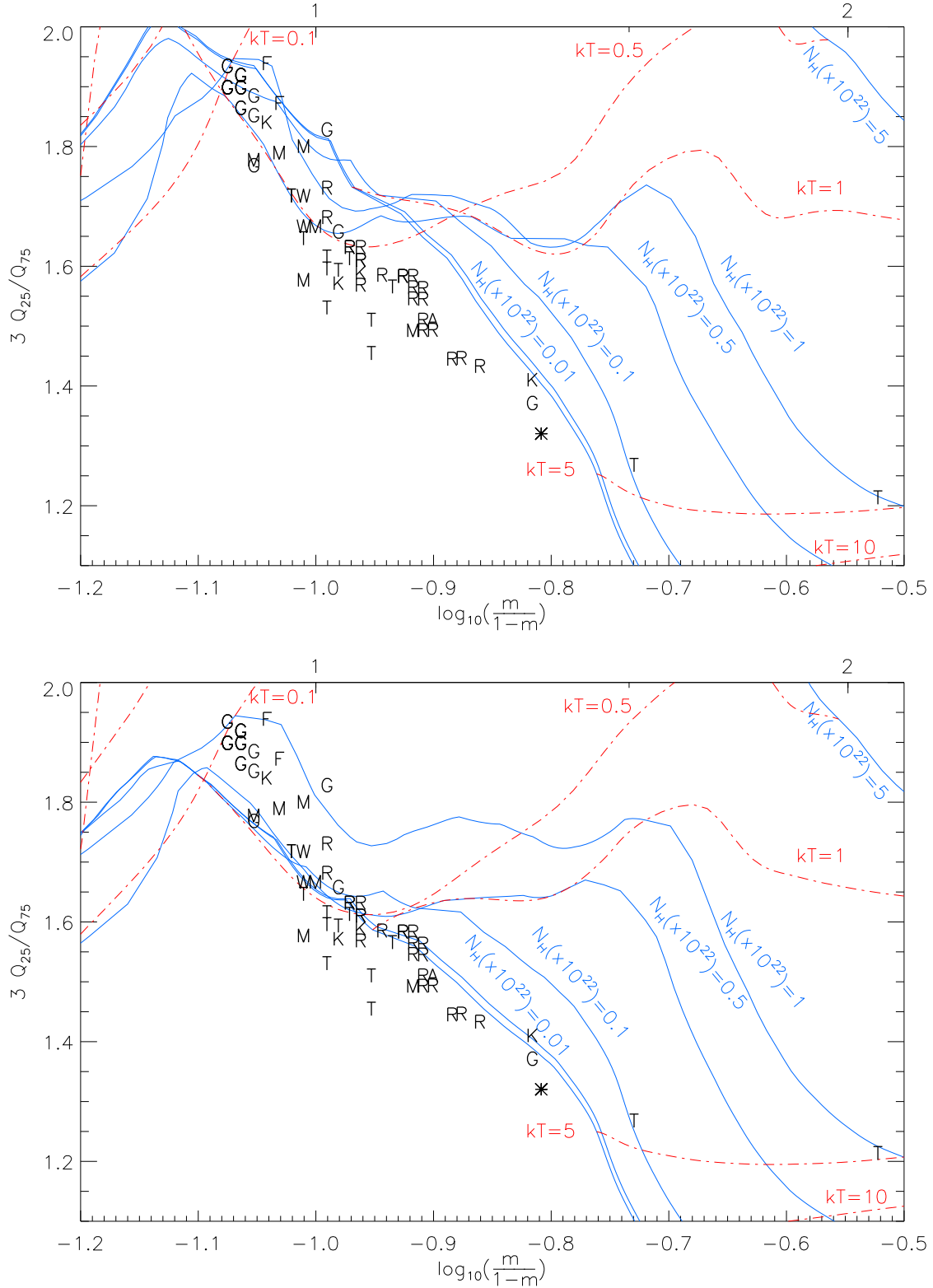
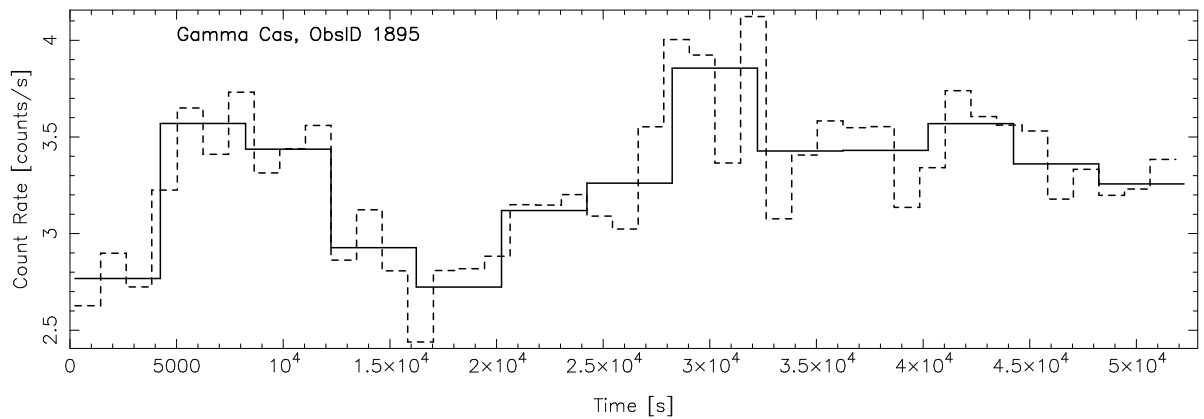
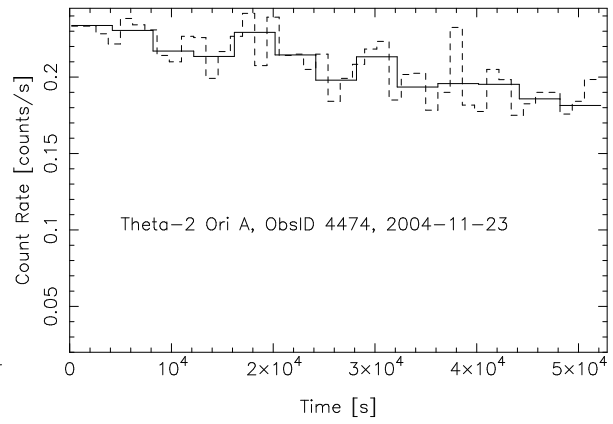
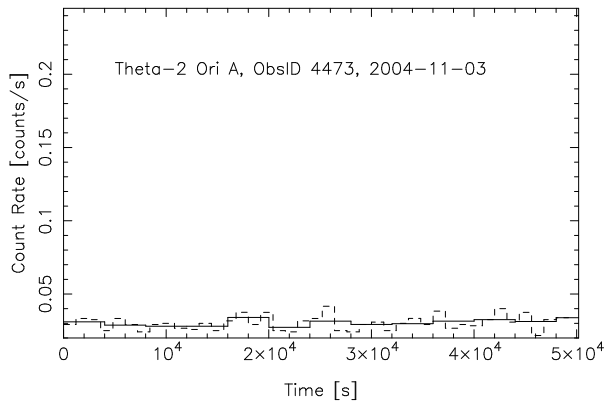
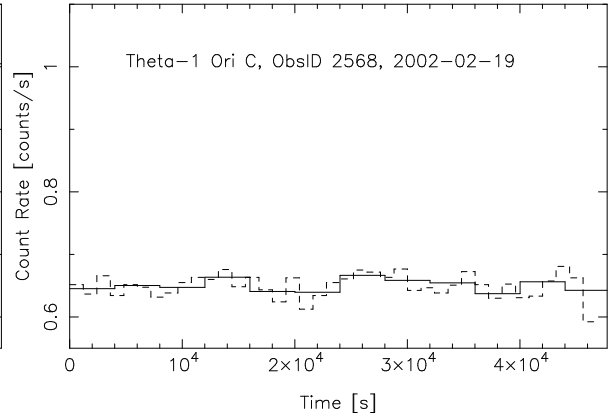
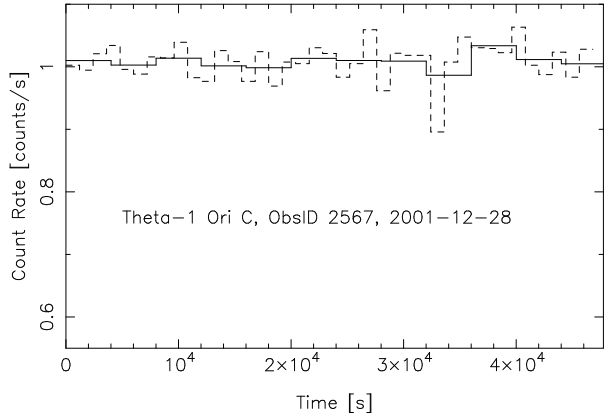
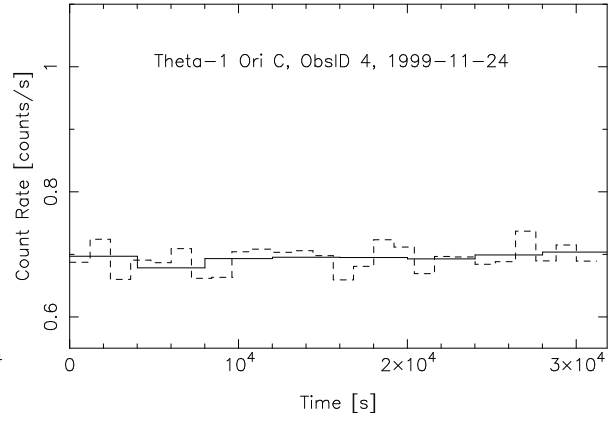
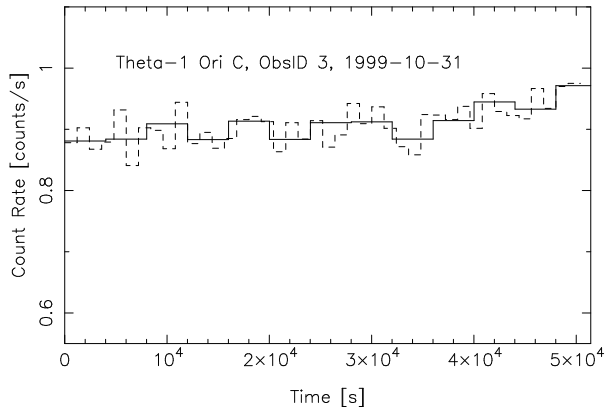


Fig. 34.— Quantile-based color-color diagrams for the predicted ACIS-I aimpoint spectra of the low-mass stars in X-Atlas. The quantile grids were calculated using metallicities of 0.3 times solar (*top*) and 0.1 times solar (*bottom*). The symbols correspond to stellar types as follows: F = normal F star; G = normal G star; K = normal K star; M = normal M star; R = RS CVn star; T = T Tauri star; W = W UMa star; A = Algol; * = FK Com. $m = Q_{50} = (E_{50} - E_{l0}) / (E_{hi} - E_{l0})$; $E_{l0} = 0.3 \text{ keV}$; $E_{hi} = 8.0 \text{ keV}$. The upper scale on the plots is the median energy in keV.



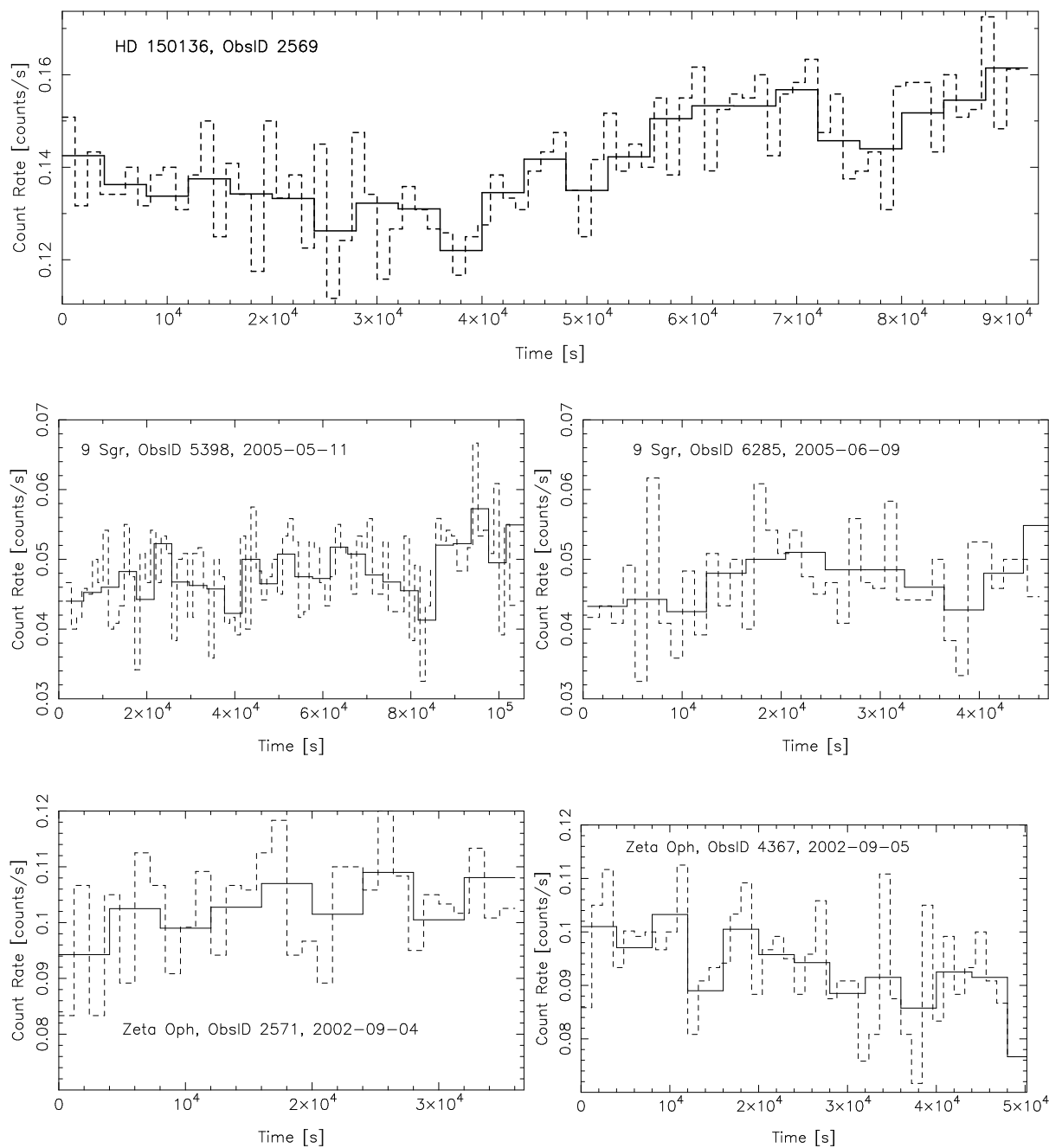
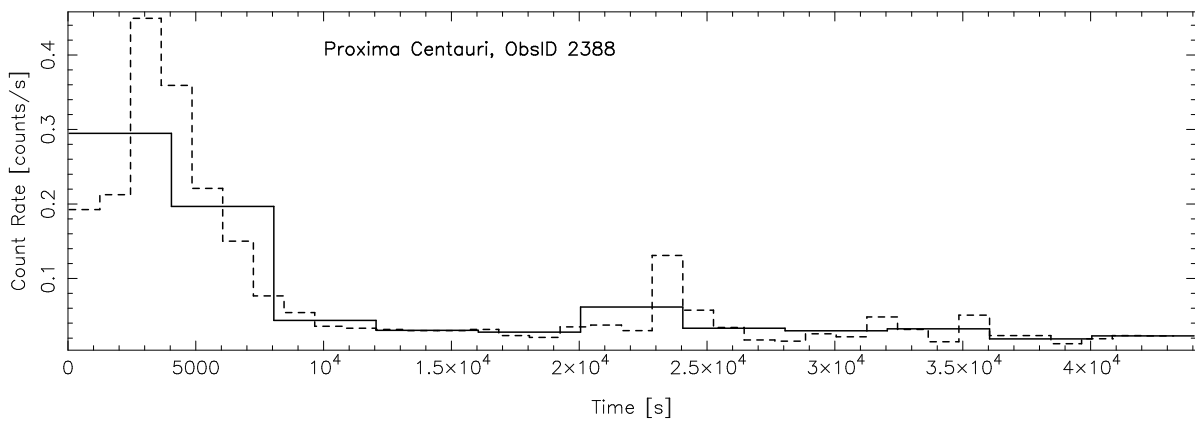
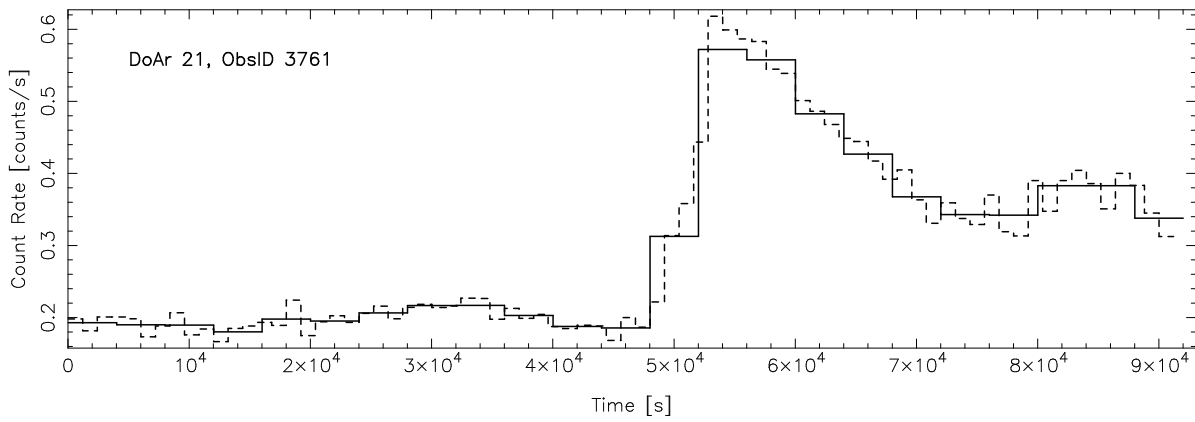
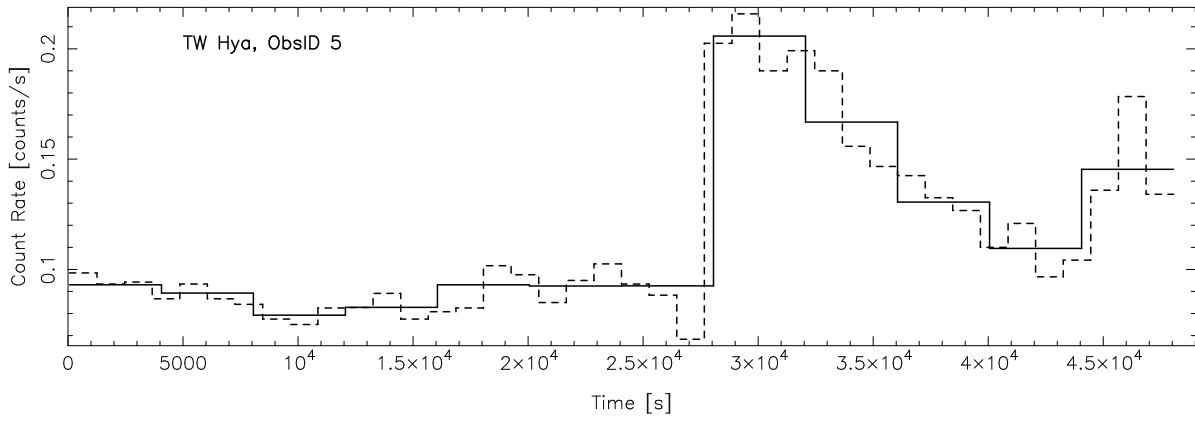
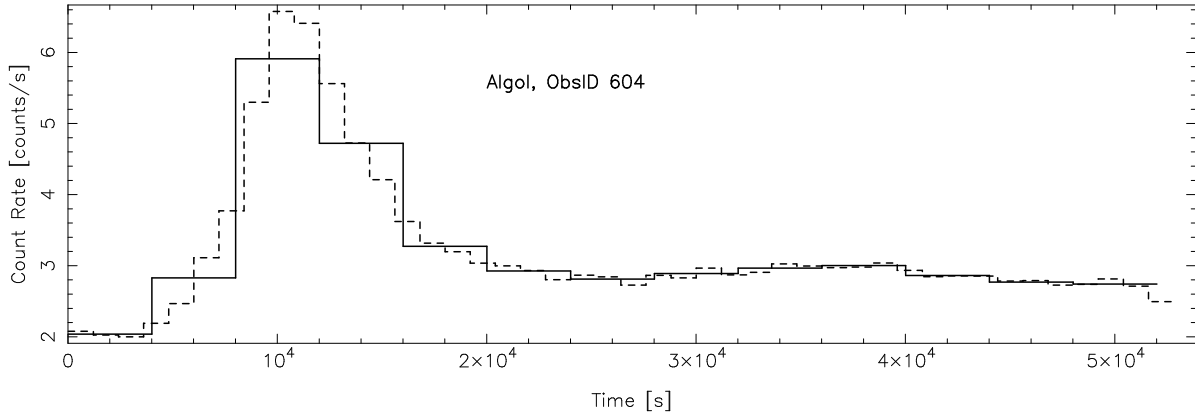


Fig. 35.— Light curves obtained from the combined dispersed counts in the HEG and MEG arms of selected HETG observations of high-mass stars. The light curves were binned at time intervals of 1200 s (*dashed line*) and 4000 s (*solid line*): Row 1-2: Four observations of θ^1 Ori C. Row 3: Two observations of θ^2 Ori A. Row 4: γ Cas. Row 5: HD 150136. Row 6: Two observations of 9 Sgr. Row 7: Two observations of ζ Oph.



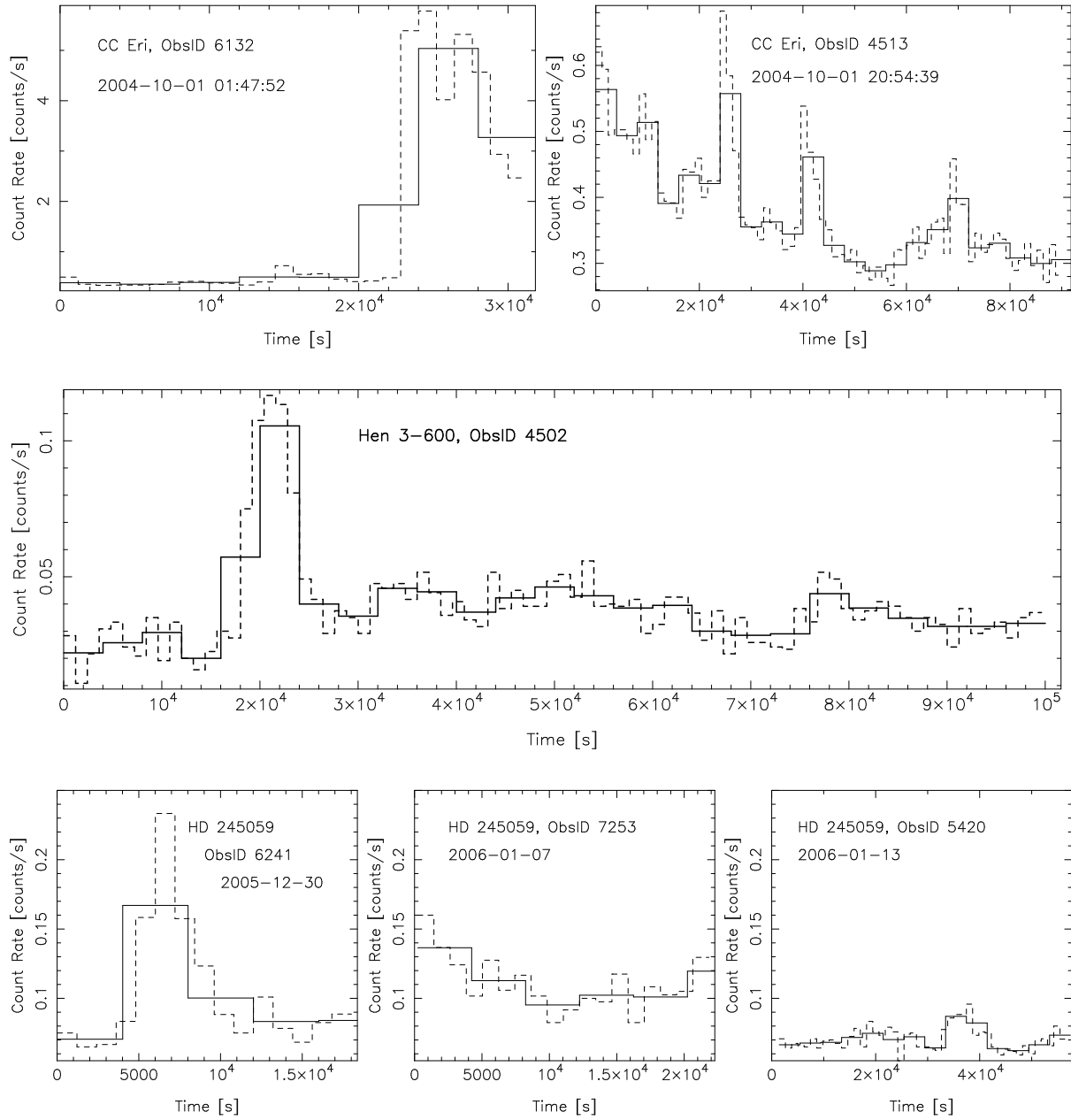


Fig. 36.— As in Figure 35, for selected low-mass stars. Row 1: Algol. Row 2: TW Hya. Row 3: DoAr 21. Row 4: Proxima Centauri. Row 5: Two observations of CC Eri. Row 6: Hen 3-600. Row 7: Three observations of HD 245059.

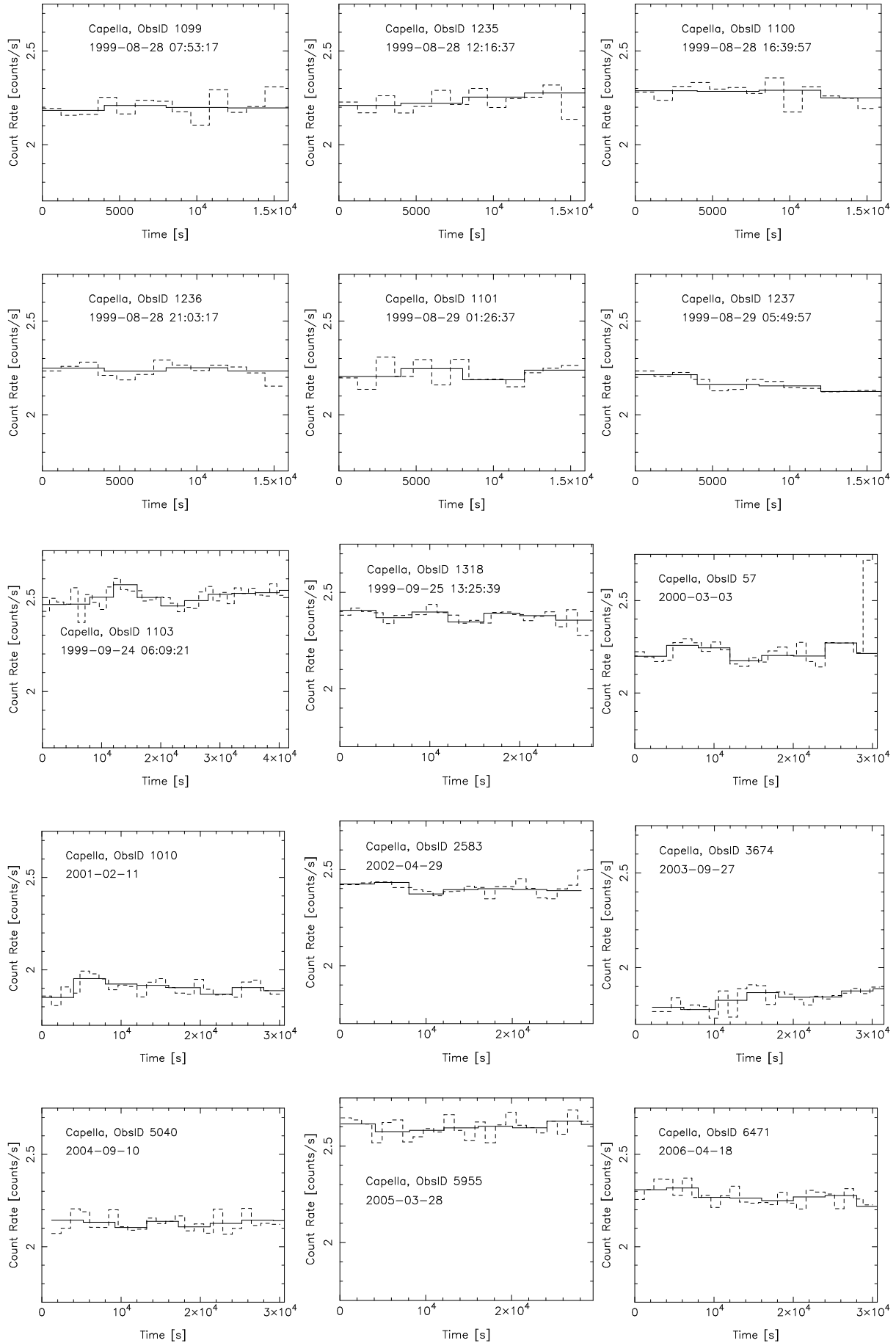


Table 1. Spectral Line Metrics

Metric	Flux ratio	Comment
NeO	Ne X λ 12.13 / O VIII λ 18.97	tracks Ne abundance
Oif	O VII(i) λ 21.8 / O VII(f) λ 22.1	O VII is density sensitive
O78	O VII(r) λ 21.6 / O VIII λ 18.97	tracks temperature
OFe	O VIII λ 18.97 / Fe XVII $\lambda\lambda$ 15.01,17.1	tracks high FIP element abundances
MgFe	Mg XII λ 8.419 / Fe XVII $\lambda\lambda$ 15.01,17.1	high-FIP elements, possibly tracks fractionation
SiFe	Si XIV λ 6.18 / Fe XVII $\lambda\lambda$ 15.01,17.1	high-FIP elements, possibly tracks fractionation
SFe	S XV λ 5.1 / Fe XVII $\lambda\lambda$ 15.01,17.1	S is a high FIP element
short line/cont	$f_{\text{line}}(\lambda < 12.13) / f_{\text{continuum}}$	sensitive to high temperatures and metallicities
long line/cont	$f_{\text{line}}(\lambda > 12.13) / f_{\text{continuum}}$	sensitive to low temperatures
line/cont	$f_{\text{line}} / f_{\text{continuum}}$	tracks metallicity
cont long/short	$f_{\text{continuum}}(13 < \lambda < 25) / f_{\text{continuum}}(3 < \lambda < 12)$	categorizes continuum shape
cont long/medium	$f_{\text{continuum}}(13 < \lambda < 25) / f_{\text{continuum}}(6 < \lambda < 12)$	categorizes continuum shape
cont medium/short	$f_{\text{continuum}}(6 < \lambda < 12) / f_{\text{continuum}}(3 < \lambda < 6)$	categorizes continuum shape

Table 2. Coadded observations in X-Atlas. ‘Num. Obs.’ indicates the number of observations that were combined. The χ^2 values listed are derived from the comparison of the observed combined 0th-order spectrum and the predicted combined 0th-order, with an extra 10% systematic error added to the observed spectrum to account for uncertainties in the effective area. ‘Num. Bins’ is the number of non-zero bins in the observed 0th-order spectrum used to calculate the *chi*² value.

Star	Num. Obs.	Observation IDs	χ^2	Num. Bins
HD 93129AB	7	5397, 7201, 7202, 7203, 7204, 7228, 7229	471.4	298
HD 93250	5	5399, 5400, 7189, 7341, 7342	865.5	630
9 Sgr	2	5398, 6285	401.8	461
15 Mon	3	5401, 6247, 6248	445.8	236

Table 3. Stars in the X-Atlas database, ordered approximately by spectral type. The 'Star' column lists the common name (if applicable) of the primary target of the observation. 'Alt. Name' gives a catalog listing for that star, usually the HD number. 'ObsID' is the *Chandra* Observation ID. 'Obs. Date' is the date the observation was made. ' t_{exp} ' is the exposure time of the observation, in ks. 'Spec. Type' is the spectral type of the star. 'B–V' is the B–V color of the star. ' d ' is the distance in parsecs from the star to Earth. 'Figure (h/l)' indicates the spectral montage figures in which the spectra from the observation can be found: the first number refers to the figure with the high-resolution MEG spectrum, and the second number refers to the figure with the projected low-resolution ACIS-S spectrum. Spectral types, B–V values, and distances were retrieved from the *SIMBAD* database, operated in Strasbourg, France, unless otherwise noted.

Star	Alt. Name	ObsID	Obs. Date	t_{exp} (ks)	Spec. Type	B–V	d (pc)	Figure (h/l)		
HD 93129 AB ^a	...	5397	2005-11-29	10.2	(2x)O2If*+O3.5V((f+)) ^e	0.206 ^e	2500 ⁿ	2/18		
		7201	2005-11-08	18.2				2/18		
		7202	2005-11-10	9.5				2/18		
		7203	2005-11-12	27.3				2/18		
		7204	2005-11-09	33.2				2/18		
		7228	2005-12-01	19.7				2/18		
HD 93250 ^b	...	5399	2005-10-22	39.7	O3.5V((f+)) ^f	0.165 ^e	2500 ⁿ	3/19		
		5400	2005-09-05	33.7				3/19		
		7189	2006-06-23	17.7				3/19		
		7341	2006-06-19	53.3				3/19		
		7342	2006-06-22	49.3				3/19		
		6285	2005-06-09	44.6				3/19		
9 Sgr	HD 164794	5398	2005-05-11	101.2	O4V((f)) ^f	0.017 ^e	1500	3/19		
ζ Pup	HD 66811	640	2000-03-28	67.6	O4I(n) ^f	-0.276	710 ^e	2/18		
HD 150136	...	2569	2002-06-27	90.3	O5III:n(f) ^e	0.161 ^e	...	2/18		
θ ¹ Ori C	HD 37022	3	1999-10-31	49.5	O5.5V ^g	0.021 ^e	...	4/20		
		4	1999-11-24	30.9				4/20		
		2567	2001-12-28	46.4				4/20		
		2568	2002-02-19	46.3				4/20		
Cyg OB2 8A	BD +40 4227	2572	2002-07-31	65.1	O6I(f)+O5.5III(f) ^h	1.09	...	5/21		
		1888	2001-02-18	34.1				O6.5V((f)) ^e	0.205 ^e	591 ^e
		1889	2001-02-09	39.5						3/19
15 Mon	HD 47839	5401	2005-11-20	54.8	O7V((f)) ^e +O9.5Vn ⁱ	-0.248	447 ^e	3/19		
		6247	2006-01-31	37.8				3/19		
		6248	2005-12-13	7.6				3/19		
ξ Per	HD 24912	4512	2004-03-22	158.8	O7.5III(n)((f)) ^f	0.014 ^e	2130 ^e	2/18		
ι Ori	HD 37043	599	2001-02-07	37.2	O9III+? ^f	-0.244 ^e	1110 ^e	3/19		
		2420	2001-02-08	12.8						
τ CMa	HD 57061	2525	2002-03-28	43.2	O9II ^e	-0.155 ^e	980.			
		2526	2002-04-24	43.9						
ζ Oph	HD 149757	2571	2002-09-04	35.4	O9.5Vnn ^e	0.019	146 ^e			
		4367	2002-09-05	48.3				3/19		
θ ² Ori A	...	4473	2004-11-03	49.1	O9.5Vpe ^e	-0.084 ^e	581.	5/21		
		4474	2004-11-23	50.6				5/21		
		3738	2003-08-12	91.0				O9.5V+B0.5V ^f	-0.240 ^e	381 ^e
δ Ori	HD 36486	639	2000-01-13	49.0	O9.5II+B0.5III ^f	-0.219 ^e	310 ^e	2/18		
ζ Ori	HD 37742J	610	2000-04-08	59.7	O9.7Ib ^f	-0.208 ^e	278 ^e	2/18		
		1524	2000-04-09	13.8						
γ Cas	HD 5394	1895	2001-08-10	51.2	B0IVpe	-0.10	188	5/21		
ε Ori	HD 37128	3753	2003-12-12	91.6	B0Ia	-0.19	412	2/18		
τ Sco	HD 149438	638	2000-09-17	59.2	B0.2V	-0.201	132	4/20		
		2305	2000-09-18	13.0				4/20		
β Cru	HD 111123	2575	2002-02-01	74.4	B0.5III ^f	-0.1520	108	3/19		
WR 140	HD 193793	2337	2000-12-29	45.5	WC7pd+O4-5 ^j	0.27 ^j	1100 ^j	6/22		
		2338	2001-05-08	24.5				6/22		

Table 3—Continued

Star	Alt. Name	ObsID	Obs. Date	t_{exp} (ks)	Spec. Type	$B-V$	d (pc)	Figure (h/l)
		5419	2006-03-31	45.1				6/22
		6286	2006-03-23	46.9				6/22
		6287	2006-04-07	49.3				6/22
γ Vel	HD 68273	629	2000-03-15	64.8	WC8+O7.5III-V ^j	-0.32 ^j	368 ^k	6/22
η Car	HD 93308	632	2000-11-19	89.5	?p	0.61	2500 ^a	7/23
		3745	2003-05-02	94.5				7/23
		3746	2003-07-20	90.3				7/23
		3747	2003-09-26	70.1				7/23
		3748	2003-06-16	97.2				7/23
		3749	2002-10-16	91.3				7/23
Algol	HD 19356	604	2000-04-01	51.7	B8V+K1IV ^l	-0.05	28.5	9/25
Canopus	HD 45348	636	2000-07-21	94.6	F0II	0.15	95.9	8/24
ν Peg	HD 220657	3731	2003-08-26	106.8	F8IV	0.61	53.1	8/24
TZ CrB	HD 146361	15	2000-06-18	83.7	G0V+G0V ^l	0.51	21.7	11/27
44 Boo	HD 133640	14	2000-04-25	59.1	G1V+G2V ^l	0.65	12.8	10/26
ER Vul	HD 200391	1887	2001-03-29	112.0	G0V+G5V ^l	0.57	49.9	11/27
ξ UMa	HD 98230J	1894	2000-12-28	70.9	G0V+G0V ^l	0.59	7.7 ^l	8/24
LS Com	HD 111812	1891	2001-03-12	130.2	G0IIIp	0.627	94.2	8/24
OU And	HD 223460	1892	2001-08-11	95.7	G1IIIe	0.79	135	8/24
AR Lac	HD 210334	6	2000-09-11	32.1	G2IV+K0IV ^l	0.72	42.0	
		7	2000-09-16	7.4				
		8	2000-09-15	7.5				
		9	2000-09-17	32.2				
		10	2000-09-20	7.2				
		11	2000-09-19	7.2				
V987 Tau	HD 283572	3756	2003-10-20	100.5	G2III	0.77	128	12/28
SU Aur	HD 282624	3755	2003-11-27	98.5	G2IIIevar	0.80	152	12/28
24 Ursae Majoris	HD 82210	2564	2002-03-26	44.4	G4III-IV	0.753	32.4	8/24
		3471	2002-03-29	44.5				
TY Pyx	HD 77137	601	2001-01-03	49.1	G5IV+G5IV	0.664	56	11/27
UX Ari	HD 21242	605	2000-01-12	48.5	G5IV	0.9	50.2	11/27
Capella	HD 34029	57	2000-03-03	28.8	G5IIIe+...	0.8	13.2	
		1010	2001-02-11	29.5				
		1099	1999-08-28	14.6				
		1100	1999-08-28	14.6				
		1101	1999-08-29	14.6				
		1103	1999-09-24	40.5				
		1199	1999-08-30	2.0				
		1235	1999-08-28	14.6				
		1236	1999-08-28	14.6				
		1237	1999-08-29	14.6				
		1318	1999-09-25	26.7				
		2583	2002-04-29	27.6				
		3674	2003-09-27	28.7				
		5040	2004-09-10	28.7				
		5955	2005-03-28	28.7				

Table 3—Continued

Star	Alt. Name	ObsID	Obs. Date	t_{exp} (ks)	Spec. Type	$B-V$	d (pc)	Figure (h/l)
μ Vel	HD 93497	6471	2006-04-18	29.6	G5IIIa	0.914	35.5	
		1890	2001-09-24	19.7				
		3403 ^c	2001-10-29	57.4				
		3410	2001-12-18	57.0				8/24
FK Com	HD 117555	614	2000-03-27	41.4	G5II	0.87	234	9/25
λ And	HD 222107	609	1999-12-17	81.9	G8III	1.08	25.8	11/27
V2246 Oph	DoAr 21	3761	2003-05-05	91.1	K0 ^m	0.33	...	12/28
II Peg	HD 224085	12 ^d	1999-10-17	0.073	K0V...	1.01	42.3	
		1451	1999-10-17	42.7				11/27
Speedy Mic	HD 197890	2536	2002-04-26	34.4	K0V	0.94	44.4	12/28
		3491	2002-04-27	34.6				
HIP 92680	HD 174429	3729	2003-06-07	73.9	K0Vp	0.77	49.7	8/24
VW Cep	HD 197433	3766	2003-08-29	116.6	K0Vvar	0.75	27.7	10/26
β Ceti	HD 4128	974	2001-06-29	86.1	K0III	1.02	29.4	8/24
λ Ori X-1	HD 245059	5420	2006-01-13	54.8	K1	0.7	...	12/28
		6241	2005-12-30	17.7				
		7253	2006-01-07	20.9				
		2538	2002-07-10	94.2				
V824 Ara	HD 155555	2538	2002-07-10	94.2	K1Vp	0.78	31.4	11/27
AB Dor	HD 36705	16	1999-10-09	52.3	K1IIIp...	0.8	14.9	8/24
YY Men	HD 32918	2557	2002-02-01	74.2	K1IIIp	1.01	292	8/24
σ Gem	HD 62044	5422	2005-05-16	62.8	K1III	1.12	37.5	11/27
		6282	2005-05-17	57.9				
IM Peg	HD 216489	2527	2002-07-01	24.6	K1.5II-IIIe	1.134	96.8	
		2528	2002-07-08	24.8				
		2529	2002-07-13	24.8				
		2530	2002-07-18	23.9				
		2531	2002-07-25	23.9				
		2532	2002-07-31	22.5				
		2533	2002-08-08	23.7				
		2534	2002-08-15	23.9				
TV Cr1	HD 98800	3728	2003-03-07	98.9	K5Ve	1.16	46.7	12/28
V4046 Sgr	HD 319139	5423	2005-08-06	97.7	K5	0.9	...	12/28
		6265	2005-08-09	45.9				
TW Hya	HIP 53911	5	2000-07-18	47.7	K8Ve	0.7	56.4	12/28
CC Eri	HD 16157	4513	2004-10-01	89.5	M0	1.36	11.5	13/29
		6132	2004-10-01	30.6				
AU Mic	HD 197481	17	2000-11-12	58.8	M1Ve	1.44	9.94	13/29
Hen 3-600	GSC 07726	4502	2004-03-16	99.4	M3	1.52	...	12/28
AD Leo	SAO 81292	2570	2002-06-01	45.2	M3.5V	1.54	4.70	
EV Lac	HIP 112460	1885	2001-09-19	100.0	M3.5e	1.36	5.05	13/29
Proxima Centauri	V645 Cen	2388	2001-09-13	42.4	M5.5Ve	1.97	1.30	13/29

^aHD 93129AB was observed with HD 93129A at the aimpoint. *Chandra* has sufficient spatial resolution to differentiate HD 93129A from HD 93129B. However, components A and B are about 3 arcsec apart along the dispersion direction, and the ACIS CCD energy resolution is not high enough to separate the events from these two sources. A third X-ray source, Trumpler 14 MJ 176, also lies in the dispersion direction ~ 5 arcsec away from HD 93129A. The extracted spectrum includes events from all three sources.

^b η Car lies directly on the spectral arm in all spectra of HD 93250. Some events from η Car may be included in the

extracted spectra, and the background counts level will be anomalously high in this region.

^cObsID 3403, a ~ 60 ks observation of HD 93497, is not included in X-Atlas. During the observation, the ACIS CCD was suffering from a problem known as threshold-plane (T-plane) lockup in chips S4 and S2, causing the science run to be stopped prematurely and replanned as ObsID 3410, which was carried out successfully.

^dObsID 12, a ~ 73 s observation of II Peg, is not included in X-Atlas. Like ObsID 3403, ObsID 12 also suffered ACIS T-plane lockup, rendering the data useless. The observation was repeated successfully as ObsID 1451.

^eMaíz-Apellániz et al. (2004)

^fWalborn (2006)

^gSchulz et al. (2006)

^hDe Becker et al. (2004)

ⁱGies et al. (1993)

^jvan der Hucht (2001)

^kMillour et al. (2007)

^lTesta et al. (2004)

^mPreibisch (1999)

ⁿEvans et al. (2003)

Table 4. χ^2 values for the comparison of the observed and predicted 0^{th} -order spectra for selected X-Atlas targets with low count rates. An extra 10% systematic error was added to the observed 0^{th} -order spectra to account for uncertainties in the effective area. The rightmost column lists the number of non-zero bins in the observed 0^{th} -order spectrum.

Target	Observation ID	Count Rate	χ^2	Num. Bins
HD 93250	7189	0.0337	174.8	257
ξ Per	4512	0.0418	381.7	340
HD 37468	3738	0.348	323.1	153
15 Mon	5401	0.0260	280.7	173
HD 206267	1888	0.0252	203.8	152

Table 5. Selected spectral fit results from the predicted ACIS-S aimpoint spectra. Fits for θ^1 Ori C, θ^2 Ori A, and γ Cas were calculated using a known, fixed N_H , while for IM Peg and Capella, N_H fit values were allowed to float. All stars were fit with a two-temperature Mewe-Kaastra-Liedahl thermal plasma model. Fits that have only one temperature listed had a flux emission ratio (FER) of 0, meaning that all of the flux was calculated to have originated from the kT_1 component of the plasma. All abundances are with respect to solar. χ^2 in the final column is reduced χ^2 .

Star	ObsID	$N_H \times 10^{22}/cm^2$	kT_1 (keV)	kT_2 (keV)	Abun.	F.E.R. (kT_2/kT_1)	χ^2
θ^1 Ori C	3	0.207	>15	1.140	0.12	0.89	1.67 ^a
	4	0.207	10.329	1.286	0.14	0.97	1.06 ^a
	2567	0.207	9.928	1.426	0.23	1.61	1.26 ^a
	2568	0.207	11.852	1.140	0.07	0.78	1.34 ^a
θ^2 Ori A	4473	0.148	0.794	0.335	0.52	1.21	1.29 ^b
	4474	0.148	3.533	1.142	0.05	0.05	1.28 ^b
γ Cas	1895	0.136	>15	...	1.25	0	1.19 ^a
Capella	57	0.014	0.602	...	0.31	0	1.80 ^b
	1010	0.057	0.568	...	0.31	0	1.71 ^b
	1099	0.022	0.568	...	0.30	0	1.08 ^b
	1100	0.034	0.561	...	0.30	0	1.14 ^b
	1101	0.01	0.597	...	0.27	0	1.75 ^b
	1103	0.031	4.098	0.561	0.32	9.79	1.42 ^b
	1235	0.047	>10	0.565	0.35	20.85	1.33 ^b
	1236	0.033	0.574	...	0.33	0	1.89 ^b
	1237	0.01	0.606	...	0.53	0	1.14 ^b
	1318	0.038	0.561	...	0.51	0	1.49 ^b
	2583	0.003	>10	0.576	0.52	5.77	0.99 ^b
	3674	0.076	0.561	...	0.51	0	1.25 ^b
	5040	0.066	0.577	...	0.44	0	1.73 ^b
	5955	0.081	0.592	...	0.40	0	1.30 ^b
	6471	0.081	0.590	...	0.31	0	1.26 ^b
IM Peg	2527	0.029	3.028	0.989	0.37	0.54	0.99 ^a
	2528	0.026	3.350	1.035	0.27	1.43	1.29 ^a
	2529	0.048	1.753	0.728	0.29	0.52	1.26 ^a
	2530	0.023	2.324	0.981	0.28	1.02	1.01 ^a
	2531	0.011	2.983	0.984	0.30	1.09	1.01 ^a
	2532	0.027	1.987	0.833	0.25	0.51	0.93 ^a
	2533	0.085	1.293	0.288	0.26	0.23	1.23 ^a
	2534	0.007	1.690	0.834	0.30	0.43	1.09 ^a

^aSpectral fits on these observations were carried out without letting all parameters float in the final fitting step.

^bSpectral fits on these observations were conducted by letting all parameters (except N_H , if known) float in the final fitting step.

Table 6. Hardness ratios and normalized quantiles for the stars in X-Atlas, derived from the predicted ACIS-I aimpoint spectra. Hardness ratios and quantiles calculated from the predicted ACIS-S aimpoint spectra are available on the X-Atlas website.

Star	ObsID	HR_1	HR_2	Q_{25}	Q_{50}	Q_{75}	$\log_{10}(\frac{m}{1-m})$	$3\frac{Q_{25}}{Q_{75}}$
HD 93129AB	5397	-0.150	0.304	0.081	0.119	0.180	-0.868	1.357
	7201	-0.369	0.521	0.085	0.114	0.159	-0.892	1.606
	7202	-0.221	0.373	0.083	0.117	0.172	-0.876	1.441
	7203	-0.282	0.448	0.085	0.121	0.171	-0.860	1.499
	7204	-0.244	0.503	0.089	0.125	0.182	-0.845	1.468
	7228	-0.269	0.566	0.091	0.127	0.172	-0.837	1.582
	7229	-0.271	0.355	0.081	0.116	0.163	-0.884	1.499
	Combined	-0.291	0.528	0.089	0.123	0.169	-0.852	1.584
HD 93250	5399	-0.178	0.434	0.087	0.121	0.184	-0.860	1.422
	5400	-0.151	0.421	0.087	0.125	0.188	-0.845	1.393
	7189	-0.262	0.514	0.089	0.123	0.174	-0.852	1.532
	7341	-0.180	0.407	0.085	0.121	0.182	-0.860	1.405
	7342	-0.185	0.489	0.089	0.123	0.191	-0.852	1.395
	Combined	-0.205	0.466	0.087	0.123	0.180	-0.852	1.452
HD 150136	2569	-0.421	0.321	0.078	0.104	0.146	-0.934	1.597
9 Sgr	5398	-0.591	0.038	0.064	0.085	0.119	-1.031	1.618
	6285	-0.591	0.008	0.064	0.085	0.119	-1.031	1.618
	Combined	-0.613	0.077	0.066	0.087	0.119	-1.020	1.666
ζ Pup	640	-0.602	0.155	0.070	0.091	0.127	-1.000	1.656
θ^1 Ori C	3	0.056	0.646	0.106	0.152	0.226	-0.748	1.411
	4	0.064	0.631	0.104	0.153	0.226	-0.742	1.386
	2567	0.009	0.659	0.104	0.148	0.216	-0.761	1.447
	2568	0.068	0.614	0.104	0.152	0.231	-0.748	1.352
	Combined	0.021	0.637	0.104	0.152	0.226	-0.750	1.411
Cyg OB2 8A	2572	0.121	0.836	0.127	0.163	0.222	-0.711	1.717
HD 206267	1888	-0.709	-0.054	0.061	0.080	0.112	-1.063	1.626
	1889	-0.695	-0.040	0.064	0.080	0.114	-1.063	1.699
15 Mon	5401	-0.767	-0.472	0.047	0.064	0.081	-1.162	1.743
	6247	-0.816	-0.456	0.044	0.062	0.083	-1.176	1.567
	6248	-0.630	-0.342	0.045	0.066	0.093	-1.149	1.468
	Combined	-0.726	-0.338	0.055	0.070	0.089	-1.123	1.850
ξ Per	4512	-0.698	-0.075	0.062	0.080	0.106	-1.063	1.767

Table 6—Continued

Star	ObsID	HR_1	HR_2	Q_{25}	Q_{50}	Q_{75}	$\log_{10}(\frac{m}{1-m})$	$3\frac{Q_{25}}{Q_{75}}$
ζ Oph	2571	-0.706	-0.067	0.062	0.080	0.102	-1.063	1.832
	4367	-0.715	-0.037	0.062	0.080	0.106	-1.063	1.767
ι Ori	599	-0.797	-0.283	0.053	0.070	0.089	-1.123	1.786
	2420	-0.759	-0.334	0.051	0.068	0.089	-1.136	1.722
τ CMa	2525	-0.753	-0.285	0.044	0.059	0.080	-1.110	1.686
	2526	-0.771	-0.333	0.040	0.055	0.077	-1.136	1.561
θ^2 Ori A	4473	-0.690	0.114	0.068	0.085	0.114	-1.031	1.799
	4474	0.115	0.577	0.108	0.155	0.241	-0.735	1.346
σ Ori	3738	-0.808	-0.329	0.053	0.070	0.087	-1.123	1.825
δ Ori	639	-0.723	-0.163	0.059	0.076	0.099	-1.086	1.787
ζ Ori	610	-0.785	-0.225	0.055	0.072	0.095	-1.110	1.739
	1524	-0.726	-0.211	0.055	0.074	0.097	-1.098	1.705
γ Cas	1895	0.320	0.594	0.123	0.186	0.362	-0.642	1.020
ϵ Ori	3753	-0.797	-0.254	0.055	0.072	0.091	-1.110	1.811
τ Sco	638	-0.642	0.079	0.066	0.085	0.116	-1.031	1.720
	2305	-0.656	0.073	0.066	0.085	0.114	-1.031	1.749
β Cru	2575	-0.865	-0.525	0.044	0.061	0.080	-1.191	1.641
γ Vel	629	0.510	0.834	0.153	0.203	0.294	-0.595	1.567
WR 140	2337	0.411	0.796	0.142	0.203	0.354	-0.595	1.203
	2338	0.946	0.420	0.281	0.394	0.518	-0.186	1.626
	5419	0.094	0.745	0.114	0.159	0.243	-0.723	1.406
	6286	0.124	0.751	0.114	0.163	0.258	-0.711	1.323
	6287	0.112	0.742	0.114	0.161	0.254	-0.717	1.343
η Car	632	0.967	0.652	0.336	0.453	0.590	-0.082	1.707
	3745	0.983	0.521	0.362	0.480	0.622	-0.035	1.747
	3746	0.751	0.218	0.193	0.368	0.557	-0.235	1.041
	3747	0.984	0.027	0.493	0.618	0.770	0.209	1.921
	3748	0.981	0.349	0.389	0.508	0.658	0.014	1.772
	3749	0.967	0.607	0.320	0.440	0.578	-0.105	1.662
Algol	604	-0.271	0.395	0.083	0.112	0.167	-0.900	1.499
Canopus	636	-0.686	0.105	0.068	0.085	0.110	-1.031	1.861

Table 6—Continued

Star	ObsID	HR_1	HR_2	Q_{25}	Q_{50}	Q_{75}	$\log_{10}(\frac{m}{1-m})$	$3\frac{Q_{25}}{Q_{75}}$
HD 220657	3731	-0.738	0.074	0.068	0.083	0.106	-1.041	1.928
TZ CrB	15	-0.506	0.232	0.074	0.093	0.133	-0.990	1.671
44 Boo	14	-0.555	0.157	0.070	0.089	0.127	-1.010	1.656
ER Vul	1887	-0.568	0.259	0.074	0.093	0.129	-0.990	1.720
XI Uma	1894	-0.673	0.003	0.064	0.081	0.110	-1.052	1.758
HD 111812	1891	-0.625	0.336	0.076	0.093	0.125	-0.990	1.817
HD 223460	1892	-0.060	0.470	0.093	0.133	0.205	-0.816	1.360
AR Lac	6	-0.481	0.328	0.076	0.099	0.140	-0.961	1.621
	7	-0.203	0.413	0.085	0.117	0.178	-0.876	1.435
	8	-0.282	0.365	0.081	0.110	0.163	-0.909	1.499
	9	-0.457	0.310	0.076	0.099	0.142	-0.961	1.599
	10	-0.455	0.293	0.076	0.097	0.140	-0.971	1.621
	11	-0.422	0.305	0.076	0.099	0.146	-0.961	1.558
V987 Tau	3756	-0.371	0.388	0.080	0.104	0.153	-0.934	1.555
SU Aur	3755	0.101	0.675	0.108	0.157	0.258	-0.729	1.257
24 Ursae Majoris	2564	-0.701	-0.002	0.066	0.081	0.108	-1.052	1.841
	3471	-0.726	-0.029	0.064	0.080	0.104	-1.063	1.854
TY Pyx	601	-0.478	0.304	0.076	0.097	0.140	-0.971	1.621
UX Ari	605	-0.390	0.358	0.080	0.102	0.152	-0.943	1.574
Capella	57	-0.749	-0.059	0.064	0.080	0.102	-1.063	1.888
	1010	-0.759	-0.076	0.064	0.078	0.100	-1.075	1.924
	1099	-0.722	-0.077	0.064	0.078	0.102	-1.075	1.888
	1100	-0.750	-0.053	0.064	0.080	0.102	-1.063	1.888
	1101	-0.741	-0.059	0.064	0.080	0.102	-1.063	1.888
	1103	-0.744	-0.080	0.064	0.078	0.102	-1.075	1.888
	1199							
	1235	-0.750	-0.077	0.064	0.078	0.102	-1.075	1.888
	1236	-0.753	-0.074	0.064	0.078	0.102	-1.075	1.888
	1237	-0.755	-0.063	0.064	0.080	0.102	-1.063	1.888
	1318	-0.759	-0.091	0.064	0.078	0.100	-1.075	1.924
	2583	-0.725	-0.038	0.064	0.080	0.104	-1.063	1.854

Table 6—Continued

Star	ObsID	HR_1	HR_2	Q_{25}	Q_{50}	Q_{75}	$\log_{10}(\frac{m}{1-m})$	$3\frac{Q_{25}}{Q_{75}}$
	3674	-0.746	-0.072	0.064	0.078	0.102	-1.075	1.888
	5040	-0.743	-0.023	0.066	0.080	0.104	-1.063	1.908
	5955	-0.757	-0.022	0.066	0.080	0.104	-1.063	1.908
	6471	-0.747	-0.009	0.066	0.080	0.104	-1.063	1.908
HD 93497	1890	-0.738	-0.013	0.066	0.080	0.104	-1.063	1.908
	3410	-0.710	0.003	0.066	0.081	0.106	-1.052	1.874
FK Com	614	-0.031	0.418	0.091	0.135	0.207	-0.808	1.320
λ And	609	-0.485	0.328	0.076	0.099	0.142	-0.961	1.599
DoAr 21	3761	0.567	0.908	0.161	0.231	0.402	-0.522	1.202
Speedy Mic	2536	-0.459	0.249	0.074	0.097	0.138	-0.971	1.602
	3491	-0.441	0.193	0.070	0.093	0.138	-0.990	1.520
HIP 92680	3729	-0.431	0.304	0.076	0.099	0.144	-0.961	1.578
VW Cep	3766	-0.595	0.178	0.070	0.089	0.123	-1.010	1.707
β Ceti	974	-0.689	0.081	0.068	0.083	0.112	-1.041	1.830
HDE 245059	5420	-0.469	0.230	0.072	0.095	0.136	-0.980	1.582
	6241	-0.316	0.229	0.074	0.100	0.153	-0.952	1.444
	7253	-0.346	0.265	0.076	0.100	0.152	-0.952	1.499
V824 Ara	2538	-0.506	0.257	0.074	0.095	0.135	-0.980	1.647
AB Dor	16	-0.464	0.232	0.072	0.095	0.138	-0.980	1.561
YY Men	2557	-0.069	0.462	0.093	0.133	0.199	-0.816	1.399
σ Gem	5422	-0.225	0.391	0.083	0.116	0.174	-0.884	1.434
	6282	-0.285	0.386	0.081	0.110	0.165	-0.909	1.482
IM Peg	2527	-0.250	0.392	0.083	0.112	0.169	-0.900	1.482
	2528	-0.355	0.387	0.081	0.106	0.155	-0.926	1.572
	2529	-0.363	0.408	0.081	0.108	0.155	-0.917	1.572
	2530	-0.361	0.408	0.081	0.106	0.155	-0.926	1.572
	2531	-0.330	0.392	0.081	0.108	0.159	-0.917	1.535
	2532	-0.300	0.405	0.083	0.110	0.163	-0.909	1.534
	2533	-0.315	0.416	0.083	0.110	0.161	-0.909	1.552
	2534	-0.348	0.392	0.081	0.108	0.157	-0.917	1.553
II Peg	1451	-0.165	0.423	0.087	0.121	0.184	-0.860	1.422

Table 6—Continued

Star	ObsID	HR_1	HR_2	Q_{25}	Q_{50}	Q_{75}	$\log_{10}(\frac{m}{1-m})$	$3\frac{Q_{25}}{Q_{75}}$
TV Crt	3728	-0.448	0.192	0.072	0.093	0.135	-0.990	1.605
V4046 Sgr	5423	-0.535	0.129	0.070	0.087	0.123	-1.020	1.707
	6265	-0.493	0.134	0.068	0.089	0.125	-1.010	1.635
TW Hya	5	-0.501	0.139	0.070	0.087	0.123	-1.020	1.707
CC Eri	4513	-0.617	0.171	0.070	0.089	0.117	-1.010	1.789
	6132	-0.285	0.369	0.081	0.108	0.165	-0.917	1.482
AU Mic	17	-0.530	0.179	0.070	0.091	0.127	-1.000	1.656
Hen 3-600	4502	-0.458	0.150	0.070	0.093	0.133	-0.990	1.585
AD Leo	2570	-0.619	0.073	0.066	0.085	0.112	-1.031	1.779
EV Lac	1885	-0.504	0.101	0.066	0.089	0.127	-1.010	1.566
Proxima Centauri	2388	-0.678	-0.031	0.062	0.081	0.106	-1.052	1.767

Table 7. Overview of the Gregory-Loredo variability analysis results. Stars were graded by their variability index. Those with indices of 7-10 have a greater than 99% probability of being variable. Those with indices of 6 were probably variable (greater than 90% probability) and those scoring below 6 (less than 90% probability) were graded not variable (Rots 2006). For stars for which multiple observations have been made, the star’s variability was judged by the observation with the highest variability index.

	Number of Stars	Variable	Probably Variable	Not Variable
High-Mass Stars	24	10	1	13
Low-Mass Stars	40	34	1	5
Total	64	44	2	18